Simulation and Measurement Techniques for Microwave Remote Sensing of Sea Ice

by

Dustin Konner Isleifson

A Thesis Submitted to the Faculty of Graduate Studies of

The University of Manitoba

in Partial Fulfillment of the Requirements of the Degree of

Doctor of Philosophy

Department of Electrical and Computer Engineering
University of Manitoba
Winnipeg, Manitoba, Canada

ABSTRACT

This dissertation presents new research into the study of simulation and measurement techniques for microwave remote sensing of sea ice. We have embarked on a major study of the microwave propagation and scattering properties of sea ice in an attempt to link the physics of the sea ice medium to experimentally obtained concomitant scatterometer measurements.

During our fieldwork, we studied the polarimetric backscattering response of sea ice, focusing on newly-formed sea ice under a large assortment of surface coverage. Polarimetric backscattering results and physical data for 40 stations during the fall freeze-up of 2003, 2006, and 2007 are presented. Analysis of the co-polarization correlation coefficient showed its sensitivity to sea ice thickness and surface coverage and resulted in a statistically significant separation of ice thickness into two regimes: ice less than 6 cm thick and ice greater than 8 cm thick. A case study quantified the backscatter of snow-infiltrated frost flowers on new sea ice, showing that the presence of the frost flowers enhanced the backscatter by more than 6 dB.

In our simulation work, an efficient method for simulating scattering from objects in multi-layered media was incorporated into a scattered-field formulation of the FVTD method. A total-field 1D-FDTD solution to the plane-wave propagation through multi-layered meda was used as a source. The method was validated for a TE-polarized incident-field through comparisons with other numerical techniques involving examples of scattering from canonically-shaped objects.

Methods for homogenization of inhomogeneous media were developed and validated using well-known dielectric mixture models. A Monte Carlo Method for simulating scattering from statistically rough surfaces was developed and was validated through favorable comparison with the SPM method for rough surface scattering.

Finally, we presented a new Monte Carlo Method for simulating sea ice remote sensing that utilized the framework of the FVTD method for scattering simulations. The modeling process was driven by actual physical measurements of sea ice, wherein dielectric and physics-based modeling techniques were employed. The method was demonstrated through a series of case studies where the scattering from newly-formed sea ice was simulated using a TE-polarized incident-field. Good agreement between experimental scatterometer measurements and simulated results was obtained for co-polarized returns, whereas cross-polarized results indicated that more depolarizing features must be taken into account.

ACKNOWLEDGMENTS

To start, I would like to thank my advisor, Dr. L. Shafai, for his continuous guidance and confidence in my research work. I would like to thank my co-advisor, Dr. D. Barber, for his guidance and for providing me with an extremely rare opportunity to conduct research in the Arctic on multiple occasions. Furthermore, I would like to acknowledge the efforts of my committee members, Dr. J. LoVetri, and Dr. T. Papakyriakou.

My research would not have been possible without major collaboration from many partners. I would like to thank my colleagues from the Centre for Earth Observation Science (CEOS) for their teamwork in conducting scientific research in such a demanding environment. I would like to thank the crew of the CCGS *Amundsen* who made our research ideas a reality.

A major thank you goes to my colleagues in the Computational Electromagnetics Group, particularly Dr. I. Jeffrey and Dr. C. Gilmore. Thanks to J. Aronsson for helping me to use the computing cluster facilities, and thanks to Dr. V. Okhmatovski for allowing me to use his computing cluster.

A special thanks goes to M. Trachtenberg, who participated in many of the same research ventures that I took part in.

I would like to acknowledge, and thank, the various funding agencies that have made my research possible. My major funding came from the National Sciences and Engineering Research Council of Canada in the form of an NSERC CGS-M scholarship and an Alexander Graham Bell CGS-D3 scholarship. Funding for my field research was provided by the Northern Scientific Training Program (NSTP), the ArcticNet program, and the Circumpolar Flaw Lead System Study (CFL), which was a major International Polar Year (IPY) project.

Finally, I would like to thank my family for their love and support throughout my PhD research.

TABLE OF CONTENTS

LIST OF TABLES

LIST OF FIGURES

LIST OF SYMBOLS AND ACRONYMS

Symbol	Definition
$\mathbf{B}$	Magnetic flux density [T]
c	Speed of light in a vacuum = 2.998×10^8 [m/s]
d	Depth [m]
d_{ice}	Ice thickness [m]
$\mathbf{D}$	Electric flux density [C/m^2]
D	Antenna aperture diameter [m]
$\mathbf{E}$	Electric field intensity [V/m]
f	Frequency [Hz]
$\mathbf{H}$	Magnetic field intensity [A/m]
j	$\sqrt{-1}$
$\mathbf{J}$	Electric current density [A/m^2]
k	Wavenumber
L_c	Correlation length for surface roughness
$\mathbf{M}$	Magnetic current density
$\mathbf{P}$	Polarization
r	Range to a given object [m]
S_i	Salinity [PSU]
S_b	Bulk salinity [PSU]
S_{si}	Salinity of the sea ice surface scraping [PSU]
T	Temperature [°C]
T_{air}	Temperature [°C]
T_{ice}	Temperature of the ice [°C]
T_{iw}	Temperature of the ice-water interface [°C]
T_{si}	Temperature of the sea ice surface [°C]
v	Velocity [m/s]
v_b	Brine volume fraction

Symbol	Definition
ϵ_0	Permittivity of free-space = 8.854×10^{-12} [F/m]
ϵ_{brine}	Dielectric constant of brine
ϵ'_{ds}	Dielectric constant of dry snow
ϵ_{eff}	Effective permittivity of a mixture
ϵ_h	Dielectric constant of a host material
ϵ_i	Dielectric constant of an inclusion
ϵ_{ice}	Dielectric constant of fresh ice
ϵ_{sw}	Dielectric constant of seawater
ϵ_{seaice}	Dielectric constant of sea ice
ϵ_{slush}	Dielectric constant of slush
λ_0	Free-space wavelength for a given frequency
μ_0	Permeability of free-space = $4\pi \times 10^{-7}$ [H/m]
ρ	Volume density of free charges [C/m ^{3}]
ρ_{ds}	Density of dry snow [kg /m^3]
ρ_{hhvv}	Copolarized correlation coefficient
σ	Conductivity [S/m]
σ_{brine}	Conductivity of brine [S/m]
σ_{ice}	Conductivity of free ice [S/m]
σ_r	Height deviation of a rough surface [m]
σ_{seaice}	Conductivity of sea ice [S/m]
ϵ_{slush}	Conductivity of slush [S/m]
σ^0_{HH}	NRCS for H-transmit, H-receive [dB m^2/m^2]
σ^0_{VV}	NRCS for V-transmit, V-receive [dB m^2/m^2]
σ^0_{VH}	NRCS for H-transmit, V-receive [dB m^2/m^2]
τ_w	Relaxation time of pure water [ns]
ω	Angular frequency [rad/s]

Acronym	Definition
1D, 2D, 3D	1, 2, or 3-Dimensional
ABC	Absorbing Boundary Condition
CAA	Canadian Arctic Archipelago
CASES	Canadian Arctic Shelf Exchange Study
CRREL	Cold Regions Research and Engineering Laboratory
CCGS	Canadian Coast Guard Ship
CFL	Circumpolar Flaw Lead (System Study)
CEOS	Centre for Earth Observation Science
dB	Decibel
EM	Electromagnetic
FDTD	Finite-Difference Time-Domain
FVTD	Finite-Volume Time-Domain
GHz	Gigahertz
HH	Synonymous with σ^0_{HH}
HPBW	Half-power beamwidth
IPY	International Polar Year
kHz	Kilohertz
MHz	Megahertz
NRCS	Normalized radar cross-section
ns	Nanoseconds
PML	Perfectly Matched Layer
ppt	Parts per thousand
PSU	Practical salinity units
PVD	Polder-Van Santen/de Loor
SPM	Small Perturbation Model
TE	Transverse Electric
TF/SF	Total-field/scattered-field
TM	Transverse Magnetic
VH	Synonymous with σ^0_{VH}
VV	Synonymous with σ^0_{VV}
WMO	World Meteorological Organization

1. INTRODUCTION

This dissertation presents new research into the study of simulation and measurement techniques for microwave remote sensing of sea ice. We have embarked on a major study of the microwave propagation and scattering properties of sea ice in an attempt to link the physics of the sea ice medium to experimentally obtained concomitant scatterometer measurements. Our primary goal was to improve upon the understanding of the physical and microwave scattering characteristics of sea ice, and to develop a new technique to model the measured radar signature of the sea ice.

1.1 Overview and Motivation

The Arctic cryosphere is a fragile environment that has received significant attention in the past decades due to the rising concern in issues of climate change. General Circulation Models used to describe our planet's climate system have indicated that the Arctic sea ice is highly sensitive to variations in the global climate change. Central to the study of the Arctic regions is sea ice type and extent, which are intimately linked to atmospheric and oceanic forcing mechanisms through the surface energy balance. Global climate change has major impacts, not only in terms of the environment, but

also on human adaptation, political attention, transportation, and natural resource use. Due to the dramatic ice depletion observed in the Arctic over the past few decades [1], improved methods to qualify and quantify sea ice remotely from space are required. Knowledge of the microwave scattering signatures of sea ice is essential for studies on the reduction of sea ice in the Arctic and the resulting changes in the climate [2]. Since increased ship activity is inevitable as more of the Arctic waters become ice-free, accurate detection and classification of sea ice types and concentration is a key issue from both a safety and economic standpoint.

Microwave remote sensing has been widely used to monitor sea ice in the Arctic for many years since it is capable of penetrating cloud, does not require solar illumination, and can observe the remote regions of the earth's surface. Space-borne radar systems have provided scientists with information on the state of Arctic sea ice since the 1970s with various active and passive sensors. These data have been used in satellite algorithms to provide information on variables such as the type and the extent of sea ice coverage.

Satellite algorithms are validated through *in situ* measurements. *In situ* scatterometer measurements, coupled with physical sampling of sea ice and surface coverage, provide a close-up look at the electrical and geophysical characteristics of sea ice. New models describing the thermodynamics and electromagnetic interactions using the data based upon field and laboratory studies have yielded an improved understanding of the ocean - sea ice - atmosphere system; however, there remain many issues that

need to be addressed.

Lingering uncertainties remain in sea ice type and concentration algorithms, which continue to be the subject of many research endeavors [3]. The level of sophistication in modeling has become quite high and validation studies are very important. Polarimetric data provides additional information for sea ice classification and is being studied to expand upon its utility. With the recent launch of RADARSAT-2, polarimetric data will be readily available and is anticipated to provide information for discriminating between ice types, and between sea ice and wind-roughened open water [4].

To date, modeling studies require improvement in understanding how the radar scattering signatures are linked to the thermodynamic and physical description of the sea ice medium. Characterization of the geophysical parameters must be improved so that the associated models have a larger range of validity and so that we can better understand the limitations of the model [5]. Furthermore, it is important to test new modeling methods and techniques, as they may give new insight for problems that have been previously attempted.

1.2 Research Rationale

This thesis involves coupling *in situ* scatterometer measurements of sea ice to modeled radar signatures via geophysical data. The goal is to develop an integrated model which will, within a reasonable level of accuracy, predict and agree with the radar signature as measured in the field. There are many reasons to develop an electromagnetic model

that connects the geophysics and scattering signatures observed in the field, some of which are:

- To provide an understanding of the governing physical mechanisms that drive the electromagnetic scattering
- To create a tool for calibrating and verifying scatterometer measurements
- To provide validation and/or calibration data for satellite remote sensing to improve upon sea ice classification algorithms
- To develop a method that can be translated to other similar situations in remote sensing
- To form a database of thermodynamic and physical states, along with their associated scattering signatures, to allow for eventual inversion of the geophysical data
- To work toward a time-series of scattering properties as a function of the sea ice physics so that we can observe the seasonal evolution of the scatterometer signatures
- To help us understand the Arctic cryosphere and the progressive effects of climate change by linking this modeling study with other aspects of the ocean - sea ice - atmosphere system

1.3 Research Goals

Early in our research we decided that it would be inappropriate to vicariously embark on a modeling study without first having a physical appreciation and understanding of the sea ice that we intended to model. Therefore, we voyaged to the Arctic on multiple occasions, and as part of many separate research endeavors, to conduct remote sensing experiments. This field work was performed in addition to studying dielectric modeling and electromagnetic simulation techniques.

To clarify our research goals, we have divided this thesis into a series of objectives with the overarching objective of developing a novel modeling technique which integrates *in situ* field data and provides a simulation tool to predict the polarimetric radar signatures of sea ice. The objectives were as follows:

1. Collect geophysical and polarimetric scatterometer data over a large variety of sea ice types and surface coverage, particularly during the fall freeze-up.

2. Study how the variations in the thermodynamic and physical state of sea ice are related to the scatterometer signatures and polarimetric parameters.

3. Develop an appropriate numerical technique or method for simulating the scattering from sea ice.

4. Develop a method of modeling the dielectrics and physical structure of the sea ice utilizing the collected field data and previous studies that will be used in the scattering model.

5. Validate, refine, and analyze the developed electromagnetic model using actual *in situ* geophysical data and measured polarimetric radar signatures.

Fig. 1.1 presents a diagrammatic overview of this PhD thesis work. During the fieldwork portion of this thesis, measurements of the radar signatures of various forms of sea ice were obtained using a C-band polarimetric scatterometer system. Detailed physical measurements were conducted in conjunction with each scatterometer measurement. The dataset includes measurements of sea ice from open water and early formation during the fall freeze-up until the depth of winter. In addition, the dataset was supplemented by measurements of multiyear sea ice just before the fall freeze-up and during the freeze-up. The field data has provided data and validation for the modeling process. More specifically, the geophysical parameters measured were used to make decisions in the dielectric and scattering modeling methodologies. The EM modeling was an iterative process. Once the general model was completed, a large series of simulations took place using the developed model and specific test cases that were associated with high quality *in situ* measurements. The model was refined during this process, until a satisfactory comparison with the actual measured radar signatures was obtained.

1.4 Research Facilities

The direction of our research work was certainly influenced by the facilities that were made available to us. The Centre for Earth Observation Science (CEOS)

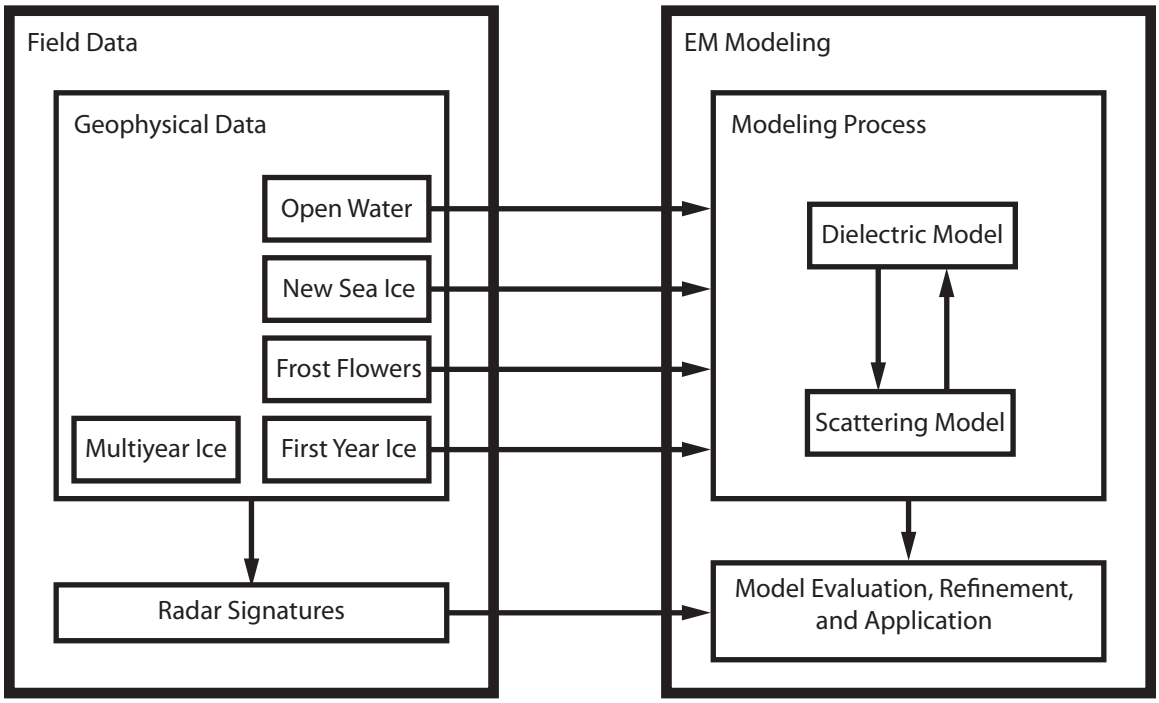

Fig. 1.1: Thesis research block diagram.

owns specialized equipment for conducting physical sampling of snow and sea ice variables. The radar system that we used for our research was a C-band polarimetric scatterometer, which was also owned by CEOS. Perhaps the most important component of our field-based research program was the CCGS *Amundsen* (shown in Fig. 1.2) and her crew. Without the ship to act as a platform for conducting our research, we would have been extremely limited in the diversity of sea ice types and locations that we were able to visit.

In terms of engineering facilities, we have had a suite of electromagnetic laboratories and software packages available from the Department of Electrical and Computer Engineering. For example, we made extensive use of the program MATLAB © [6].

Fig. 1.2: The CCGS *Amundsen*: our research base during the ArcticNet and CFL projects.

While we have performed tests using the standard commercial EM simulation software packages, we were fortunate to have the Computational Electromagnetics (CEM) group to help us in our research. A parallelized FVTD computational engine was being developed within the laboratory, and so, it was convenient to work with the CEM group to incorporate some of the specific code that was required for remote sensing simulations. Finally, we were given the privilege to use a computing cluster, which significantly sped up our code development. This computing cluster also provided us with the ability to perform Monte Carlo simulations, which were the backbone of our simulation methods.

1.5 Outline of the Thesis

This dissertation presents work and material from a variety of research areas and topics, each of which are scientific or engineering disciplines on their own, and which are united in the remote sensing problem.

In Chapter 2 we present relevant information on each of these major topics: 1) Geophysics of Snow-Covered Sea Ice, 2) Microwave Remote Sensing of Sea Ice, and 3) Modeling Aspects for Sea Ice Remote Sensing.

Chapter 3 presents results and analysis of the geophysical variables and sea ice remote sensing. We analyze the radar data and make some inferences based upon our measurements and observations. Polarimetric backscattering results and physical data for 40 stations during the fall freeze-up of 2003, 2006, and 2007 are presented.

Chapter 4 and Chapter 5 provide detailed information on the simulation and modeling techniques that we have investigated towards our goal of developing an appropriate technique for sea ice remote sensing. Chapter 4 focuses on the validation of a technique for simulating multi-layered media that we incorporated in the FVTD engine. We validate the technique for scattering from discrete objects in the multi-layered media. Chapter 5 focuses on rough surface scattering techniques and propagation properties of inhomogeneous media using the FVTD method.

Finally, in Chapter 6, we present a new Monte Carlo method for simulating sea ice remote sensing. The modeling process is driven by actual physical measurements of sea ice, wherein dielectric and physics-based modeling techniques are employed. This

Monte Carlo method is validated through a series of case studies, where we show that we can match experimentally measured scatterometer measurements by appropriately describing the physics of the sea ice medium.

We finish the document with a conclusion and an outline of the future work which we think should be considered.

2. BACKGROUND

In this chapter, we present relevant information on three major topics: 1) Geophysics of Snow-Covered Sea Ice, 2) Microwave Remote Sensing of Sea Ice, and 3) Modeling Aspects for Sea Ice Remote Sensing. We begin by presenting important aspects of snow-covered sea ice, particularly with respect to the formation, structure, and variations present in naturally forming sea ice. Next, we present fundamental topics in polarimetric remote sensing of geophysical media. We discuss the underlying mathematical equations governing wave propagation in multi-layered media, present the dielectric properties of snow and sea ice, and explain how the properties manifest themselves in polarimetric radar measurements. Finally, we discuss some of the available techniques and methods that have been used for modeling microwave scattering from a geophysical medium, including scattering and dielectric models. We present the finite-volume time-domain (FVTD) and finite-difference time-domain (FDTD) methods in the context of their use as a modeling tool for microwave remote sensing.

2.1 Geophysics of Snow-Covered Sea Ice

The geophysical and thermodynamic state of sea ice effectively determines the propagation behavior of any electromagnetic wave that is used to interrogate the sea ice medium in a remote sensing experiment. Since sea ice is a thermodynamically and dynamically active medium, the thermodynamic state must be defined at a single point in time and space through measurement and description of the temperature, salinity, and structure of the sea ice. Whereas fresh water ice is a relatively homogeneous substance, sea ice is a heterogeneous mixture of ice, air bubbles, brine, and solid salts. Physical properties are highly variable across various sea ice samples; however, systematic relationships exist in the growth cycle, such that meaningful relationships can be determined.

In this section we will present the geophysics of sea ice as they pertain to the remote sensing problem. We begin by describing the formation and basic structure of sea ice. Next, we discuss the salinity structure of sea ice through a description of the dynamic inclusions within the ice crystal matrix. Following this, we present some physical details on some important surface features that may be present on sea ice.

2.1.1 The Formation of Sea Ice

Sea ice begins to form when the surface temperature of the ocean reaches the freezing temperature of seawater (-1.86°C at 34 PSU). The cooling of the surface produces instability in the density structure of the upper ocean layer since seawater has a

freezing temperature that is higher than the temperature of its maximum density. This results in convective mixing, causing heat to be transferred from the lower layers of the water to the ocean surface. In this super-cooled upper ocean layer, tiny disks of ice begin to form, floating towards the surface, as the density of the ice is less than that of the seawater. Through motion and further freezing, a layer of randomly oriented needles and platelets known as frazil ice begins to accumulate. As more ice forms, it gathers at the surface as grease ice, which bears a resemblance to grease floating on water. If there is no wind action, the grease ice begins to consolidate and solidify into a thin elastic crust known as nilas. If there is wind action, then the frazil collects into rounded pans and forms pancake ice. The pancakes collide and have elevated ridges due to the collisions. Eventually this ice form consolidates as well. Once the ice has consolidated, congelation growth occurs from the freezing of seawater to the bottom of the ice at the ice-ocean interface due to the upward conduction of heat [7].

2.1.2 Sea Ice Structure

The structure of first year sea ice formed under quiescent conditions can be stratified into three distinct layers: frazil, transition, and columnar. Each of these layers exhibits significantly different physical characteristics since the formation and growth mechanisms are quite different. One key aspect throughout the growth cycle is the rejection of brine from the ice crystal structure (discussed in more detail later in this

section). Sea ice is a polycrystalline substance, wherein the individual ice crystals may have different orientations.

The uppermost layer of the sea ice is called the frazil layer, which is a highly granular form due to the turbulent mixing that occurs during its formation. The frazil layer is fine grained in structure with random orientations of the ice crystals and random locations of brine inclusions due to its formation mechanisms [8]. Typically the frazil layer makes up about 5% of the ice cover and is usually 1-10 cm thick [7]. During its formation, frazil ice has fluid-like properties and transitions to solid-like characteristics once the volume fraction of ice is near 40% [7]. In terms of physical strength, fine grain frazil is stronger than coarse grain frazil, and the strength of frazil decreases as the volume of brine inclusions increases. The sizes of frazil ice crystals measured recently in forming grease ice were found to be on the order of 3-4 mm, with a random orientation [9].

The transition layer lies below the frazil layer in congelation sea ice. Once the frazil layer has solidified into nilas, there is one less degree of freedom for the ice growth to occur – a process known as geometric selection. Growth with the principle crystallographic c-axis [1] of the ice perpendicular to the temperature gradient is thermodynamically favorable due to the lower energy requirements [7]. If the grain boundaries of the conglomeration of frazil ice crystals are not perpendicular to the

[1] The c-axis in the naturally occurring ice polymorph Ih is perpendicular to the hexagonal structure of the ice crystal lattice. This open crystal structure is the reason that ice is less dense than liquid water.

freezing interface, the growth will cause interference between crystals, and crystals not growing in the preferred direction are gradually cut off.

The columnar layer is below the transition layer and it consists of pure ice plates that are separated by parallel layers of brine [8]. It is characterized by a strong crystal elongation parallel to the direction of heat flow, pronounced crystal orientation, and an increase in crystal size when moving away from the cold source. This is similar in effect to the growth of metal ingots in metallurgy [7]. In terms of horizontal orientation, the crystals are generally isotropically positioned. The substructure of the columnar layer has a cellular characteristic, with ice platelets evenly spaced and separated by grain boundaries as depicted in Fig. 2.1. It is between these grain boundaries that the salt, in the form of solid or liquid, is held. The most important parameter of substructure is arguably the brine layer spacing - this is the distance between brine pockets, measured parallel to the c-axis. There is a general increase of brine layer spacing with an increase of depth and with growing conditions under constant temperature. Slower growth results in a larger brine layer spacing as there is more time to reject brine and salt, whereas faster growth results more brine entrapment in brine pockets.

The size of the grains in columnar ice increases with depth. At the top of the layer the horizontal diameter may be several tenths of centimeters, increasing to a diameter of several centimeters near the bottom of the ice. The vertical length of grains may be millimeters [10]. At the bottom of the sea ice, at the seawater interface, a non-planar, dendritic interface called the skeletal layer forms due to the thermodynamic processes.

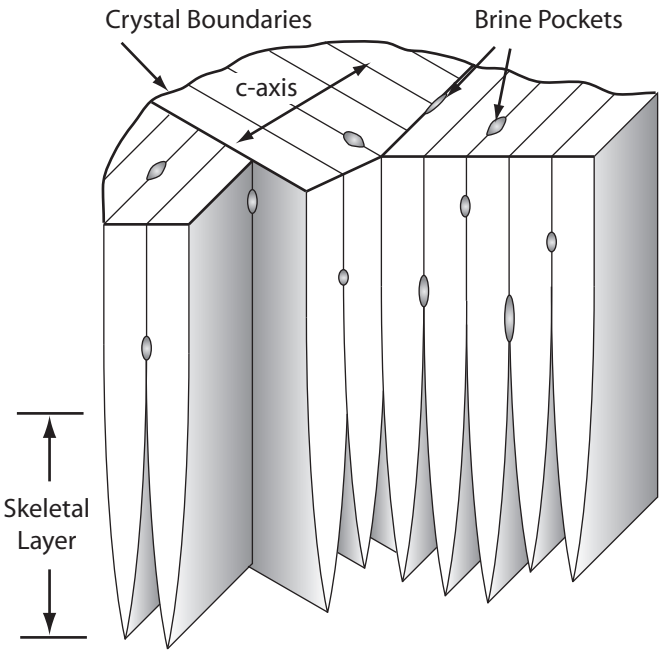

Fig. 2.1: Illustration of the skeletal layer at the bottom of the sea ice. *c*-axis orientation of the individual ice platelets are shown within the crystal boundaries. Brine pockets lie in the interstices between the ice platelets.

This layer is typically on the order of 1-3 cm in thickness and is depicted in Fig. 2.1.

Brine drainage tubes are a complex capillary system of interconnected brine pockets that develop as the sea ice forms. These brine drainage channels collect into larger tubes and eventually exit at the bottom of the sea ice. As an example, brine drainage tubes at the bottom of a 1.55 m thick ice sheet were measured at 0.4 cm diameter on average, with one large channel for every 180 cm^2, whereas other studies have measured the tube diameter as 0.1-1.0 cm on average [7]. The number of brine channels is related to the growth rate of the sea ice. Ice stalactites can form from the cold "brine streamers" that are expelled from the channels.

2.1.3 Salinity Profile

The salinity of sea ice makes it very different thermodynamically, mechanically, and electrically from fresh ice. The salinity profile of first year sea ice typically has a C-shape characteristic due to the formation mechanisms and brine dynamics. Liquid inclusions of brine are entrapped in the sea ice, determined initially by the rate at which the sea ice grows. As the ice increases in thickness, the bulk salinity decreases. Differences in temperature during the formation and thermodynamic evolution of sea ice therefore have an effect on the salinity and consequently on the electrical properties through the dielectrics (discussed in Section 2.2). Changes in the dielectrics are evident in the radar signatures, and so, the thermodynamics have a direct impact on the backscattering measurements.

Brine Volume Fraction

The brine volume fraction represents the amount of brine present in a given sea ice sample as a percentage of the total volume of the sea ice sample. Since the sea ice crystal matrix rejects the brine as it forms pure ice crystals, the brine forms pockets within the interstices of the ice crystals. The salinity and temperature of the brine pockets are dependent upon the temperature as the sea ice attempts to achieve thermal equilibrium, and therefore the brine volume can be calculated using the temperature and salinity of a sea ice sample. Frankenstein and Garner [11] derived a series of empirically based equations following the phase diagram of Assur [12] to calculate the

brine volume for the temperature range between -0.5 and -22.9°C:

$$v_b = 10^{-3}\, S_i\, (-52.56/T - 2.28),\ -0.5°C \geq T \geq -2.06°C, \tag{2.1}$$

$$v_b = 10^{-3}\, S_i\, (-45.917/T + 0.930),\ -2.06°C \geq T \geq -8.2°C, \tag{2.2}$$

$$v_b = 10^{-3}\, S_i\, (-43.795/T + 1.189),\ -8.2°C \geq T \geq -22.9°C, \tag{2.3}$$

where v_b is the brine volume fraction, S_i is the salinity, and T is the temperature in °C. Later, Cox and Weeks [13] revisited the problem and accounted for solid salts, developing a series of equations that determine the relative brine volume between -2 and -30°C. They also include a calculation for the air volume fraction, which accounts for the air voids that may be present in the sea ice.

Brine Dynamics

The salinity of sea ice is controlled by the entrapment of salt in brine pockets [8]. There are several major brine dynamic processes: brine expulsion, pocket migration, gravity drainage, and flushing [7]. As the sea ice grows, the volume of the ice increases and microscopic cracks can appear. Brine expulsion occurs since as the ice cools, the brine pockets shrink, become pressurized, and consequently the liquid can be forced upwards or downwards. Pocket migration arises due to the temperature gradient within the ice and within the brine pockets themselves - freezing occurs on the colder side and melting occurs on the warmer side. Gravity drainage occurs since the ice

begins to float and rise out of the seawater, while the brine seeks to remain at sea level. The microscopic cracks in the ice and brine drainage channels can facilitate the drainage, and this factor is amplified by the increased density towards the relatively cold sea ice surface. Golden found that at temperatures above -5°C and a salinity of 5 parts per thousand (ppt) the sea ice becomes effectively permeable to fluid flow [14]. Finally, melt water flushing happens during the melt and summer seasons where fresh water from rain or snow melt flows into the ice and the denser brine is ejected out from the bottom.

Sea Ice Inclusions

Detailed information on the sea ice inclusions and sea ice microstructure is important when analyzing microwave scattering. Size, shape, orientation, and content of the inclusions are each significant since they play a role in the overall physical characteristics of the sea ice as well as governing the microwave interactions with the sea ice. In sea ice, the inclusions include brine pockets and tubes, air pockets, and in some cases, precipitated salts. In first year ice, the brine volume fraction is typically much higher than the gas volume fraction.

Many statistical studies have been conducted on the details of the microstructure of sea ice, for example [15], and [16]. There have been numerous studies conducted on the statistics of the inclusions, ranging from the more traditional "thin sections," where sections of the ice are mounted on glass plates, shaved down to millimeter

thicknesses and observed under microscope, to more sophisticated techniques such as magnetic resonance imaging (MRI). The size and shape of the brine pockets are highly temperature dependent, with warmer ice tending to have larger brine inclusions [15]. Additionally, the brine pockets appear to have a characteristic horizontal spacing [16].

In terms of shape, the brine pockets can range from spherical to spheroidal, with an elongation in the vertical direction [16], [17]. In a study of the microstructure of multiple sea ice types, Perovich and Gow found that there is an axial ratio in the horizontal plane of 4:1, implying that the shape of the inclusions is ellipsoidal [18]. As another example, ([19], Table 2) reports that in their MRI study they found that sea ice at a 5 cm depth had inclusions with an ellipsoidal shape in the horizontal plane, with a major axis of 1.19±1.44 mm and a minor axis with 0.58±0.56 mm. In contrast, [17] has reported that the average size of inclusions is 0.27 mm in the horizontal plane and 2.4 mm in the vertical plane, but their ice samples are from 0.8 m in depth and therefore are representative of columnar sea ice.

2.1.4 Multiyear Sea Ice

Multiyear sea ice (MYI) is defined as sea ice which has survived at least one summer melt period. It is physically quite different from first year sea ice, having a weathered characteristic appearance with surface features that include rolling hummocky hills and meltponds [10]. Its thickness is typically around 2.5-5 m, but it can reach up to 12 m thick if the conditions are right for growth [7]. Fig. 2.2 shows a MYI floe

Fig. 2.2: A multiyear sea ice floe as seen from the CCGS *Amundsen* during our ArcticNet 2006 research cruise through the Canadian Arctic Archipelago.

during September and before the fall freeze-up has occurred. The large hummocks are several meters thick, while the smooth flat areas are only several tens of centimeters in thickness. Open water can be seen in the distant background.

During its lifecycle, the bulk salinity of sea ice decreases as it thickens and ages, and so, multiyear sea ice has a much lower salinity than first year sea ice. Air bubbles within the sea ice fabric are evident in the low density hummocks due to desalination mechanisms. Annual layering gives the ability to potentially establish sea ice age. Simple layering mechanisms include snowfall layers on top of the ice, whereas underneath the ice, frazil freely suspended beneath the ice may accumulate

and freeze to the bottom of the ice layer. Fresh ice can lie between the dense seawater and the bottom of the ice, caused by melting, runoff, and enhanced by thaw holes in the ice. Melt-water ponds, with or without snowfall, may exist on the surface of the multiyear floes. The crystals within the ice structure re-texturize during the summer melt, resulting in sharp crystal edges becoming rounded. While still columnar, the structure of the ice becomes brine-poor and glacial-like. The most pronounced effects are in the top layers of the ice which become more porous and less dense. As the ice desalinates and the crystal structure slowly changes, the ice becomes brittle and eventually begins to break down and decay.

2.1.5 Surface Features

Surface features on sea ice represent an important component of the ocean-sea ice-atmosphere system. The thermodynamic evolution and geophysical state of the sea ice can be completely different for sea ice under different surface coverage. Radar measurements at microwave frequencies are very sensitive to surface features, not only due to the addition of a new scattering layer, but also due to the thermodynamic changes that occur with the presence of a particular surface coverage.

Saline Surface Layer

A thin brine skim has often been observed on newly forming sea ice. This thin layer can freeze and form a very high salinity skim on the sea ice surface [20]. It can

additionally act as a source of brine for frost flowers (discussed later in this section). The brine within the sea ice is transported towards the surface, but the exact nature of the transport has not yet been fully verified. One suggestion is that the saline layer is formed by brine expulsion, which is important with the initial formation, but decreases in importance as the sea ice thickens [21]. It would be enhanced since in the upper layer of the ice the porosity is higher than the underlying ice, providing favorable conditions for the upward transport of brine [21]. Another suggestion is that brine may be transported within the ice grain boundaries towards the sea ice surface, as determined by a thermo-molecular pressure gradient [22], and attributed to the temperature difference between the warmer underlying seawater and the colder atmosphere.

Snow

Snow cover on sea ice has important ramifications in terms of the thermodynamics, dielectrics, and scattering signatures of the sea ice. Snow on sea ice can be described as a mixture of ice, air, and potentially liquid water and/or brine. In characterizing snow cover the parameters of interest include the thickness, density, temperature, salinity, liquid content, grain size, and grain structure. These parameters change based on the formation of the initial snow and the thermodynamic evolution of the snowpack. Snow on sea ice can be divided into layers based upon the physical parameters. Statistics on the grain size, density, and salinity have been measured, for example, in [23].

Snow is initially formed in the atmosphere under a variety of different formation mechanisms and is deposited on the sea ice surface. The density of snow varies from (50-500 kg·m^3) and gradually increases with time [24]. In winter, the snowpack has been commonly characterized by three distinctive layers [23], [25]: the new snow layer, the original snow layer, and the basal snow layer. Example grain sizes in each layer are 1-2, 2-4, and 9-20 mm^2, respectively [23].

Once snow has fallen on the sea ice surface it undergoes a series of thermodynamic metamorphisms. The growth processes and temperature gradient in the snow cover determine the size and shape of the crystals. Temperature gradient metamorphism has the most significant impact on grain size. The grain growth occurs when wetness is present and the temperature gradient is high enough. In the absence of a large temperature gradient the snow grains grow slowly and equally in all directions, resulting in well rounded crystals, known as an equilibrium form of snow [26]. In contrast, kinetic growth forms have a fast growth rate, with a dendritic structure or largely faceted shapes. A large temperature gradient combined with high vapor flow results in high vapor pressure and fast growth [26]. Kinetic growth processes result in a wide range of faceted crystal types, including scrolls, cups, plates, sheaths, needles, and the well-known hexagonal snowflake [26].

During the cold winter season, the bottom of the snowpack is warmer than the top due to the thermal conductivity blanketing effect, resulting in upward vapor transport. Kinetic growth takes place in the basal layer at the bottom of the snowpack where the

larger grains grow at the expense of the smaller grains. Additionally, the basal layer of the snowpack is saline due to brine wicking from the sea ice surface and potentially from an old layer of frost flowers which can be incorporated into the overlying snow accumulation. The snow grains near the surface of the snowpack are typically more rounded grains and are not very likely to form kinetic growth forms due to colder temperatures. A typical profile of the snow pack would show an increase in grain size when moving from the air - snow interface surface down to the snow - ice interface, whereas the density would show a decrease since the grains cannot be packed together as tightly.

Wet snow can be classified into two separate regimes based upon the amount of liquid content. The pendular regime is defined by the condition when water can stay in the interstices of the snow and the liquid water content is up to 7%, whereas the funicular regime occurs when the water begins to drain, at liquid water content greater than 7% [26]. Snow in the pendular regime consists of clusters of grains, which form quickly when the snow is first wetted and results in grain growth increase [26]. In the funicular regime the snow is a two phase system with individual spherical grains and the pore space between the grains containing liquid water.

Snow crystals may be formed from a variety of processes, resulting in a complex grain structure. Melt-freeze crystals can form due to cycles of temperature, forming multi-crystalline portions. Melt layers on the snowpack surface or at the base of the snowpack can refreeze and generate a complicated crystal structure. Wind crusts

Fig. 2.3: Close-up pictures of frost flowers that were observed on newly-forming sea ice during the CFL project.

may form at the surface due to ice particles breaking into smaller pieces and packing densely. Surface glaze forms from rainwater, creating a smooth, impermeable surface.

Frost Flowers

Frost flowers are a salient feature in the winter Arctic, which form rapidly on new sea ice under calm conditions. They are characterized by their high salinity (2-3 times oceanic values) and by their crystal growth habits such as clumps, dendrites growing on rods, hexagonal plates, or needles. It is postulated that they are formed when the brine skim layer and cold temperatures provide a region of supersaturated vapor [27] and small-scale roughness provides nucleation sites for the ice crystal formation [28]. The frost flowers wick up brine rejected by the sea ice through surface tension. The surface brine comes from the interior based upon simple kinetic processes [28]. Observations have shown that the flowers insulate the ice surface from the colder air by several

degrees. In addition, radar measurements are sensitive to the presence of the frost flowers, showing an increase in backscatter when the flowers are present. An example close-up picture of frost flowers growing on newly-forming sea ice during the fall period of the CFL project is shown in Fig. 2.3

2.2 Microwave Remote Sensing of Sea Ice

The purpose of active microwave remote sensing of sea ice is to obtain information on the geophysical or thermodynamic state of the sea ice through radar measurements. The physical makeup of the sea ice fabric and snow cover can be converted into an electrical description by assigning a dielectric constant to each of the constitutive components. The propagation of electromagnetic waves in the sea ice medium is therefore dependent upon the radar system parameters and the sea ice dielectrics, the latter of which are affected by the thermodynamics as will be discussed in Section 2.3.2.

In this section we will present the connection between the geophysics of sea ice and remote sensing variables. We begin by presenting Maxwell's equations and the wave equation. Next, we will show the conversion of the physics of the sea ice to an electrical quantity through a description of the dielectric concept. Following this, we present some details on how electromagnetic waves are used in radar systems to characterize a target, including a description of the polarimetric response of an area-extensive target, such as sea ice. The fundamentals of surface and volume scattering are presented. Finally, we will show the scattering signature dependence of sea ice

through a discussion of sea ice physics and corresponding radar signatures.

2.2.1 Maxwell's Equations and the Wave Equation

Maxwell's equations, together with the constitutive relationships, completely describe the macroscopic behavior of electromagnetic waves [29]. Maxwell's equations presented in differential form are:

$$\nabla \times \mathbf{E} = -\frac{\partial \mathbf{B}}{\partial t} \tag{2.4}$$

$$\nabla \times \mathbf{H} = \mathbf{J} + \frac{\partial \mathbf{D}}{\partial t} \tag{2.5}$$

$$\nabla \cdot \mathbf{D} = \rho \tag{2.6}$$

$$\nabla \cdot \mathbf{B} = 0 \tag{2.7}$$

where $\mathbf{E}$ is the electric field intensity in [V/m], $\mathbf{H}$ is the magnetic field intensity in [A/m], $\mathbf{D}$ is the electric flux density in [C/m ^{2}], $\mathbf{B}$ is the magnetic flux density in [T], $\mathbf{J}$ is the current density in [A/m ^{2}], and ρ is the volume density of charges in [C/m ^{3}]. The constitutive relationships are given as:

$$\mathbf{D} = \epsilon \mathbf{E} \tag{2.8}$$

$$\mathbf{B} = \mu \mathbf{H} \tag{2.9}$$

$$\mathbf{J} = \sigma \mathbf{E} \tag{2.10}$$

where all bolded terms were previously defined, and ϵ is the permittivity in [F/m], μ is the permeability in [H/m], and σ is the conductivity in [S/m].

The wave equation may be derived from Maxwell's equations. If the media is assumed to be linear, isotropic, and homogeneous, non-conducting media, by manipulation of Maxwell's equations the following homogeneous vector wave equation for a source-free region can be derived:

$$\nabla^2 \mathbf{E} - \frac{1}{v^2} \frac{\partial^2 \mathbf{E}}{\partial t^2} = 0 \tag{2.11}$$

where v is the velocity in the medium in [m/s].

Polarization and Plane Waves in Layered Media

A monochromatic electromagnetic wave can be described by its magnitude, phase, and polarization. For a transverse electromagnetic (TEM) wave, with a field configuration such that the electric and magnetic fields vectors lie in parallel equiphase planes, the TEM wave is considered to be a plane wave. A plane wave is said to be uniform if the magnitudes of the field components are also constant on the equiphase plane.

A plane wave that is traveling in the negative z-direction is said to be "vertically polarized" or "TM" if the electric field vector lies in the plane of incidence. The electric field vector then has an x and a z-component. Similarly, the wave is said to be "horizontally polarized" or "TE" if the electric field vector is perpendicular to

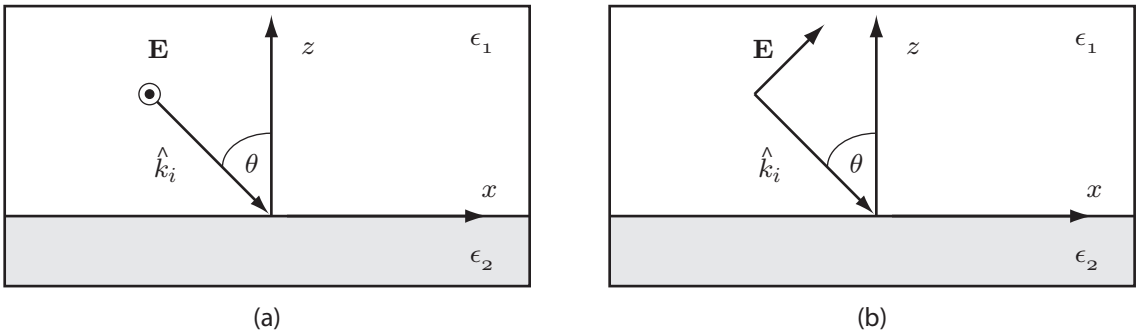

Fig. 2.4: Orientation of electric fields for oblique incidence on a semi-infinite planar medium. a) Horizontally polarized, b) vertically polarized.

the plane of incidence. This is shown in Fig. 2.4, where a) shows the horizontally polarized case and b) shows the vertically polarized case of oblique incidence on a semi-infinite planar medium.

When a plane wave is obliquely incident upon a lossy dielectric interface, some of the energy is transmitted and some is reflected with the interactions described in terms of the Fresnel reflection coefficients. Details of time-harmonic wave propagation through layered material media are well-known and thoroughly discussed in the literature. Our work focuses on the time-domain solution, and so, details of the solution to wave propagation through multi-layered media that are specific to our developed methods are presented in Chapter 4.

2.2.2 Dielectric Properties of Snow and Sea Ice

When a material is subjected to an electric field, small displacements in the bound charges of the material result in a general polarization of the media. The electric flux

density, denoted **D**, gives a divergence relationship between the "free charges" of a medium and the electric field. More specifically, where **P** represents the polarization vector due to an applied field, the electric flux density is given as:

$$\mathbf{D} = \epsilon_0 \mathbf{E} + \mathbf{P} = \epsilon_0 \epsilon_r \mathbf{E}, \tag{2.12}$$

and the divergence of the electric flux density is equal to the total charge enclosed, that is,

$$\nabla \cdot \mathbf{D} = \rho. \tag{2.13}$$

There is an inertia in the charged particles that prevents them from keeping up with the frequency of the electric field. It is this inertia which creates a damping mechanism and therefore energy loss. If there are free charge carriers, there are also ohmic losses. Both damping and ohmic losses are contained in the imaginary part of the complex permittivity.

Pure Water

Pure water is a substance whose molecules have a permanent dipole moment [30]. The relative dielectric constant of pure, unbound, liquid water is given by the Debye

relation, which shows a frequency dependence of the dielectric constant:

$$\epsilon_w(\omega) = \epsilon_{w,\infty} + \frac{\epsilon_{w,s} - \epsilon_{w,\infty}}{1 + j\omega\tau_w}. \tag{2.14}$$

The value of the high frequency relative permittivity, $\epsilon_{w,\infty}$, is typically set at 4.90, with a temperature dependence that is very weak and henceforth neglected. The value of the low frequency, or static relative permittivity, $\epsilon_{w,s}$, is a function of temperature, following an exponential form. The relaxation time, τ_w, is closely related to the relaxation frequency, $f_0 = 1/(2\pi\tau)$, which is at about 17 GHz for water at room temperature. The relaxation frequency is the frequency at which the imaginary part of the permittivity (dielectric loss) achieves its maximum. A diagram known as a Cole-Cole plot can be used to show the variation of the real and imaginary components of the permittivity as a function of frequency [31]. It is important to note that there is a distinctive difference between bound water and unbound water. Bound water refers to water that is trapped within another material, such as water in soil. The response of the water molecules to the electric field are no longer the same since the molecules stick to the surfaces of the other components in a phenomenon known as "adsorption."

Saline water is a substance that contains dissolved salts. The amount of salt in the saline water is typically reported in units of parts per thousand [ppt], or practical salinity units [PSU]. The Debye relation can be modified to include the conductivity,

as follows:

$$\epsilon_{sw}(\omega) = \epsilon_{sw,\infty} + \frac{\epsilon_{s,sw} - \epsilon_{\infty,sw}}{1 - j\omega\tau_{sw}} + j\frac{\sigma}{\omega\epsilon_0} \tag{2.15}$$

Pure Ice

Pure ice, or freshwater ice, is a very different substance from liquid water. Ice is a solid, and so, the crystallographic structure may affect the effective dielectric constant. Pure ice follows a Debye behavior, but since its relaxation frequency is much lower than liquid water (7 kHz at 0°C and decreasing with temperature) it is rather dispersionless at microwave frequencies and is only slightly dependent upon temperature. An empirical equation describing the relative permittivity of pure ice as a function of temperature (in °C) was determined by Mätzler [32]:

$$\epsilon_{ice} = 3.1884 + 0.00091T \tag{2.16}$$

There is some debate as to the validity of the Debye behavior for the loss factor (imaginary part), but typically it is relatively small in the microwave regime ($10^{-3} - 10^{-2}$).

Sea Ice

Sea ice is a very complex substance to model in terms of the dielectric properties since it is an inhomogeneous medium. Typically, it is considered to be a pure ice background, or host material, with brine and/or air bubble inclusions. Various

approaches have been taken to describe the effectively random medium, which are discussed in Section 2.3.2. The brine pockets are of key importance in describing the dielectric properties of the sea ice medium. They have a very high dielectric constant compared to the ice background medium and therefore act as scattering centers.

Within the sea ice, the dielectric constant of the brine inclusions is calculated using the temperature and the number of inclusions is estimated using the temperature and salinity of a given ice sample. The dielectric constant of brine trapped within sea ice was studied intensively by Stogryn and Desargent [33]. They fit a Debye-type relationship similar to that of seawater which associates the variation of permittivity with frequency. Their equations give values for the static permittivity ϵ_s, high frequency permittivity ϵ_∞, relaxation time τ in [ns], and conductivity σ in [S/m], as:

$$\epsilon_s = (939.66 - 19.068T)/(10.737 - T) \tag{2.17}$$

$$\epsilon_\infty = (82.79 + 8.19T^2)(15.68 + T^2) \tag{2.18}$$

$$2\pi\tau = 0.10990 + 0.13603 \times 10^{-2}T + 0.20894 \times 10^{-3}T^2 + 0.28167 \times 10^{-5}T^3 \tag{2.19}$$

$$\sigma = -Texp(0.5193 + 0.08755T) \tag{2.20}$$

These equations are valid for temperatures greater than -25°C and the units of T are in °C. There is both a temperature dependence and a frequency dependence in the dielectric constant of the brine for both the real and imaginary components.

Snow

The dielectric properties of snow are governed by the dielectric properties of ice, the density of the snow, and the shape of the snow grains. Due to the fact that the dielectric of ice is basically frequency independent and only slightly temperature dependent, the dielectric constant is effectively based upon the density of the snow. The dielectric properties of snow on sea ice have been studied extensively both in modeling and field studies; however, due to variations in the snow morphology as discussed in Section 2.1.5, it is difficult to perfectly match theoretical calculations of dielectrics to the measured values in all cases. One study of snow dielectric properties was conducted by Tiuri *et al.* [34] that involved a series of cylindrical cavity resonator measurements to determine the dielectric constant. They found that the real part of the dielectric permittivity of dry snow was independent of almost every parameter, with the exception of density, which gave the following empirical polynomial fits:

$$\epsilon'_{ds} = 1 + 1.7\rho_{ds} + 0.7\rho_{ds}^2, \tag{2.21}$$

$$\epsilon''_{ds} = (0.0008)(0.52\rho_{ds} + 0.62\rho_{ds}^2), \tag{2.22}$$

where ϵ'_{ds} and ϵ''_{ds} are the real and imaginary components of the dielectric constant of dry snow and ρ_{ds} is the density of the snow.

Wet snow is much more complicated than dry snow – there is a larger frequency and temperature dependence due to the liquid content. Furthermore, the water is

distributed differently throughout the snowpack dependent upon whether the snow is in the pendular or funicular regime and the presence of brine further exacerbates the situation. The literature has a variety of empirical models that have been proposed for different frequencies and snow properties, for example, see [31].

2.2.3 Polarimetric Radar Measurements of Sea Ice

Radar measurements of sea ice have been used to obtain information about the thermodynamic and physical state of sea ice for many years now. Of primary importance are ice type, ice thickness, thermodynamic state, and physical state. Ultimately, the goal is to use remote sensing to obtain information on the physical parameters which control the electromagnetic scattering. Determining the physical parameters of the sea ice from the radar measurements is an inversion problem with a large number of parameters and has been discussed in the literature [35]. Neural networks and look-up tables are the prime tools that are used for the inversion problem since the real focus is on operational monitoring and observation of changes in the radar signatures. In spite of the difficulty in inverting the data, radar measurements of sea ice have shown that the sea ice features of interest have dominant scattering mechanisms. The backscatter is influenced by the frequency, polarization, and incidence angle of the radar. Different aspects of the sea ice structure also influence the backscatter.

In a monostatic radar system, the transmitted waveform has one polarization and receives in the same polarization. For example, if the system transmits with a

vertically polarized (TM) wave and the received signal is also vertically polarized, then the signal is said to be the "VV return." Similarly, a radar system can be designed to transmit and receive a horizontally polarized (TE) wave to obtain the "HH return." These are termed the "co-polarized returns." Polarimetric radar systems present a large improvement in the data collection capability when compared to single-polarization systems. A polarimetric radar system collects the VV, HH, and VH returns, in addition to the phase difference between the two co-polarized channels.

When considering a discrete target, the complex scattering matrix, $\mathbf{S}$, can be used to describe the relationship between the incident and scattered fields [36], given as:

$$\mathbf{S} = \begin{bmatrix} |S_{hh}|e^{j\phi_{hh}} & |S_{hv}|e^{j\phi_{hv}} \\ |S_{vh}|e^{j\phi_{vh}} & |S_{vv}|e^{j\phi_{vv}} \end{bmatrix} \tag{2.23}$$

where S_{rt} is the received field in polarization r, for a transmitted field t, and r or t may each be h or v. The phase difference between the transmit and receive signals is ϕ_{rt}. Using the following relation, the scattering matrix can be found through transmitting and receiving both vertically and horizontally polarized waves:

$$\mathbf{E}^{sc} = \frac{e^{jkr}}{kr}\mathbf{S}\mathbf{E}^{inc}, \tag{2.24}$$

where $\mathbf{E}^{sc}$ is the scattered electric field and $\mathbf{E}^{inc}$ is the incident electric field.

For an area extensive target, a scattering matrix is measured for each pixel or

resolution element. A covariance matrix is calculated using an ensemble averaging process and assuming that the region that we are illuminating is reciprocal ($S_{vh} = S_{hv}$). The normalized radar scattering cross section (NRCS, and denoted as σ^0 [37]) is computed using the scattered far-field quantities in the following expression [38]:

$$\sigma^0(\theta_{sc}, \phi_{sc}, \theta_{inc}, \phi_{inc}) = \lim_{R\to\infty} 4\pi R^2 \frac{\langle S^{sc}(\theta_{sc}, \phi_{sc})\rangle}{A_0 S^{inc}(\theta_{inc}, \phi_{inc})}, \tag{2.25}$$

where A_0 is the area of illumination, $S^{sc}(\theta_{sc}, \phi_{sc})$ is the scattered power in the direction θ_{sc}, ϕ_{sc}, $P^{inc} = A_0 S^{inc}(\theta_{inc}, \phi_{inc})$ is the incident power, and $\langle . \rangle$ denotes ensemble averaging of the quantity within the angled brackets.

The radar signature of an area extensive target describes the variation of the NRCS with incidence angle. Radar signatures are visualized by plotting the NRCS versus the incidence angle of the radar for each available polarization. The variation with incidence angle contains information on the scattering mechanisms (e.g. surface and volume), types of surface coverage (e.g. bare ice versus frost flower covered sea ice), and thermodynamic state (e.g. dry snow versus wet snow).

Further expressions that are used in addition to σ^0 include the total power, co- and cross-polarized ratios, copolarization correlation coefficient and phase differences [36]. One polarimetric parameter that is used to show similarity in the co-polarized channels and which we utilize in Chapter 3 is the co-polarized correlation coefficient, ρ_{hhvv},

defined as:

$$\rho_{hhvv} = \left| \frac{\langle S_{hh} S_{vv}^* \rangle}{\sqrt{\langle S_{hh} S_{hh}^* \rangle \langle S_{vv} S_{vv}^* \rangle}} \right| \tag{2.26}$$

where S_{rt} are elements of the scattering matrix as previously described. Other polarimetric expressions are given in [36].

2.2.4 Scattering in Snow-Covered Sea Ice

Scattering in snow covered sea ice is a complicated process that can involve scattering from the sea ice surface and from within the sea ice volume itself. The thermodynamic state of the sea ice influences the scattering response due to the relationships with the physical parameters. In fact, there is a seasonal evolution of backscattering signatures that may be observed due to the thermodynamic and physical changes within the sea ice fabric and overlying snow cover.

Surface and Volume Scattering Fundamentals

Surface and volume scattering separately describe the behavior of an electromagnetic wave that is incident upon a geophysical surface. Typically the scattering region consists of a layered medium with rough interfaces and some sort of inhomogeneities within the volume.

Surface scattering considers the interfaces between the layers, with particular attention paid to the interface at the air - sea ice interface. If the surfaces are

perfectly smooth, and if they are assumed to be infinite in extent, then there is no backscatter generated from the interfaces at all. The backscatter must then be completely incoherent. With increasing surface roughness, non-specular scattering begins to take place. When the dielectric contrast is very high, the rough surface scattering tends to dominate the scattering signature since there is not as much energy transmitted into the medium where volume scattering can take place. A good example of a surface scatterer is the ocean surface since there is a high dielectric contrast between the air and the seawater, and seawater is extremely lossy at microwave frequencies.

In volume scattering, a "mean wave" propagates through the background medium. This is commonly termed the "coherent component." The coherent wave interacts with various scatterers within the volume, which results in re-radiation of the energy in a form that is typically out of phase with the coherent component, and is therefore called the "incoherent component." When the medium is not very lossy and the scatterers re-radiate the field multiple times, it is called multiple scattering. However, when a medium is very lossy, usually single order scattering dominates. In Fig. 2.5, a ray-tracing illustration is shown to describe the concept of multiple scattering. In Fig. 2.5(a) a wave is incident upon a half-space of different dielectric constant that is populated with a series of inclusions with yet another dielectric constant. In Fig. 2.5(b) part of the wave is reflected from the surface and part is transmitted into the lower half-space, each with reduced intensity. Upon encountering one of the inclusions the

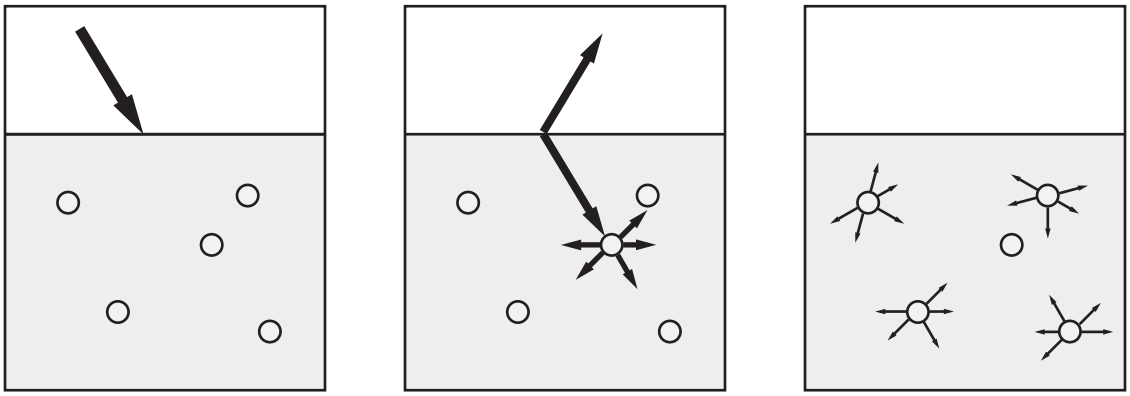

Fig. 2.5: Graphical ray-tracing illustration of multiple scattering. a) Wave is incident upon a half-space, b) wave is reflected by the surface and scattered by an inclusion, c) other inclusions scatter the energy scattered by the first inclusion.

wave is scattered with reduced intensity. In Fig. 2.5(c) the wave that was scattered from the first inclusion has propagated and is scattered once again from the other inclusions.

It is interesting that a medium with a strong volume scattering characteristic does not require a large volume of scatterers. Rather, it is determined by the strength of the individual scatterers and the level of energy absorption within the scattering medium. In volume scattering the permittivity is assumed to vary continuously or to have a discrete distribution of inclusions. The inclusions are often assumed to be canonical in form (for example, spheres and spheroids). The sum of the scattering response of each element is often acceptable for sparse media; however, for dense media, the inter-inclusion interactions and multiple scattering cannot be ignored. Although volume and surface scattering were discussed separately, they are not truly

independent of each other. In fact, they are complexly intertwined and in reality there are complex surface-volume interactions that take place.

Microwave Signatures of Sea Ice

There are many important environmental and physical properties that are relevant to scattering measurements. Important aspects include the temperature, dielectric constant, salinity, snow cover, and surface roughness. The mechanisms under which the ice formed, how it has changed over time, and the age of the ice all are factors in determining the microwave properties and therefore the measured backscatter of the sea ice.

Sea ice classification algorithms have developed to exploit the differences in radar signatures that are observed through the use of different frequencies, polarizations and incidence angles. Open water, newly-formed sea ice, first year sea ice, and multiyear sea ice each exhibit characteristic scattering mechanisms. In first year sea ice the dominant backscattering mechanism is considered to be surface scattering, followed by volumetric scattering from the upper layers of the ice. In contrast, the dominant backscattering mechanism for multiyear sea ice is considered to be volume scattering from the bubbles and secondarily from the surface of the ice [39].

The thermodynamic state of the ice and the type of surface coverage influence the backscattering response of the sea ice. In first year sea ice an increase in temperature can increase the size of the brine pockets as the walls of the pockets melt to seek

thermal equilibrium. The salinity of the brine changes which results in a change in the dielectric constant. Clearly the temperature effect is complex since the dielectric and the size of the scatterers changes with the temperature. This change is also evident in the various types of surface coverage that were previously discussed.

The microwave scattering of sea ice has a large variation with the season and has been presented in terms of the seasonal cycle (for example, [2]). The information in the time series is very important for interpretation of satellite images and for using remote sensing data. For example, the backscattering responses of multiyear sea ice and first year sea ice are very different throughout the winter season due to the different scattering mechanisms, yet during the advanced melt it is difficult to distinguish between them due to the presence of water in liquid phase. Additionally, the determination of the time of fall freeze-up and the spring melt are of interest in studies of Arctic climatology.

2.3 Modeling Aspects for Sea Ice Remote Sensing

Conducting a modeling study for the remote sensing of sea ice requires transforming the physical description of the sea ice through an electric description into a modeling domain. In this manner, the knowledge of the geophysics of the sea ice drives the development and simulation parameters of dielectric models, which in turn drives the scattering models.

In this section we will present some important aspects for modeling the microwave

interactions of sea ice with application to the remote sensing problem. We will start by presenting a cursory overview of past modeling efforts and approaches. Next, we will present some methods for modeling a random dielectric medium, building on the background that was presented in Section 2.2. Finally, we will introduce the finite-difference time-domain (FDTD) and finite-volume time-domain (FVTD) methods, focusing on the salient aspects that are important for modeling the backscattering in a remote sensing problem.

2.3.1 Modeling of Microwave Scattering from Geophysical Media

There are many different formulations of electromagnetic scattering models that have been used to describe microwave scattering from geophysical media. It is a challenging task to decide what level of approximation in the solution method is acceptable and what the fundamental assumptions should be. Simple models have been developed; however, with limited application. At the same time, there are more complex models that take into account more of the governing physics of the interactions with the medium, yet the complexity of the models may outweigh the benefit of using such a model. There is no well-established commercial software package to use that can focus on the remote sensing problem as in other types of electromagnetics problems. In fact, different models may produce reasonable agreement between modeled radar signatures and measured radar signatures, even when assuming different versions of the underlying physics and constrained by the same geophysical data [40].

As mentioned in Section 2.2.4, in modeling the remote sensing problem, both volume and surface scattering must be considered to some extent for a model to be useful and/or valid. To this end, there have been essentially two major classes of models that have been developed in the literature. The major types of models can be classified into Radiative Transfer theory (RT) models and Analytic Wave Theory (AWT) models. RT is based on energy conservation principles and has successfully been applied to scattering problems with highly complex geometries [40]. AWT models are generally more complex than RT and are formulated directly from Maxwell's equations. Both methods have been extensively developed and have been successfully applied in many situations with varying levels of success. For example, AWT models have been used for modeling scattering from a variety of snow and sea ice types by Nghiem [41], while RT models have been used for modeling scattering from soil, snow, and ice (Fung's book provides an excellent overview of RT, providing examples and citing many relevant publications [40]).

The single largest attempt to characterize and model sea ice was performed by the Accelerated Research Initiative (ARI) on the Electromagnetic Properties of Sea Ice (EMPOSI). The results of the ARI are well documented in the Special Section on the Electromagnetic Properties of Sea Ice in the IEEE Transactions on Geoscience and Remote Sensing, Vol. 36, No. 5, 1998 [42]. To date, most of the results are considered as the benchmark for which to base future work. In this study, significant advances were made in understanding the snow and sea ice physics as well as advancing modeling

techniques and theory through linking the research efforts. Important comparisons between laboratory studies and field studies were made and one of the important conclusions was that further modeling studies should be conducted that focus on connecting the sea ice physics with the modeling studies.

An excellent review of models used for microwave remote sensing has been provided in [42]. Examples of some past models that have been used for modeling sea ice remote sensing include models based on AWT (Nghiem [43]), with a part of the model based on strong fluctuation theory (SFT) to calculate the effective permittivities (Stogryn [44]), radiative transfer theory (RT) (Ishimaru [45]), dense medium radiative transfer theory (DMRT). Surface scattering models have also been applied under the geometric optics approximation (GO), perturbation theory (for example, the small perturbation model, SPM, [46]), and integral equation methods (IEM). As an alternative to the AWT and RT formulations, numerical computation methods have been used for simulating the interaction of waves with sea ice. While AWT formulations are generally quite complex, numerical simulation techniques can accommodate variations in complex media descriptions relatively easily. For example, Nassar studied the utility of FDTD for scattering from sea ice [47] and found that he was able to simulate scattering for mid-range incidence angles with some success. Furthermore, fully-developed simulation tools based on AWT and advanced RT models are not readily available, and so, considerable time in developing, debugging, and validating one of the models would be required.

2.3.2 Modeling the Dielectric of a Random Medium

There are many different approaches that may be taken in order to model the dielectric of an inhomogeneous dielectric substance, each with underlying assumptions about the governing physics and often dependent upon the end application of the dielectric model. The effective dielectric consists of a background dielectric constant and a fluctuating component, such that [31]:

$$\epsilon_{eff}(\mathbf{r}, \mathbf{p}) = \epsilon_h(\mathbf{p}) + \epsilon_f(\mathbf{r}, \mathbf{p}), \tag{2.27}$$

where $\mathbf{p}$ is the polarization of the exciting field and $\mathbf{r}$ is the location in space. Therefore the effective dielectric constant is dependent upon the location within the medium and also dependent upon the polarization of the excitation field. The goal of modeling the dielectric of a random medium is to come up with a method to determine the value of the dielectric constant throughout the inhomogeneous medium. There are many approaches to do this, including dielectric mixture models, analytical methods, empirical models, correlation functions, and discrete scatterer methods.

Dielectric Mixture Models

In a mixture model, the permittivity is assumed to consist of a host medium with a variety of inclusions embedded within it, as shown in the left image of Fig. 2.6. We assume that the macroscopic permittivity of the mixture is a function of the

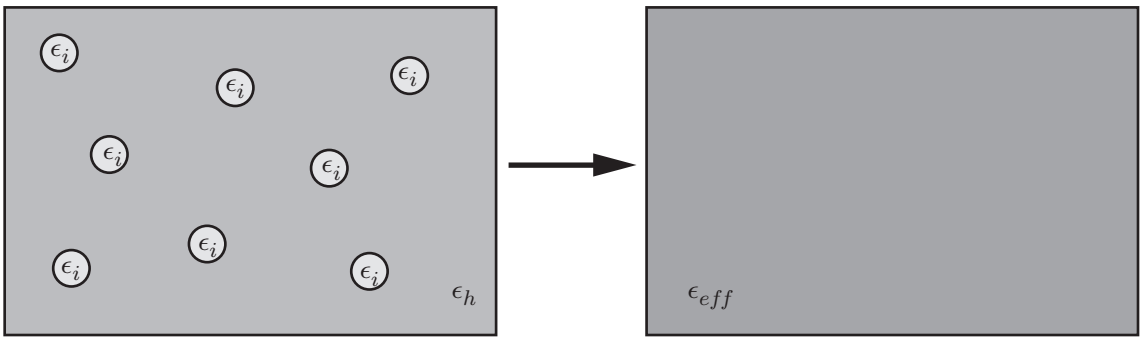

Fig. 2.6: Concept drawing showing how a dielectric mixture replaces the inhomogeneous medium in the left-hand box by the homogeneous medium in the right-hand box.

permittivity of the host medium, the permittivity of the inclusions, and the shape and orientation of the inclusions. Typically the permittivity of the mixture is then calculated by assuming that the inclusions are of some canonical shape, such as a sphere or ellipsoid. Variations include using concentric and confocal ellipsoids, multiple species of scatterers (for example, brine pockets and air pockets), and different assumptions on the interactions of local scattered fields. Generally the polarization due to a single scattering object is calculated under a quasi-static approximation. The summation of a conglomeration of scatterers is calculated, and the effective dielectric constant is calculated.

A large variety of mixture models exist in the literature; however, for sea ice, the most popular tend to be the Polder-Van Santen/de Loor model (PVD) [31] or the Tinga-Voss-Blossey models [48]. The PVD model also goes under the names of the Bruggeman formula, and the effective-medium model [30]. In this thesis we use the PVD model due to its prevalence in the sea ice remote sensing literature.

The following expression for the average dielectric constant of a two-phase mixture was proposed by Polder and Van Santen [31]:

$$\epsilon_{eff} = \epsilon_h + \frac{v_i(\epsilon_i - \epsilon_h)}{1 + A_u(\epsilon_i/\epsilon^* - 1)}, \tag{2.28}$$

where ϵ_{eff} is the effective dielectric constant of the mixture, ϵ_h is the dielectric constant of the host medium, ϵ_i is the dielectric constant of the inclusions, v_i is the volume fraction of the inclusions, and A_u is the depolarization factor of the ellipsoidal particle along its u-axis. In de Loor's modification, he considered $\epsilon^* = \epsilon_{eff}$ in order to account for near-particle interactions. Under the assumption of spherical inclusions, the depolarization factor is $A_u = 1/3$.

The PVD model for spherical inclusions is given by the following expression:

$$\epsilon_{eff} = \epsilon_h + 3\, v_i \epsilon_{eff} \frac{\epsilon_i - \epsilon_h}{\epsilon_i + 2\epsilon_{eff}}, \tag{2.29}$$

where ϵ_{eff} is the effective dielectric constant of the mixture, ϵ_h is the dielectric constant of the host medium, ϵ_i is the dielectric constant of the inclusions, and v_i is the volume fraction of the inclusions. This is a quadratic equation in ϵ_{eff}, which can be solved using simple algebraic manipulation.

Some of the major limitations of dielectric mixture models are discussed in [30]. Dense mixtures cause problems since there are interactions between the scatterers due to near-field effects that are not usually calculated ([48] calculates the second order

scattering). Mixture models work reasonably well for volume inclusions of up to about 10%, above which, the models generally start to degrade due to assumptions about the local polarizing fields [48] and modifications are required. A quasi-static approach is used when describing a dielectric mixture (inclusions are much smaller than the electromagnetic wavelength), meaning that the propagation properties of the fields are neglected. According to Tinga [48], the effective permittivity can only be used when the field is considered to be quasi-static. The quasi-static approach breaks down when the spatial variation of the wave within the medium is large with respect to the scatterer. Since the substance is a mixture, no unique wavelength can be defined, and so, the concept of "large variation with respect to the scatterer" becomes blurred. Variations in the size of scatterers further complicates the problem, as do variations in the canonical shapes that are chosen to represent the inclusions.

In spite of their limitations, dielectric mixture models are quite successful for many remote sensing applications. For example, [49] used a capacitance probe in the field to calculate the dielectric constant of sea ice and was able to successfully match the measurement to model results. We also note that in sea ice, at a frequency of 5.5 GHz (the operating frequency of our instrumentation), the inclusions are so small that the mixture models may be appropriate. A generally accepted assumption is that scattering from air bubbles is important at frequencies above 2-3 GHz, whereas scattering from brine pockets may only be important at frequencies above 20-30 GHz [7].

Analytical Methods

One of the major limitations of a mixture model is that they only provide an estimate of what the effective dielectric should be; however, there can be a range of acceptable values since we are only estimating based upon statistical descriptions of the inclusions. Analytical methods have been used to compute the expected bounds of a permittivity mixture by casting the properties of the ratio of constituent components in an analytic function. Specific assumptions about the geometry of the inclusions are not made. In these methods an integral representation may be used to derive the bounds of validity for the values obtained for the dielectric constant and loss factor. This method has been developed for sea ice by Golden [50].

An example of the bounds for a dielectric mixture are the so-called Wiener bounds:

$$\epsilon_{eff,max} = v_i\epsilon_i + (1 - v_i)\epsilon_h, \tag{2.30}$$

$$\epsilon_{eff,min} = \epsilon_i\epsilon_h/[v_i\epsilon_h + (1 - v_i)\epsilon_i], \tag{2.31}$$

where $\epsilon_{eff,max}$ is maximum value of the effective dielectric constant of the mixture, $\epsilon_{eff,min}$ is minimum value of the effective dielectric constant of the mixture, and the other terms are defined in equation (2.29).

Empirical Models

Empirical models refer to a class of dielectric models that are based on fieldwork or laboratory measurements. When there are many parameters that affect the interaction of the medium with an electromagnetic wave it becomes difficult or impossible to exhaust all possibilities for analytically describing the dielectric behavior. For example, in studies of snow dielectric, the medium is characterized by a large variety of grain shapes, grain sizes, wetness, and brine content as previously discussed. The grains of the snow are, by necessity, in contact with each other in a very complicated manner. However, through measurements, empirical relations can be derived that connect one or more of the physical parameters to the dielectrics within a reasonable error. For example, the cavity resonator measurements of Tiuri [34] provide a relatively simple connection between the density of dry snow to the dielectric constant at microwave frequencies. Indeed, the derived expressions are quite useful and in cases where it is difficult to measure specific parameters on a large scale (such as snow grain size and shape), empirical models should not be dismissed out of hand.

Continuous Random Media Models

Correlation functions for random media are an approach to deal with statistically varying fluctuations of dielectric within a medium. A statistical model describes the variations of the fluctuations in terms of mean, variance, and a spatial correlation function. This is similar to the approach used in random rough surface studies. Due

to the practical difficulties in computations, the scattering is typically taken as first order only; however, this is only a practical restriction and not a requirement by the modeling [5].

Discrete Dielectric Modeling

While dielectric mixture models generally work fairly well, they do suffer from some limitations as discussed previously. There have been a number of studies conducted to study such limitations. As stated by [51], classical mixing formulas fail when the dielectric contrast is high, and/or when the volume fraction of scatterers is high. Studies utilizing numerical techniques such as FDTD have been used to calculate the dielectric constant of a mixture [52]. They find that the simulations result in the classical mixing formulas when the restrictions of low dielectric constant and low volume fraction are satisfied. Moreover, they are also able to extend the range of validity of a mixture model since the simulations that they perform do not neglect multiple interactions. They also find that giving many realizations builds up a good probability distribution for the true value of the dielectric constant of a random medium.

2.3.3 EM Numerical Simulation

Traditionally, the various scientific disciplines have relied on theoretical and experimental methods for understanding nature and natural systems. Modern computers

provide a third, complementary, option – simulation techniques [53]. In some cases, analytic or theoretical approaches are exceedingly difficult to attempt, while on the other hand, experimental work is often difficult to perform and some of the variables are impossible to control.

Electromagnetic simulation methods can be divided into frequency-domain solutions, where a time-harmonic single-frequency solution is found, and time-domain solutions, where a time-dependent solution is found. Whereas more traditional modeling techniques have often relied upon frequency-domain solutions, time-domain modeling has recently seen major growth in application. Frequency-domain solutions were preferred in the past due to their tractability in analytic solutions [54]. However, with today's high performance computers, many algorithms and problem solutions that were intractable before can now be solved. Monte Carlo techniques have been used for random rough surfaces and random distributions of particles with success.

In certain cases, there are some considerable advantages in time-domain modeling over frequency-domain modeling. Time-domain solutions can be more computationally efficient and seem more naturally suited when we seek the transient response in a problem. While it is true that transient responses may be obtained through transformed frequency-domain data, many frequencies are required and a computation performing the transformation to the time-domain is needed. In comparison, the direct time-domain approach provides information on all frequencies (for which the solution is valid) simultaneously. Some problems are better suited to time-domain modeling such

as when we need to simulate large objects and can provide time-gating.

Time-domain modeling is appropriate for the remote sensing problem, whose goal is to measure the backscattering from an area-extensive target. There is an interest in the response at many different frequencies, polarizations, and incidence angles due to the large suite of satellite-based sensors that are currently available.

The Finite-Difference Time-Domain Method

The Finite Difference Time Domain (FDTD) method is one of the most popular time-domain analysis methods for computational electromagnetics. A detailed treatment of the FDTD method is available elsewhere [54] and the literature is full of examples of applications of the method. The FDTD method was first introduced by Yee in 1966 [55] as a method to solve the curl form of Maxwell's equations.

The FDTD method may be best illustrated by an example. Consider one of the equations for the propagation of the TE mode in layered media, (described in greater detail in Chapter 4),

$$\frac{\partial E_y}{\partial z} = \mu_0 \frac{\partial H_x}{\partial t}. \tag{2.32}$$

In order to solve this equation numerically, the expression must be discretized, meaning that we must write the expression as a function of ($k\Delta z$, $n\Delta t$). The spatial dimension, z, is divided into K different locations in the computational space, and the temporal

dimension, t, is divided into N timesteps. Here Δt represents the time discretization and Δz represents the spatial discretization. Furthermore, we follow the approach of Yee and interleave the electric and magnetic field components, placing the magnetic field evaluation points at the $[(k+1/2)\Delta z, (n+1/2)\Delta t]$ locations. A central difference approximation to the previous expression then gives the following expression, which is the update equation for the y-component of the electric field:

$$\frac{E_y|_{k+1}^n - E_y|_k^n}{\Delta z} = \mu_0 \frac{H_x|_{k+1/2}^{n+1/2} - H_x|_{k+1/2}^{n-1/2}}{\Delta t} \tag{2.33}$$

A portion of the computational domain is shown in Fig. 2.7. The electric field components are located on integer multiples of the space and time lattice, whereas the magnetic field components are located on the half locations. The black arrows in the figure indicate the values which are used in the update equation for the electric field at the n^{th} location in z and at the k^{th} timestep. The electric field is updated at the integer k^{th} timestep for all z-locations, graphically from bottom to top in the computational diagram. This is followed by an update of the magnetic field at the $(n + 1/2)^{th}$ timestep using a different update equation (not shown). The updates are performed using the update equations for all z-locations, alternating E and H components, and proceeding from left to right in the computational diagram until the final timestep is reached.

The FDTD method shown here gives an explicit solution (eliminating problems

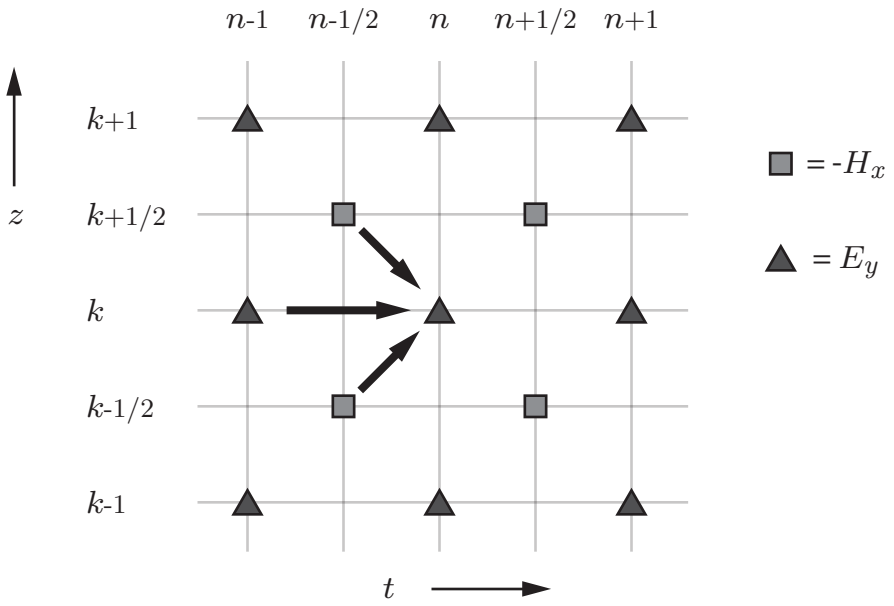

Fig. 2.7: A portion of the computational domain in FDTD graphically depicting the update equation for the E_y component.

with potential matrix inversions), is second-order accurate, and is non-dissipative (the numerical wave does not decay due to some non-physical aspect of the expression). The spacing in both time and space are chosen such that it is stable and numerical dispersion is minimized. More specifically, in terms of stability of the FDTD method, there are limitations on the spatial and temporal discretization that must be observed. The Courant stability limit demands that:

$$\Delta t \leq \Delta z / v, \tag{2.34}$$

where v is the velocity of propagation in the medium, Δz is the spatial discretization, and Δt is the temporal discretization. If the stability limit is not satisfied, then the

solution will grow exponentially to infinity, resulting in a useless simulation result.

A common rule of thumb for stability is to use a discretization that is less than 1/10 of the smallest wavelength that needs to be simulated. More specifically,

$$\Delta z \leq \lambda/10. \tag{2.35}$$

The main limitation of the FDTD method for modeling the remote sensing of sea ice is the cubic lattice structure, which is considered to be a 0^{th} order spatial description. In order to maintain a high order of accuracy in describing the curved surfaces, a large number of very small elements must be used. More elements imply larger computation times. A better approximation could be to use higher order elements, such as 1^{st} order elements as shown in Fig. 2.8. Larger and fewer elements can be used to describe the shape of a curved object in an attempt to maintain higher accuracy. Since most of the objects that we are modeling in sea ice have general curved or undulating surfaces (for example, spherical brine pockets, or rough surfaces), it is logical to seek a method that has the ability to model curved surfaces with fewer elements than the cubic lattice of the FDTD method, such as through the utilization of higher order elements. One such method is the FVTD method.

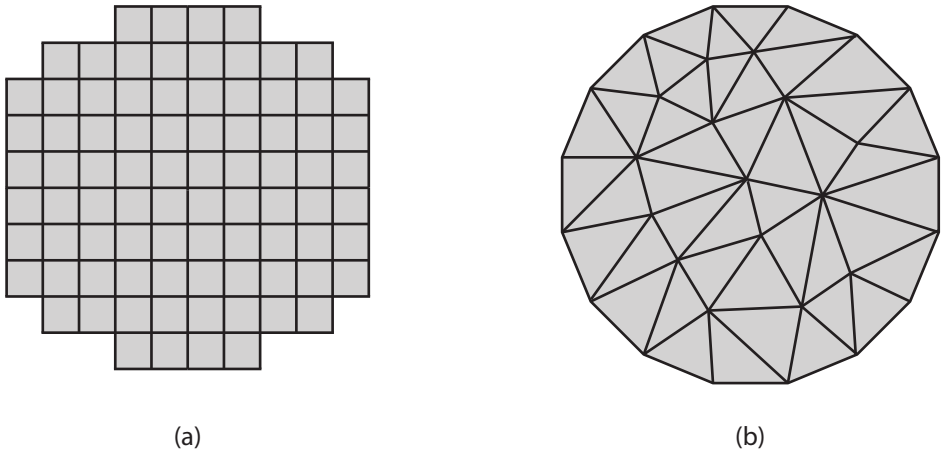

Fig. 2.8: Spatial discretization of a circle showing the difference between a) 0^{th} order spatial approximation, b) 1^{st} order spatial approximation.

The Finite-Volume Time-Domain Method

The finite-volume time-domain (FVTD) method is a robust and flexible scheme for numerically simulating three-dimensional electromagnetic problems [56], [57]. The FVTD method has its origins in the field of computational fluid dynamics and has been used to solve hyperbolic forms of partial differential equations, specifically in the form of conservation laws. One of the advantages FVTD has over the ubiquitous finite-difference time-domain algorithm (FDTD) is that both structured and arbitrary unstructured meshes are equally suitable discretizations for FVTD simulations. This implies that the volumetric mesh can be created to naturally follow oblique surfaces and no alteration to the algorithm is required to compensate for an inaccurate physical model. More details of the numerical algorithm that are relevant to our modeling study are presented in Chapter 4.

Monte Carlo Methods for Remote Sensing Modeling

Monte Carlo methods are defined as "a numerical method of solving a physical problem by the simulation of random variables" [58]. Alternatively, Monte Carlo methods are considered to be a way of numerically solving problems through sampling experiments. These are methods that are associated with random numbers. Historically, the regular use of these methods came from the numerical approaches that were created during World War II in the development of the atomic bomb, and they have been used in many different electromagnetic problems, ranging from potential theory to random rough surface scattering. The name Monte Carlo comes from the association of random numbers with the Monte Carlo casinos in Monaco.

Monte Carlo simulation techniques are considered to be complementary to the notion of conducting true experiments. For example, in making radar measurements of sea ice, many different "looks" with the radar are made in order to build up some statistical significance for our results. Using a Monte Carlo technique to represent the sea ice medium that we are simulating provides a method of emulating the real radar measurements since each random realization also provides a "look" at the location.

Some of the difficulties in applying Monte Carlo techniques are pointed out in [53]. The amount of time to perform simulations and the amount of available memory should be considered before embarking on any project involving Monte Carlo methods. Even if the project can be done, other sources of error must be controlled, such as ensuring that the precision of the computations will be high enough. A decision must

be made on the number of finite statistical samples that will be simulated to reduce error, versus studying the properties of the system with different conditions. For example, we must decide whether it makes more sense to simulate 20 realizations of a random medium at 5 incidence angles, or to simulate 10 realizations of the random medium at 10 incidence angles. In our opinion, it is generally better to have more realizations, or samples, of fewer incidence angles.

A Monte Carlo method for simulating scattering from sea ice using a combination of the FDTD and FVTD methods has the potential to provide new insight and information. Some of the advantages of the proposed technique include:

- Solves Maxwell's equations exactly, within numerical approximation
- Can add an unlimited number of layers to create a random media model
- Can add random inclusions with relative ease
- Can add surface roughness with relative ease
- Can investigate other interesting features, such as cracks and rafting of sea ice

At the same time, there are distinct disadvantages that the using the FDTD-FVTD Monte Carlo model may encounter:

- Proper spatial discretization of the sea ice medium restricts the size of the computational domain

- Monte Carlo techniques can be time consuming and require large computing resources

For context, other researchers have applied the FDTD method to problems involving scattering objects in random media [59] and scattering from objects in stratified media [60]. Uchida [61] has reported on using the FVTD method for scattering from a randomly rough surface at grazing angles with application to communications and found that the results compared favorably with IEM methods. Still other research has been performed that involves the analysis of heterogeneous rough media using FDTD [62]. There was a numerical study of electromagnetic scattering from sea ice using FDTD that is similar to our research [47]. To the best of our knowledge, no one has applied the FVTD method to modeling microwave remote sensing of sea ice.

2.4 Chapter Conclusions and Discussion

This chapter has attempted to give a sufficient overview of the salient aspects of the physical description of sea ice as they pertain to the problem of sea ice remote sensing. Furthermore, significant information on the various methods that are employed in modeling sea ice remote sensing were discussed.

3. POLARIMETRIC BACKSCATTERING SIGNATURES OF NEWLY FORMED SEA ICE

This chapter presents the results and analysis of experimental data that were obtained during our field campaigns in the Canadian Arctic. In terms of our research objectives, a major goal was to collect geophysical and polarimetric scatterometer data over a large variety of sea ice types under an assortment of surface features during the fall freeze-up. Moreover, we wanted to study how the variation in the thermodynamic and physical state of the sea ice is related to the scatterometer signatures.

The main objective of this chapter is to present C-band polarimetric scattering signatures of sea ice during fall freeze-up, obtained using a ship-mounted polarimetric scatterometer, along with their coincident geophysical descriptions. Emphasis is placed on how these polarimetric radar data can be used for improved satellite-based classification of sea ice types. Initially, we present the results of our measurements of the polarimetric radar signatures, differentiating between World Meteorological Organization (WMO) sea ice types that occur during fall freeze-up [63]. Next, an analysis of the relationship of polarimetric parameters (in particular, the co-polarized correlation coefficient, ρ_{hhvv}) to ice thickness is presented. We discuss the implications

of ice floe deformation and surface features in naturally occurring new ice types, including frost flowers. Finally, the variation of parameters within a characteristic floe is addressed with a discussion of the physical state and associated polarimetric radar signatures. An analysis and comparison of the *in situ* measurements with space-borne measurements is assessed in [64].

Material in this chapter has been published in the IEEE Transactions on Geoscience and Remote Sensing [65][1].

3.1 Introduction

The world's attention is now focused on the fact that the sea ice cover in the Arctic is undergoing a rapid state of change. This is largely due to the reduction in thickness and aerial extent of multiyear (MY) sea ice [66]. It is important to note that this change in MY ice is concomitantly associated with an increase in the presence and aerial extent of much younger, and much more saline, first-year sea ice types. The presence of high brine concentration types of sea ice, at a time and location where thicker, and much lower salinity, ice previously existed has significant implications for fluxes of gas, mass, energy, and momentum within the Arctic and also has commensurate effects on physical, biological, and biogeochemical processes operating across the ocean-sea ice-atmosphere (OSA) interface [67]. Microwave remote sensing can play a key role in

[1] © 2010 IEEE. Reprinted, with permission, from D. Isleifson, B. Hwang, D. G. Barber, R. K. Scharien, and L. Shafai, "C-band Polarimetric Backscattering Signatures of Newly Formed Sea Ice During Fall Freeze-Up," *IEEE Trans. Geosci. Remote Sens.*, vol. 48, no. 8, pp. 3256-3267, 2010.

understanding these changes (see for example [2]). Additionally, there is likely to be an increase in demand on operational ice charting to support ice activities that will rely heavily on space-based SAR and the ability to interpret ice conditions from these data.

The fall freeze-up in the Arctic is a critical time of year to study due to the rapid changes that occur in the thermodynamic balance of the OSA system. In light of the recent and dramatic reduction in sea ice extent and thickness [1], new observation techniques are needed to improve our understanding of the observed changes and development of a capability to precisely monitor these changes into the future. Satellite SAR measurements during this period are difficult to interpret since the freeze-up occurs at different rates in different locations creating high variability between ice types within the SAR footprint. As such, *in situ* scatterometer measurements can aid in providing relative calibration data for satellite monitoring since the radar can be positioned to measure only one specific ice type at a given time, rather than integrating a mosaic of different ice types.

Detailed polarimetric microwave backscatter data by sea ice type is limited in the literature (a good summary is provided in [68]), however its potential for improving sea ice type discrimination has not been fully explored. Field campaigns, which combine the *in situ* geophysical measurements with polarimetric radar measurements, provide useful data for validating existing satellite algorithms and baseline data for the development of new algorithms. It has been suggested that there is likely

more discrimination capability through the use of different frequencies rather than different polarizations [36]; however, the availability of space-borne polarimetric data is relatively new and the addition of *in situ* data is still quite useful for modeling studies and satellite validation. Moreover, multi-frequency capability from different sensors lacks contemporariness, and its applicability is limited over the mobile ice pack.

Ice thickness can be estimated for thin ice types (<12 cm) through the use of prior knowledge of sea ice type combined with polarimetric radar measurements [69]. Improved retrieval of sea ice thickness through radar measurement would provide valuable data for studies of sea ice thermodynamics, dynamics, and climatology studies. Ice thickness governs the energy balance of the OSA interface through modulation of the short-wave and long-wave fluxes, in addition to sensible heat, and therefore plays a role in the thermodynamic evolution of the sea ice. The deformation and motion of sea ice is influenced by the thickness and mass of the ice volume. Climatology studies indicate that the spectral albedo is impacted by the thickness of the sea ice, with thin new sea ice absorbing more energy than thick first year sea ice [70]. Sea ice thickness plays a role in each of these aspects, yet from an operational perspective the retrieval of sea ice thickness is not yet reliable under all surface conditions and deformation mechanisms. Sea ice altimetry has been used to estimate sea ice thickness from its freeboard measurement and has demonstrated the recent thinning of sea ice, yet it has typically been focused on large-scale temporal and spatial variations [66].

Previous studies have succeeded at retrieving the thickness in a laboratory setting using C-band scatterometer measurements [69], [41]; however, *in situ* sea ice is subject to many different environmental factors and therefore there is more uncertainty in the thickness retrieval. Consequently *in situ* measurements of sea ice thickness and thermo-physical properties, coupled with polarimetric radar measurements are useful for validation of inversion algorithms and estimation techniques.

Detailed thermodynamic and physical measurements of the frost flower covered sea ice, coupled with the associated polarimetric radar measurements, are useful for sea ice type discrimination. Frost flowers, which are formed through the deposition and crystallization of water vapor and subsequent wicking up of brine [28], are known to have a major impact on the measured scattering response, enhancing the backscatter by as much as 6 dB [71]. Past laboratory studies of frost flower covered sea ice have quantified the radar sensitivity at C-band; however, a quantitative description of the effects of the frost flower coverage under differing surface conditions - such as when there is a light snow cover on the frost flower covered surface - on C-band radar signatures is required for similar sea ice types.

In spite of the fact that different parts of a single floe of sea ice can grow under similar environmental conditions, slight differences in radar measurements across the floe are indicative of slight variations in the thermodynamic, physical, and morphological state of the ice. This is particularly true during the fall freeze-up. In particular, variations in the surface snow cover, environmental forcing, and dynamics create small

scale deviations of the dielectric constant and surface roughness within the measured polarimetric signatures [72], [73]. For example, the formation and distribution of frost flowers upon a sea ice surface can vary depending upon where the frost flower nucleation sites are located on the floe, while wind can cause a deterioration and compaction of the delicate crystal structures. Each ice type within the satellite footprint contributes a different level of backscatter, and therefore the satellite measurement takes an average of the relative contributions. However, even one single ice floe of a relatively uniform similar physical description produces variation within the observed backscattering signal. Quantification of the variation can help with sea ice type discrimination.

3.2 Methods and Techniques

3.2.1 Study Area

The main study area covers the Cape Bathurst polynya in the southeastern limit of Beaufort Sea in the Canadian Arctic, as shown in Fig. 3.1. The ice station data used in this paper are from three different Arctic expeditions, spanning 2003-2007. A total of 16 ice stations with associated scatterometer measurements took place in the Cape Bathurst polynya during October to November 2003 as a part of the CASES (Canadian Arctic Shelf Exchange Study) project. Four ice stations occurred in McClintock Channel in September 2006 as part of the ArcticNet 2006 project, which

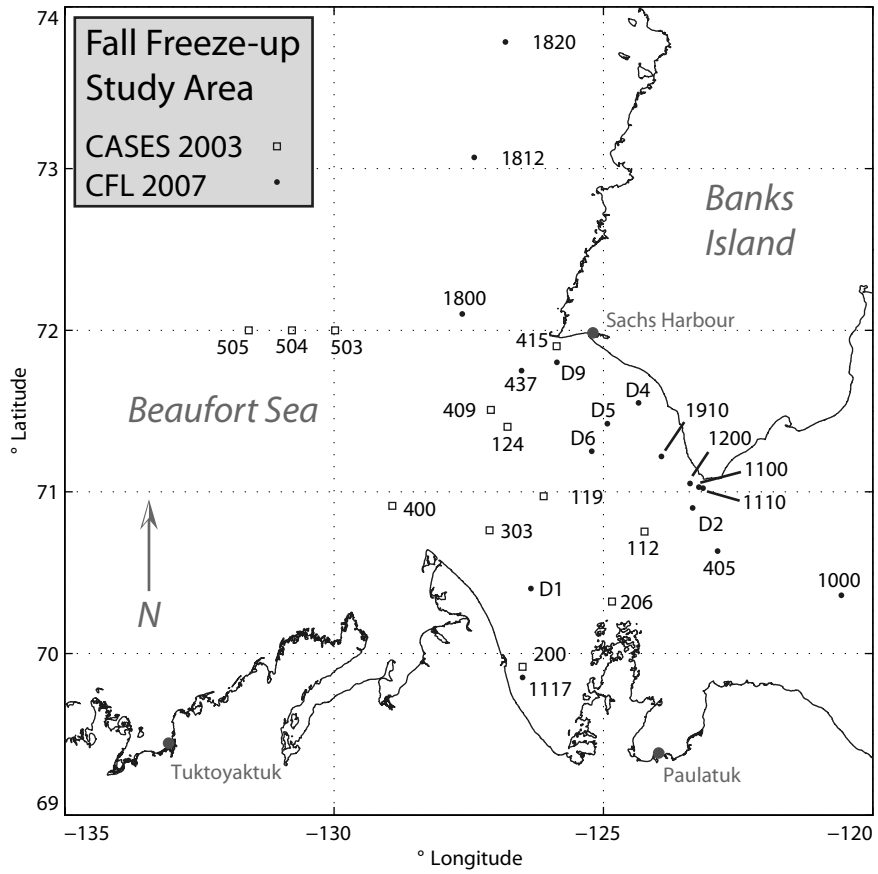

Fig. 3.1: Map showing the location of the stations in the CASES and CFL field campaigns during the fall freeze-up. CASES stations are denoted by a box and CFL stations are denoted by a dot.

covered the measurement of open water and grease ice[2]. Although the measurements from the ArcticNet 2006 project are not from the same geographical region as the other measurements, scattering responses of open water and grease ice are mostly influenced by environmental conditions (i.e. wind speed), and so, provide comparable data since the same wind conditions could easily occur in the Cape Bathurst polynya. A total of 20 ice stations took place in the Cape Bathurst polynya during October to December 2007 as part of CFL (Circumpolar Flaw Lead) system study. A summary of the station names, date of sampling, ice type, thickness, and surface description are provided in Table 3.2 and Table 3.3. The percentage coverage of frost flowers was estimated from surface photography and is indicated in parenthesis beside the surface type "Frost Flowers". Stations from the ArcticNet 2006 project are not included on the map in Fig. 3.1 since they lie within McClintock Channel. Fig. 3.2 gives a mosaic of pictures for typical examples of the ice types that were encountered for a visual reference.

3.2.2 C-band Scatterometer System

The C-band polarimetric scatterometer system was mounted on the port side of the icebreaker CCGS *Amundsen* at a height of about 8 m with respect to the sea surface. A picture of the system in operation is given in Fig. 3.3. The system operates with a center frequency of 5.5 GHz and a bandwidth of 500 MHz. The antenna was a

[2] A study on the properties of MYI during the ArcticNet 2006 project is given in [74]

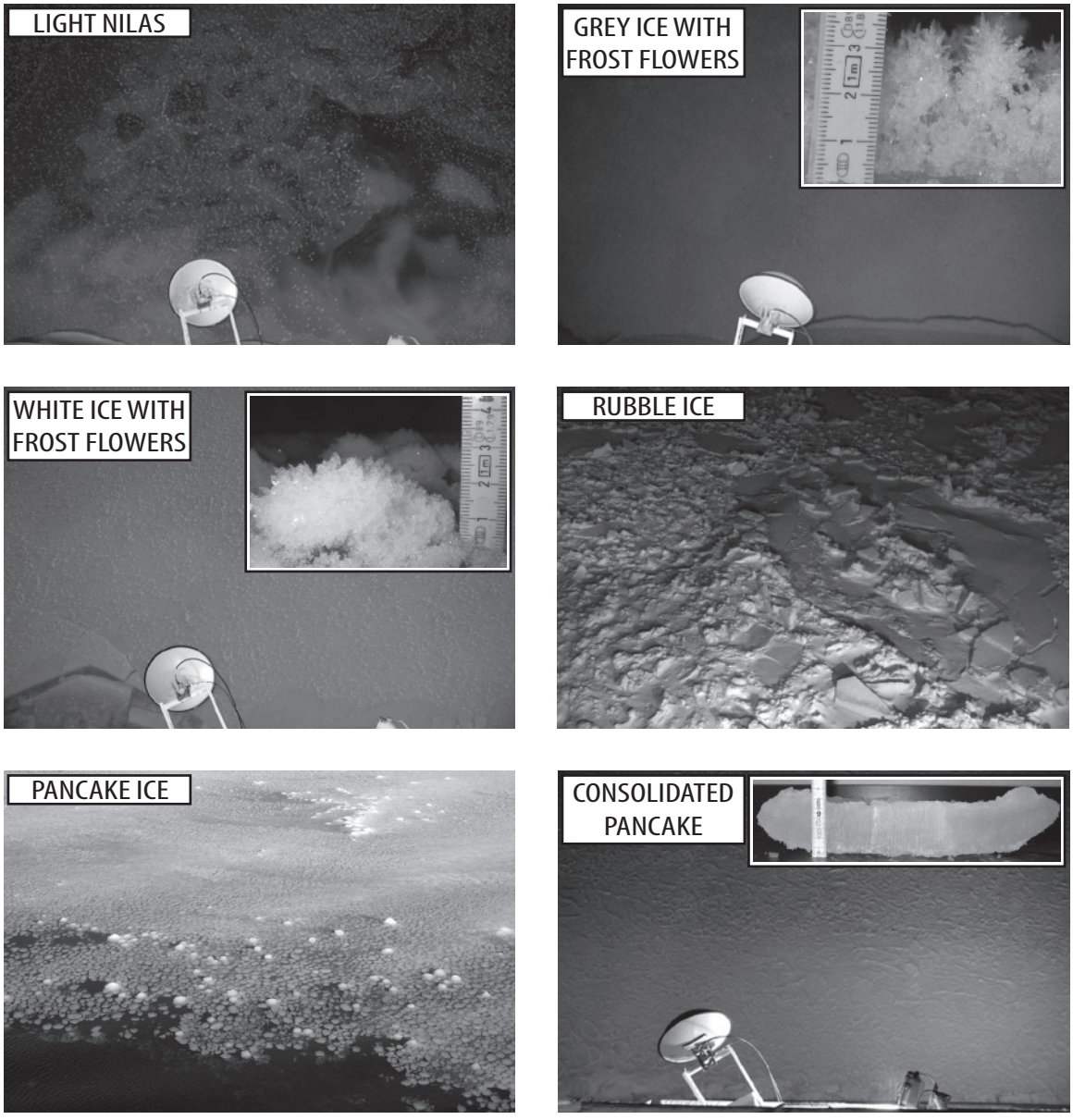

Fig. 3.2: Mosaic of typical examples of sea ice types encountered. Main pictures were taken from the CCGS *Amundsen*, while inset pictures were taken *in situ* or in the laboratory.

Fig. 3.3: The C-band polarimetric scatterometer system, mounted on the port side of the CCGS *Amundsen* and overlooking a multiyear sea ice floe.

dual-polarized reflector with a beamwidth of approximately 5.5° in both the E-plane and H-plane. The system parameters are summarized in Table 3.1. Measurements were conducted in 60° azimuth swaths over a 20° to 60° incidence angle range with a 5° increment. The returned power and phase information was measured, and the covariance matrix was calculated allowing σ^0_{VV}, σ^0_{VH}, and σ^0_{HH} normalized radar cross sections (NRCS) and various polarimetric parameters to be obtained. In the context of our work, the radar signature is defined as a plot of the NRCS as a function of incidence angle.

Our measurements were made at a range slightly less than that of the far-field

Tab. 3.1: C-band Scatterometer Operating Parameters

Parameter	Value
Center Frequency	5.5 GHz
Bandwidth	500 MHz
Antenna Type	Parabolic Reflector
Antenna 3-dB Beamwidth	5.5°
Antenna Gain	28 dBi
Cross-polarization Isolation	>28 dB
Estimated Sensitivity	-40 dB
Transmit/Receive Polarizations	HH, VV, HV, VH

range of the antenna, and therefore we are accepting that the phase error will be slightly larger than the $\lambda/8$ error given by the $2D^2/\lambda$ criterion, where D is the antenna aperture diameter. In terms of near-field correction, we note that the difference between near-field and far-field is essentially a definition of the error in the phase. Regarding the near-field correction implemented in [75], we observe that their correction factor is around 0.25 dB at a range of 7 m and is monotonically decreasing with increased range ([75], Fig. 3). Our range is greater than 8 m, and so, any correction factor would be negligible and likely less than other measurement errors.

Taking the average incidence angle of 45° and a half-power beamwidth (HPBW) as approximately 6° (slightly larger than the actual) we obtain an average footprint size of about 1.1 m^2. The size of the footprint of the antenna is a function of incidence angle since the region of illumination increases with increasing angle. As the incidence angle increases during the radar measurements, there are a larger number of scattering centers that contribute to the measured backscattered field. In processing the data, we take the footprint size into account through a range-binning procedure.

The raw data is processed into range profiles and these profiles are averaged in the azimuth for each incidence angle that is measured. In processing the range profiles for the calculation of the backscattered fields, we ensure that an adequate signal to noise ratio (typically >10 dB) is maintained. At the end of the processing, we must make some sort of estimate of the average noise floor, and therefore we use the specified instrument sensitivity for this value. It is assumed to be reasonable for both the co- and cross-polarized terms, and across all incidence angles. In comparison with the noise-equivalent sigma-zero (NESZ), we note that the noise floor of the scatterometer system is typically lower than that of conventional space-borne SAR systems.

3.2.3 Field Sampling Methods

Each target ice floe (see Table 3.2) was visually selected to have a relatively homogeneous surface (spatially). Typically, five sets of scatterometer measurements were collected at each location to ensure that a statistically significant number of independent samples of a floe were obtained. Following scatterometer measurements, physical sampling of sea ice was conducted within the footprint. Digital photographs of the ice floe accompanied a record of qualitative observations of surface conditions. To record the areal coverage of frost flowers, we took pictures of the surface with meter-sticks visible for scaling. Frost flower coverage estimations were made using image analysis software (ImageJ ©). In each image the approximate area covered by each individual frost flower was calculated by manually drawing an ellipse over the

frost flower. The sum of the area of these ellipses was calculated using ImageJ © and subsequently divided by the total area in the picture to give the approximate areal coverage. Close-up pictures were taken (with a ruler in the picture as a calibration measure) to record crystal structure, height, and vertical structure (e.g. presence of slush layer) of the frost flowers. The samples of frost flowers were carefully taken using a metal spatula and were placed into water-tight bags to take salinity measurements in the lab. Standard snow pit measurements (with temperature profiles at 2 cm intervals, salinities at 2 cm intervals, and snow grain pictures) were obtained to characterize the snow cover, with particular attention made for snow basal layer thickness. After snow pit measurements, samples of ice surface (i.e. scrapings of the top 2.5 mm) were taken for the salinity measurements (S_{si} in Table 3.3).

Air temperature was taken by holding a hand-held temperature probe (Traceable © Digital Thermometer, Control Company, accuracy ± 0.05°C) approximately 1 m above the ice surface (T_{air} in Table 3.2). Temperatures at the air-frost flower or air-snow interface were taken by placing the probe on the top of frost flower or snow. Temperatures at the frost flower-ice or snow-ice interface were taken by placing the probe in between (T_{si} in Table 3.3). For thick snow, a temperature profile was taken at a 2 cm interval. Ice temperature profiles were taken by inserting the probe into the hole drilled to the center of the ice core, extracted by an ice coring system (Mark II, Kovacs Enterprises). Ice temperatures were measured at a 5 cm interval, starting from the bottom to the top of the ice. Ice thickness was measured from the extracted

core using a meter-stick (d_{ice} in Table 3.2).

Extra ice cores were placed in plastic sleeves and stored in a -20°C freezer for further salinity and texture analysis. The ice core was sliced into 5 cm segments (i.e. 5 cm tall cylinders) in the -20°C cold lab onboard the ship. The outer edges where the ice core had contacted the sea water were trimmed away in order to minimize the effects of the exposure. These samples were allowed to melt in plastic containers at room temperature and the conductivity was measured by using a conductivity meter (Hach Sens Ion 5 ©). The salinities of the samples were calculated from the conductivity according to the formulation of [76]. More detailed description of physical sampling procedure is available elsewhere (e.g. [77]).

Ship-based meteorological data were collected through a ship-based AXYS Automated Voluntary Observation Ship system (AVOS). This system is mounted approximately 20 m above sea level on the wheelhouse to minimize the ship's influence and can measure air temperature and wind speed. The measurements are continuously monitored and updated every 10 minutes on a display monitor located within the wheelhouse.

Tab. 3.2: Summary of Ice Stations and General Descriptions.

Station ID	Date	T_{air} [°C]	d_{ice} [cm]	WMO Definition
ArcticNet 101A	18-Sep-06	0.1	0	Open Water
ArcticNet 101B	18-Sep-06	0.1	0	Open Water
ArcticNet 109	17-Sep-06	0.0	0	Open Water
ArcticNet 308.5	24-Sep-06	0.3	2	Grease Ice
CFL 1000	26-Oct-07	-2.5	2	Pancake
CASES 200B	24-Nov-03	-11.7	3	Dark Nilas
CFL 2007D2	29-Nov-07	-17.1	4	Dark Nilas
CFL 1800C	26-Nov-07	-15.6	5.5	Dark Nilas
CFL 1200	20-Nov-07	-15.2	6	Consolidated Pancake
CASES 112C	28-Oct-03	-8.1	7-11	Consolidated Pancake
CASES 124C	26-Oct-03	-5.0	8.5	Light Nilas
CASES 124A	26-Oct-03	-5.0	8.5	Light Nilas
CFL 1110	27-Oct-07	-8.6	8.5	Light Nilas
CFL 1800B	26-Nov-07	-17.4	9	Light Nilas
CASES 119	27-Oct-03	-8.0	9	Light Nilas
CASES 409	06-Nov-03	-6.8	13-16	Consolidated Pancake
CASES 206A	01-Nov-03	-6.6	14	Grey Ice
CASES 415	07-Nov-03	-12.9	14	Grey Ice
CASES 504	24-Oct-03	-5.0	14-21	Consolidated Pancake
CASES 503	25-Oct-03	-4.9	15-21	Consolidated Pancake
CASES 200C	04-Nov-03	-12.0	19	Grey-White Ice
CASES 505	24-Oct-03	-4.1	19	Grey-White Ice
CASES 206B	01-Nov-03	-6.2	19	Grey-White Ice
CFL 1800A	26-Nov-07	-16.7	24	Grey-White Ice
CASES 400-1	05-Nov-03	-9.9	25	Grey-White Ice
CASES 400-2	05-Nov-03	-9.9	25	Grey-White Ice
CFL 1820	24-Nov-07	-22.7	26	Grey-White Ice
CFL 2007D5	05-Dec-07	-19.7	26	Grey-White Ice
CFL 1812	25-Nov-07	-16.6	31	White Ice
CFL 2007D4	01-Dec-07	-17.9	33	White Ice
CFL 1117	15-Nov-07	-16.0	34	White Ice
CFL 1100	19-Nov-07	-16.2	36	Rubble Ice
CFL 1910	20-Nov-07	-13.5	37	White Ice
CASES 303	13-Nov-03	-18.1	38	White Ice
CFL 405A	18-Nov-07	-19.4	43	White Ice
CFL 405B	19-Nov-07	-18.1	46	White Ice
CFL 2007D9	17-Dec-07	-20.2	50	White Ice
CFL 2007D1	28-Nov-07	-16.8	52	White Ice
CFL 437	21-Nov-07	-16.2	57	White Ice
CFL 2007D6	09-Dec-07	-21.8	69	White Ice

Tab. 3.3: Summary of Ice Station Physical Measurements.

Station ID	T_{si} [°C]	S_b [PSU]	S_{si} [PSU]	Surface Salinity [PSU]	Surface Feature Description
ArcticNet 101A	n/a	n/a	n/a	n/a	windspeed = 1 m/s
ArcticNet 101B	n/a	n/a	n/a	n/a	windspeed = 4 m/s
ArcticNet 109	n/a	n/a	n/a	n/a	windspeed = 8.7 m/s
ArcticNet 308.5	n/a	n/a	n/a	n/a	windspeed = 3.6 m/s
CFL 1000	n/a	n/a	n/a	n/a	none
CASES 200B	-4.6	10.5	27.3	n/a	Frost Flowers (<10%)
CFL 2007D2	-10.5	18.5	n/a	n/a	Compression Ridges
CFL 1800C	-8.7	11.8	18.4	n/a	none
CFL 1200	-8.5	17.9	23.6	n/a	none
CASES 112C	-4.4	5.2	28.7	n/a	Wet Surface
CASES 124C	-3.2	5.9	19.3	n/a	none
CASES 124A	-3.3	6.2	17.6	n/a	none
CFL 1110	-4.6	7.9	n/a	n/a	Slushy
CFL 1800B	-10.7	13.7	21.4	n/a	Frost Flowers (25%)
CASES 119	-4.2	7.2	23.6	n/a	none
CASES 409	-3.4	4.1	18.0	12.3 (Snow)	Snow (2 cm)
CASES 206A	-2.4	3.2	7.8	n/a	Snow (2 cm)
CASES 415	-2.9	3.7	14.1	10.6 (Snow)	Snow (6 cm)
					4 cm dry, 2 cm slushy
CASES 504	-4.8	4.8	10.6	n/a	Consolidated Pancake Rims
CASES 503	-5.2	5.1	n/a	n/a	Similar to CASES 504
CASES 200C	-2.5	5.1	16.8	0.9 (Snow)	Snow (13 cm),
					9 cm dry, 4 cm slush
CASES 505	-3.9	3.5	23.4	n/a	F. Flowers (60%) slushy ice
CASES 206B	-2.9	5.5	26.2	n/a	Snow (3 cm)
CFL 1800A	-11.1	8.4	55.9	62.5	Frost Flowers (>95%)
CASES 400-1	-4.0	3.3	n/a	1.5 (Snow)	Snow (10 cm)
CASES 400-2	-4.0	3.3	n/a	n/a	Snow (10 cm)
CFL 1820	-13.7	6.8	82.8	54.8	Frost Flowers (>95%)
CFL 2007D5	-16.4	8.8	69.2	79.2	Consolidated Pancake Rims
CFL 1812	-12.9	6.9	71.9	56.8	Frost Flowers (>95%)
CFL 2007D4	-13.1	7.2	59.9	21.5	Frost Flowers (>75%)
CFL 1117	-10.0	6.4	46.5	11.7	Snow (2 cm)
CFL 1100	n/a	6.8	n/a	n/a	Rough Random Ridges
CFL 1910	-12.8	8.5	45.9	41.8 (FF),	Frost Flowers
				18.6 (Snow)**	(>95%)
CASES 303	-7.2	4.8	25.6	15.4	Snow (5.5 cm)
CFL 405A	-18.2	6.6	75.8	59.8	Frost Flowers (35%)
CFL 405B	-16.7	6.7	n/a	n/a	Frost Flowers (35%)
CFL 2007D9	-14.4	6.5	31.2	25.9*	Snow (4 cm)
CFL 2007D1	-10.1	8.8	42.0	35.2*	Snow (5 cm)
CFL 437	-17.5	6.8	55.8	35.7	Frost Flowers (10%)
CFL 2007D6	-15.4	8.5	46.9	14.3*	Snow (3.5 cm)

3.3 Results and Discussion

3.3.1 Mean NRCS by Ice Type

We have collected the NRCS over several ice types, which we believe to be a good representation of many of the variations observed during the freeze-up (i.e. a total of 40 scan locations). The co- and cross-polarized NRCS can be used to separate the sea ice into WMO classes, but the classification error is large enough to cause uncertainty. These data are useful for building up a large dataset of radar signatures and associated ice types for future classification algorithm development.

As a first pass attempt to separate sea ice types based upon our measurements, we divided the sea ice based upon its WMO description and secondly upon its surface coverage. We considered frost flower coverage of <10% to be bare ice. Fig. 3.4 presents the average co-polarized and cross-polarized NRCS (σ^0_{VV}, σ^0_{VH}, and σ^0_{HH}) as a function of our classification. We did not include the measurements at CFL 2007D2 due to the unique ridging present, nor did we include CFL 2007D5 because it does not fit into the Grey Ice (Snow) or Grey-White (FF) categories (see Table 3.3). NRCS at 30° are presented such that comparisons can be made within the incidence angle range of conventional satellite-based platforms (e.g. RADARSAT-2).

Measurements of open water (OW) were conducted during a variety of wind speeds (see Table 3.3 for wind speeds). The case of low wind speed provides a baseline for our other measurements. Since the surface was nearly perfectly smooth, the dielectric

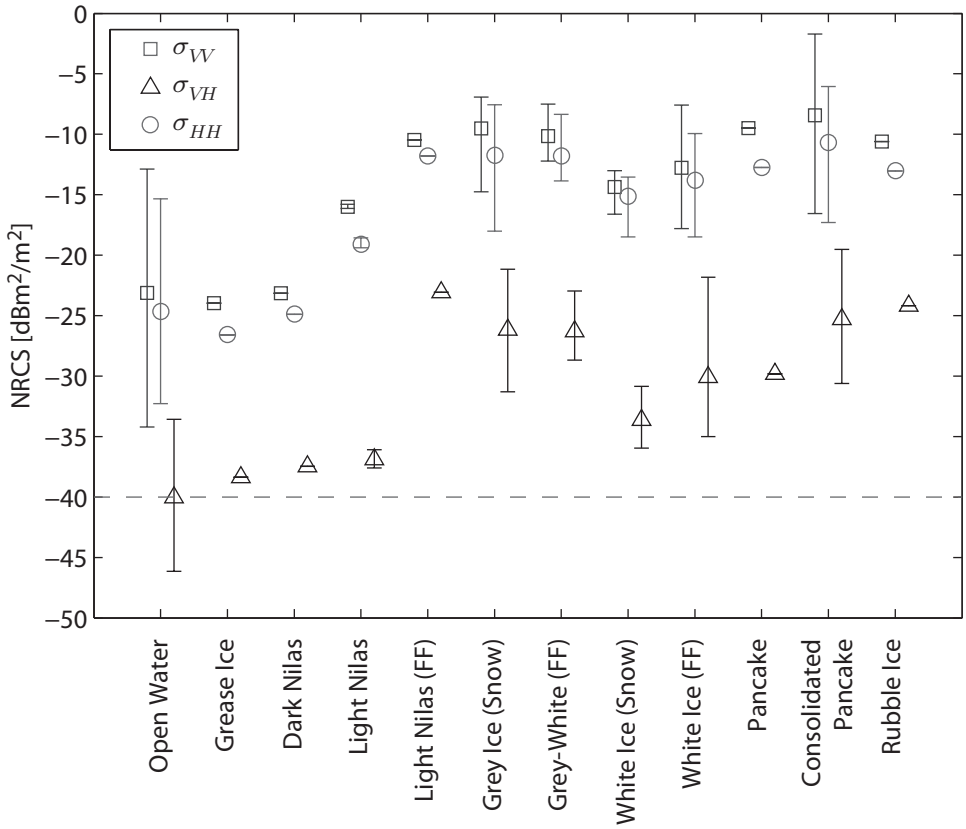

Fig. 3.4: Normalized radar cross section as a function of ice type at an incidence angle of 30°. Error bars represent maximum and minimum values of measurements.

properties of the seawater cause the horizontally polarized waves to be better reflected than the vertically polarized, and as such, the HH signal is slightly higher than that of the VV signal [78]. Other OW measurements were conducted in higher wind speeds, and consequently we observed a large variability in measurements as a function of wind speed. The grease ice measurements show a slight decrease in the co-polarized NRCS when comparing mean values, as expected due to the decrease in the dielectric contrast (more penetration and signal loss) and due to the damping effects on any wave action. However, the grease ice signal could easily be aliased as open water based upon our error bars. In comparison with the field studies of Beaven *et al.* [79], [80], our co-polarized grease ice measurements are quite similar (within about 1 dB), while our the cross-polarized measurements are significantly higher (about 6 dB); however, we acknowledge that our measurements were near the noise floor of the instrument and therefore could play a role in the backscatter differences.

The dark nilas measurements correspond to bare sea ice and produce a marginally higher NRCS than the grease ice and OW (e.g. dark nilas is about 1 dB greater than grease ice likely due to the scattering contribution of the ice-water interface, which exhibits a greater dielectric contrast than gradual contrast presented by the slushy suspension of ice in the grease ice case). Similar to the grease ice case, the dark nilas could easily be aliased as open water based upon our error bars. As the ice continues to thicken to light nilas, the NRCS increases significantly, indicating an increase in the volumetric scattering occurring within the sea ice volume due to an

increase in scatterer size during the desalination process [41]. Additionally, the model study of Fung suggested the surface scattering from the air-ice interface alone could not account for the observed values and the ice-water interface should be included in the analysis [40].

In comparison to the field data of Beaven *et al.* [79], [80], we find that our results are in good agreement. Our measurements of dark nilas for co-polarized signals are on the higher end of their measurements while our cross-polarized signals are near the noise floor and cannot be readily compared. For the light nilas measurements, our VV measurements are again slightly higher on average; however, the HH and VH measurements are within their reported 25^{th} and 75^{th} percentiles. When we compare our thin ice types (light nilas) to the field measurements of Grandell *et al.* [81], we find that our measurements for VV fit within the ellipses that they have drawn for "thin young ice" at 23° incidence angle.

There is a definite distinction between the NRCS for light nilas and light nilas covered with frost flowers, in that the frost flower covered NRCS is approximately 6 dB higher than the bare light nilas for all incidence angles, except at 20°. Onstott suggested that the brine-rich ice crystals cause an increase in surface scattering as they increase surface roughness [39]. On the other hand, Pimsamarn observed the enhancement of backscattering was caused by an increase in volume scattering from the brine-rich slush layer underneath the frost flowers [82]. We did not observe this slush layer in all cases. Based on the work of Onstott and Pimsamarn, we suggest

that the increase of 6 dB can therefore likely be attributed to the enhanced surface scattering caused by the larger surface roughness and high dielectric constant, plus an enhancement of the volumetric scattering occurring within the upper few centimeters of the ice.

The measurements of frost flower covered light nilas, snow covered grey ice, and frost flower covered grey-white ice are quite similar for both co-polarized and cross-polarized signals, making the distinction between ice types using the NRCS rather difficult (Fig. 3.4). In fact, the measurements of frost flower covered white ice are also quite similar when taking into account the range of values shown by the error bars. Although the cross-polarized signals for frost flower covered light nilas have the highest mean values, we do not have enough samples to infer whether or not we can separate this ice type from the others. Further data from frost flower covered light nilas is needed to provide a better sense of the variability in the measurements.

When examining the surface ice salinities for the frost flower covered ice (see Table 3.3), we note that the salinity tends to increase with an increase in thickness for light nilas and grey-white ice (21 PSU to 83 PSU for thicknesses of 9 cm to 26 cm). The frost flower coverage also tends to increase (from 25% to >95%). The trend does not appear to continue with the frost flower covered white ice, however, due to factors such weathering, wind action, and potential snow accumulation, it is not surprising. In his laboratory experiment Nghiem [71] reported an increase in surface salinity as sea ice grew in thickness, with an abrupt doubling to between 50 and 80 PSU. He found

that this corresponded to a frost flower coverage of around 30% and a backscatter minimum [71]. We could not observe this minimum in our field experiments since our data is spatial, not temporal, and therefore we recommend that a field study to observe the timing of this minimum could be useful.

When comparing the mean co-polarized NRCS values of snow covered grey ice and white ice, we observe that the white ice values are lower by 3.4 dB, 4.8 dB, and 7.5 dB for the HH, VV, and VH channels, respectively (Fig. 3.4). It is known that the temperature sensitivity of the brine in the basal layer of the snow and near the snow-ice interface affects the dielectric constant of the layer, and therefore plays a role in the measured backscatter [72]. Since our temperatures are higher by a few degrees (when compared to [72]) and the salinity of brine is a non-linear function of temperature, it is difficult to exactly compare the values; however, the values appear to be reasonable.

For comparison with sea ice types impacted by wind action, we present the results for pancake ice and consolidated pancake. For each of these types the NRCS is quite high relative to the same ice thickness categories. This higher return is commonly attributed to the enhanced surface roughness caused by the rims on the edges of the pancakes [83]. Similar enhancement of NRCS can be seen in rubble ice, which is a very common feature in the fall freeze-up due to sea ice dynamics. In comparison with the field studies of Beaven *et al.* [79], [80], our measurements for pancake ice are significantly higher; however, Onstott *et al.* [83] [Fig. 17. c.], reports backscatter

values as high as about 3 dB for slush covered pancakes, which is actually a closer match the physical description of our sampling location. This discrepancy highlights the high variability that may be seen for even one ice type during the fall freeze-up.

3.3.2 Relation of Ice Thickness to Polarimetric Parameters

As introduced, the retrieval of ice thickness from satellite sensors is a major challenge. Through the use of the co-polarization correlation coefficient (ρ_{hhvv}) we have observed that the growth of sea ice can be divided into two separate thickness regimes. Our *in situ* measurements show that it is not possible to obtain a linear or non-linear regression relationship between ρ_{hhvv} and ice thickness. A first-pass visual inspection of the data for sea ice formed under quiescent conditions demonstrated that there are two regimes linked to the evolution of ice thickness, where ice that was <6 cm thick demonstrated a unique ρ_{hhvv} relative to ice >8 cm thick. We did not have data for the range (6 cm - 8 cm).

We performed a two-sample difference of means t-test based on the co-polarization correlation coefficient at each incidence angle that we measured to see if the mean values could be separated into distinct groups. In this analysis, we included all ice stations, regardless of surface type and formation mechanisms (i.e. included consolidated pancake, pancake, and rubble ice). Ice stations that were <6 cm were placed into group 1 (denoted G1), while ice stations that were >8 cm were placed into group 2 (denoted G2). Results from the difference of means showed that the

means of G1 and G2 are significantly different and therefore come from separate populations. This test was found to be acceptable at the $\alpha = 0.01$ confidence level for incidence angles from 20° to 60°. In Fig. 3.5 we have plotted the mean and standard deviation of the co-polarization correlation coefficient for each scan as a function of incidence angle. We have eliminated three major outliers for the following reasons. CFL Station 2007D2 was 4 cm thick nilas; however, it exhibited an abnormally high surface roughness characteristic that was significantly different from the other stations in G1. CFL Station 1200 was consolidated pancake, which exhibits high rims and variable salinity based upon how the pancakes were formed and consolidated. The other cases of consolidated pancake were already in G2 due to their thickness, and so, we believe that CFL Station 1200 is an outlier since it is only slightly thinner and lies on the threshold of the two groups (at a thickness of 6 cm). The third outlier was CFL Station 1110, which was 8.5 cm thick light nilas; however, it was completely covered with a thick layer of wet slush, meaning that electromagnetically it was quite different from the other ice types in G2.

Based on our analysis, there is a statistically significant change in the co-polarization correlation coefficient that is related to the ice thickness. Confidence in making this equality is supported by a large sample set containing several surface types with spatial and seasonal robustness, including bare sea ice in G2. We note that there is a larger variability within G1 (less than 6 cm thickness) than within G2 (greater than 8 cm thickness). Our dataset for G2 had approximately three times the number of

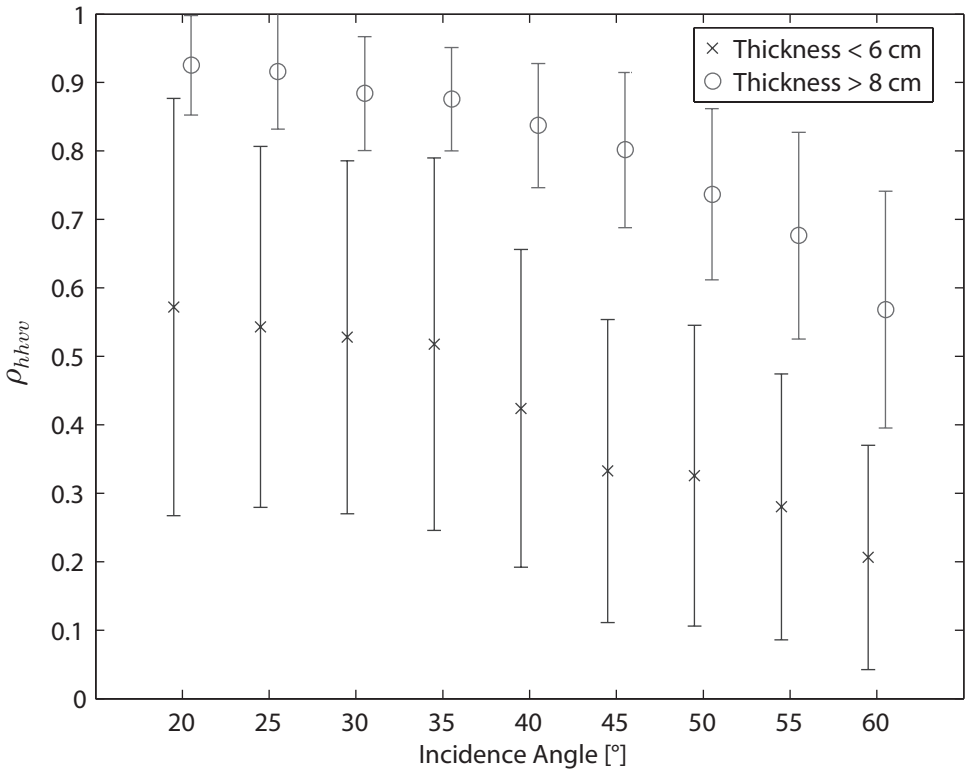

Fig. 3.5: Co-polarization correlation coefficient as a function of incidence angle for ice less than 6 cm and ice greater than 8 cm in thickness. Error bars denote one standard deviation. The data from three stations has been filtered out as discussed in the text.

samples as G1, so it would be interesting to see if the addition of data would reduce the variability. We speculate that there would not be a large reduction since there is a lot of variability in measurements of thin sea ice and open water, and therefore this could be a limitation of using the co-polarization correlation coefficient in sea ice classification. Within G1, the thickness of the ice is small enough that multiple scattering between the ice surface and bottom can cause significant de-correlation ($\rho_{hhvv} < 1$). As a rough estimate for the penetration depth, we can compare with the values reported by Ulaby *et al.* [31], [Appendix E, Fig. E.24]. Using their modeled value for relative dielectric constant of lossy sea ice ($\epsilon_{seaice} = 3.3 - j0.25$ at -10°C and a frequency of 5.5 GHz), we obtain a penetration depth of 12.6 cm, which corresponds to an exploration depth of 6.3 cm. This means that once the thickness reaches greater than 6.3 cm (for the estimated dielectric constant), we do not expect that the sea ice - ocean interface will contribute to backscatter. Within G2, the correlation exists due to the lack of multiple scattering (the ice attenuates enough of the signal to minimize multiple scattering between layer interfaces), and also due to the surface coverage effects. For example, CFL 1800B and CASES 119 have the same ice thickness of 9 cm with very different surface coverage (frost flowers versus bare ice), yet the relation still holds. These results imply that the use of the co-polarization correlation coefficient has the potential for aiding in ice thickness estimation. This is mainly due to the fact that the radar wave has limited penetration depth and further ice growth does not alter the scattering mechanism. Thus, the results suggest the co-polarization

correlation coefficient (ρ_{hhvv}) can be useful to classify thin (<6 cm) and thick (>8 cm) newly-formed sea ice by using satellite sensors (e.g. RADARSAT-2).

Previous modeling studies coupled with measurements by Nghiem *et al.* have produced some results regarding the co-polarized correlation coefficient. For a sea ice sheet of 8.2 cm thickness (which corresponds to our G2), ρ_{hhvv} averages around 0.8 [41]. In another paper, they reported on the same ice sheet when it had reached a thickness of 11.2 cm and the values of ρ_{hhvv} were around 0.82 [84]. Furthermore, their modeling studies showed that the presence of a covering layer (frost flowers 2.5 cm thick) increased the magnitude of ρ_{hhvv}, which is indicative of isotropic scattering characteristics. These laboratory results corroborate our findings. In a different study Nghiem *et al.* found that ρ_{hhvv} ranges from 0.3 to 0.6 for thin lead ice (3.5 cm thick, with incidence angles ranging from 25° to 52°), while for thick first year ice ρ_{hhvv} ranges from about 0.9 down to 0.6 (2 m thick, with incidence angles ranging from 25° to 52°) [85]. It was suggested that the low correlation coefficient for thin ice may be caused by a decorrelation effect of non-spherical scatterers (brine cells) with a preferred orientation relative to the vertical plus some contribution of surface scattering [85]. Since the backscatter from thin sea ice is low at C-band (see Fig. 3.2), the effects of noise can contribute to the de-correlation (i.e. decreases the value of ρ_{hhvv}), so due care must be exercised when evaluating the applicability of the co-polarization correlation coefficient. These past studies have recommended collecting data over a diverse set of ice types and conditions to validate their findings, and so, our data

provides a piece of this missing information.

As a further comparison, a study of polarimetric parameters over soil with various moisture content levels conducted by Mattia *et al.* showed that the magnitude of ρ_{hhvv} was not very sensitive to the surface roughness [86], but further studies by Malhotra *et al.* [87] showed that at higher roughness scales the co-polarized signals are highly correlated. The results of Malhotra *et al.* provide justification for our removal of CFL Station 2007D2 as an outlier. Further modeling studies and the collection of surface roughness data are required to precisely define the interactions of the incident electromagnetic fields with sea ice since we expect, in general, that there will be surface-volume scattering interactions taking place. As a note of geophysical interest for sea ice, the transition from the granular characteristics of the upper frazil layer to the columnar layer occurs near our threshold of 6 - 8 cm. Future studies incorporating detailed sea ice microstructural analysis on a case-to-case basis could help to elucidate any possible connection.

Based upon our results and their statistical significance across all incidence angles that we measured, we recommend that future satellite missions should include products in the form of the co-polarization correlation coefficients. In a fully polarimetric SAR, this parameter is not difficult to calculate and could potentially aid in sea ice type discrimination. There are exceptions to the applicability, as evidenced by our need to filter several outliers to improve upon separation of the two thickness classes; however, observations of the standard backscattering parameters can aid in isolating these

specific cases. Further studies are required to assess the utility of the co-polarization correlation coefficient as an additional parameter for sea ice thickness estimation and type classification.

3.3.3 Frost Flower Effects

Since ship-based field studies do not always provide the luxury of time-series observation in a fixed location, we conducted a case study where we removed snow infiltrated frost flowers from the surface and measured the sensitivity of the radar signature and geophysical parameters to the presence of the old frost flowers. Upon arrival at CFL Station D4, we made our standard *in situ* measurements on the frost flower covered surface. Two varieties of clump-type frost flowers existed on the surface - approximately half of them were 5 cm in height, whereas the others were 3 cm in height. A light dusting of snow (about about 1 cm) existed on and in between the frost flowers. We did not find a slushy layer underneath the frost flowers at all.

At the end of our physical measurements we used plastic shovels and brooms to clear off a large portion of the sea ice surface (a semi-circular region with a radius >18 m). Another set of scatterometer measurements were conducted immediately to quantify the change in backscatter caused by the removal of the frost flowers and snow. 12 hours after the first measurement we conducted a third set of scatterometer measurements and collected the associated ice physical data. It is interesting to note that after only 12 hours the bare ice had increased in thickness by 4 cm, whereas the

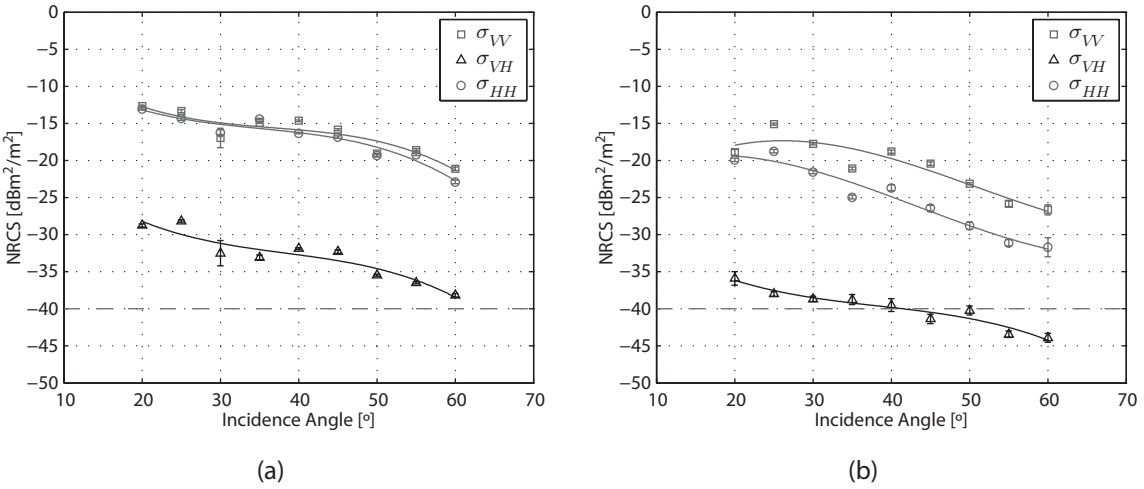

Fig. 3.6: Average radar signatures at Station D4. (a) Before removal of frost flowers, (b) after removal of frost flowers. 3^{rd} order polynomials provided to aid in interpretation of behavior as a function of incidence angle.

ice that was still covered in frost flowers had increased in thickness by only 1 cm. Our measurements are based upon 2-3 thickness observations. These types of measurements can be useful for evaluating the thermodynamic properties of frost flowers.

The results of the scatterometer measurements upon arrival at the station are presented in Fig. 3.6 (a), while the measurements after the removal of the frost flowers are presented in Fig. 3.6 (b). Fig. 3.6 (a) shows the mean and standard deviation of seven scans taken before the removal of the frost flowers, while Fig. 3.6 (b) shows the mean and standard deviation of seven scans taken after the removal of the frost flowers. We have fit a 3^{rd} order polynomial to each of the channels in an attempt to smooth out the effects of taking samples at 5° steps. The noise floor is indicated in Fig. 3.6 by a horizontal dashed line at -40 dB.

Observations of the radar signature before the removal of the frost flowers in

Fig. 3.6 (a) demonstrate that there is minimal separation between the VV and HH channels (with VV always slightly higher). We suggest that in this case there is a complex interaction happening at the frost flower - sea ice interface that would require a modeling study to fully interpret. In the radar signatures of Fig. 3.6 (b), it would appear there is a relatively large separation between the VV and HH channels (with VV always several dB higher); however, there is evidently a more rapid decrease with incidence angle than in Fig. 3.6 (a). Taking an average value of the change in NRCS for each incidence angle, the removal of the frost flower coverage decreases the signal by 4.5, 8.3, and 7.0 dB for σ^0_{VV}, σ^0_{HH}, and σ^0_{VH}, respectively.

The salinities of the snow covered frost flowers and surface scraping presented for CFL Station D4 in Table 3.3 suggest that our measurements have taken place quite late in the lifecycle of the frost flowers, i.e. the salinities are closer to those of basal layer snow than "pure" frost flowers (as compared to the values of Table 3.3. However, we are not observing homogeneous snow covered sea ice, meaning that our measurements help to show the fate of the frost flowers, as has been a point of interest in past studies on frost flower backscattering. For example, the results reported by Nghiem *et al.* [71] state that the bare ice showed a decrease in backscatter of 3-5 dB for all polarizations when compared with the frost flower covered surface, while our results show a decrease of about 4-8 dB for all polarizations. In both cases there is a significant reduction in the backscatter. We attribute the difference between the measured decrease to the differences in the frost flower and ice properties. More specifically, our case study

examined old frost flowers, whereas Nghiem's study examined newly formed frost flowers. Still, our measurements have provided a quantitative measure on the effects of the highly saline snow covered frost flowers, which can be useful in modeling studies and for interpretation of satellite SAR data as the season progresses from the fall freeze-up into the winter.

3.3.4 Variability within a Floe

It is well known that the thermodynamic state of sea ice plays a major role in influencing the interaction of the radar wave with the sea ice and associated sea ice surface features. The thermodynamic state of the ice is also subject to small-scale spatial variability. We conducted a series of radar and physical measurements to quantify the variability within a vast frost flower covered ice floe. We now present the highlights of the dataset from the physical sampling at CFL Station 437, during which we had the opportunity to conduct scans at seven different locations (denoted EM1 - EM7).

We arrived at CFL Station 437, a vast ice floe which was homogeneously covered in frost flowers, at approximately 10 PM local time, on November 21, 2007. Radar measurements were made at three separate locations (EM1, EM2, and EM3). Geophysical measurements were conducted at EM3. Approximately eight hours later we began another series of radar measurements at four separate locations, denoted as EM4, EM5, EM6, and EM7. Geophysical measurements were made at EM5, EM6,

and EM7.

The results of the physical sampling are presented in Table 3.4. Air temperatures refer to the AVOS temperatures measured on the CCGS *Amundsen* at the time of the radar measurements. Salinity measurements are each based upon five replicate samples at the location, and the error represents one standard deviation. For comparison, Martin *et al.* report surface (slush) salinity values on the order of 66 PSU and frost flower salinities of 55 PSU after 73 hours of growth in their 20°C experiment [27]. Our values are lower since the snow has likely wicked up some of the brine and therefore there is a larger volume in which the brine is distributed, while at the same time, our surface salinities are within 6 PSU of the values measured by Martin *et al.* [27].

Tab. 3.4: Physical Properties at CFL Station 437

	$T_{air,AVOS}$ [°C]	$T_{air,insitu}$ [°C]	T_{sa} [°C]	T_{si} [°C]	S_{ff} [PSU]	S_{snow} [PSU]	S_{si} [PSU]
EM1	-16.2	n/a	n/a	n/a	n/a	n/a	n/a
EM2	-16.0	n/a	n/a	n/a	n/a	n/a	n/a
EM3	-15.8	-17.97	-18.47	-17.15	32.71±5.00	34.76±1.89	54.31±3.69
EM4	-20.7	n/a	n/a	n/a	n/a	n/a	n/a
EM5	-20.6	-21.23	-20.48	-17.46	37.92±10.95	38.19±1.07	57.54±6.44
EM6	-20.9	-21.43	-20.85	-17.75	32.94±5.13	35.52±2.62	53.96±2.33
EM7	-20.8	n/a	n/a	n/a	39.30±2.89	39.36±1.11	60.66±3.92

The surface conditions of the ice exhibited an average frost flower height of 3 cm, with some light snow (<1 cm) covering the entire surface. The image showing typical white ice with frost flowers in Fig. 3.2 compares very well with what the ice and frost flowers looked like at CFL Station 437. The average percentage coverage of frost flowers was approximately 9.5%, with an average diameter of 5.8 cm, as obtained

through field measurements and evaluations using ImageJ ©. Our measurements of the sea ice indicated an average thickness of 57 cm, and the salinity analysis exhibited the standard C-shape salinity profile. Micro-structural analysis from a parallel ice physics study (not shown here) indicated that the ice initially formed under calm conditions. The granular layer was approximately 5 cm thick, followed by a transition layer that was 2 cm thick. The next 12 cm were columnar; however, at further depths there was evidence of turbulent mixing processes since there were a variety of different layers with various thicknesses, alternating between granular, mixed, and columnar ice types.

There is a temperature difference of approximately 5°C between the first group of measurements (EM1 - EM3) and the second group of measurements (EM4 - EM7). This suggests that there may not be only spatial variability but also temporal variability associated with temperature difference. The radar NRCS values from all measurements exhibited high variability (not shown here to retain clarity in Fig. 3.7). Most of the variability existed between two groups of measurement (i.e., group 1 for EM1-EM3 and group 2 for EM4-EM7) Fig. 3.7. Applying a Wilcoxon Signed Ranks test yields the result that the two groups of measurements have significantly different median values, acceptable at the $\alpha = 0.05$ confidence level for all incidence angles except 20° for σ^0_{VV} and σ^0_{VH}. For σ^0_{HH} the test results suggest that the groups are different at mid-to-far range incidence angles ($\geq 40°$) except at 50° (p-value = 0.086). The non-parametric Wilcoxon test was chosen here due to low number of samples and the

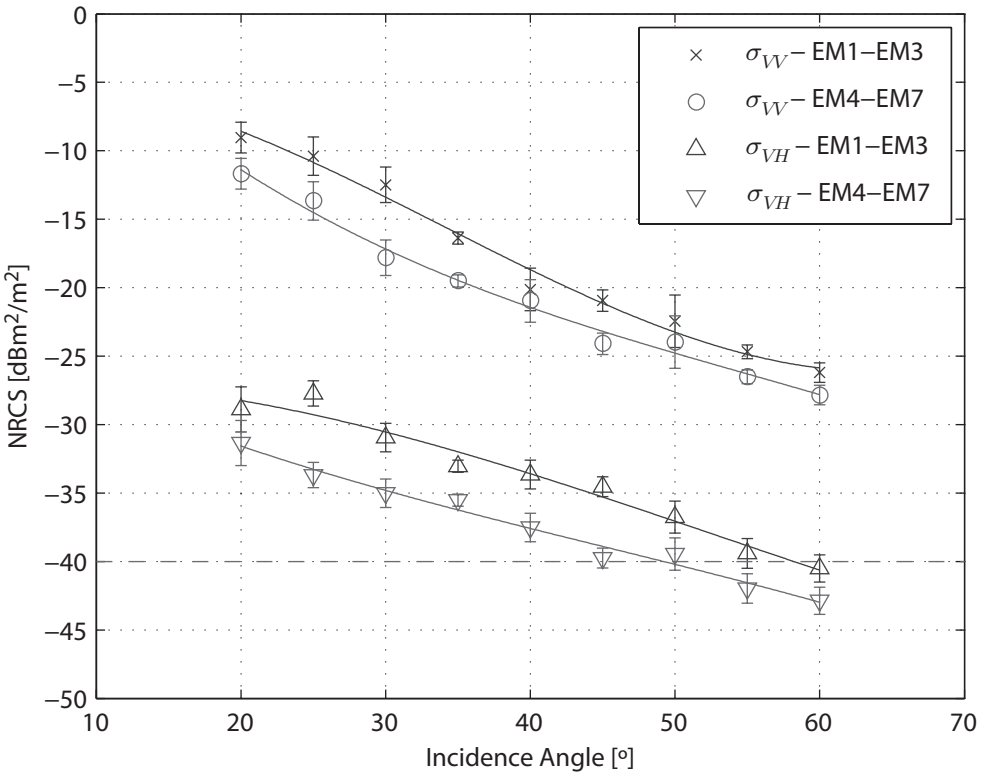

Fig. 3.7: Radar signatures for Station 437 separated into thermal regimes. Error bars represent one standard deviation based on n = 9 and n = 11 samples for EM1-EM3 and EM4-EM7 respectively. 3^{rd} order polynomials provided to aid in interpretation of behavior as a function of incidence angle.

failure of data at some incidence angles to follow the normal distribution assumption required for the parametric difference of means t-test.

Our result suggests that in this case study the effects of spatial variability within the given ice floe were smaller than that of the temperature; however, the variations could not be explained by temperature alone. Similar effects in the change of temperature were also observed in passive microwave signatures [88]. This can be attributed to the observed salinity variations within the floe, such that even slight increases in

temperature should increase the spatial variation of the complex dielectric constant significantly.

While it is tempting to relate the change in temperature with the change in backscatter values, it would be naïve to ignore the effect of the frost flowers. The frost flowers were high salinity clumps that have an effective radius on the order of half of a wavelength at C-band. These features would influence changes in scattering predominantly in the near-range, where the radar is most sensitive to surface roughness effects, and may explain the failure of the Wilcoxon difference test at 20°. Future modeling endeavors must somehow account for the frost flowers, for example, considering modifications to the method of Twersky for scattering bosses on a conducting plane [78]. The situation is quite complex, and so we suggest that future work to uncover the details of the scattering mechanisms of mixed surface types (i.e. saline snow and frost flowers) should be considered in controlled laboratory studies. In this manner the effects of the temperature could be isolated.

3.4 Chapter Conclusions and Discussion

In this chapter, data were presented showing the average NRCS by ice type, including variations in surface coverage. Our results show that there is a large variation of scattering characteristics dependent upon the ice type and surface coverage. A statistical study of the co-polarization correlation coefficient (ρ_{hhvv}) showed that we could use the co-polarization correlation coefficient to separate measurements into two

separate regimes: ice that is less than 6 cm thick, and ice that is greater than 8 cm thick. This polarimetric parameter was shown to be sensitive to both ice thickness and surface characteristics (both the type of coverage and the relative roughness).

The effect of snow covered frost flowers on the NRCS were shown to have a major impact on the backscattered power and the radar signature. We quantified the decrease in the NRCS due to the removal of snow covered frost flowers as 4.5, 8.3, and 7.0 dB for σ^0_{VV}, σ^0_{HH}, and σ^0_{VH}, respectively, which gives an average value of 6.6 dB.

Measurements of the NRCS over a uniform floe of new first year sea ice were shown to be sensitive to a $5°C$ temperature drop (which corresponded to a reduction of NRCS by more than 5 dB for all incidence angles). Our spatial-temporal analysis showed that these results are statistically significant and that the temperature variation over a uniform ice floe plays a role in the measured backscatter.

As stated in our introduction, our fieldwork was conducted to collect geophysical and polarimetric scatterometer data over a large variety of sea ice types and surface coverage, and to study how the variations in the thermodynamic and physical state of sea ice are related to the scatterometer signatures and polarimetric parameters. With these objectives complete, and the modeling data collected, our next few chapters outline components of the modeling techniques and modeling study.

4. NUMERICAL TECHNIQUES FOR SCATTERING FROM OBJECTS IN MULTI-LAYERED MEDIA

In this chapter, we present techniques for simulating scattering problems involving multi-layered media using an FDTD-FVTD method. We begin by presenting some motivation and previous work on techniques that have been used to simulate or model multi-layered media. A scattered-field formulation that is well-suited to the remote sensing problem is presented. We then discuss how the technique can be implemented in a time-domain numerical engine – the FVTD engine. To demonstrate and validate the method, we first show some simple results for reflection and transmission from multi-layered media, followed by a comparison of our results to some examples of buried canonically-shaped objects that have been discussed in the open literature.

Scattering models for remote sensing typically consist of a stratification of the geophysical media into a number of layers that are representative of the physical make-up of the region where the remote sensing experiments took place. Since from a physical standpoint we can consider a representative 1D-profile of the medium, layers are usually oriented perpendicular to the z-axis, as shown in Fig. 4.1.

The number of layers that are needed in the model are often dictated by the

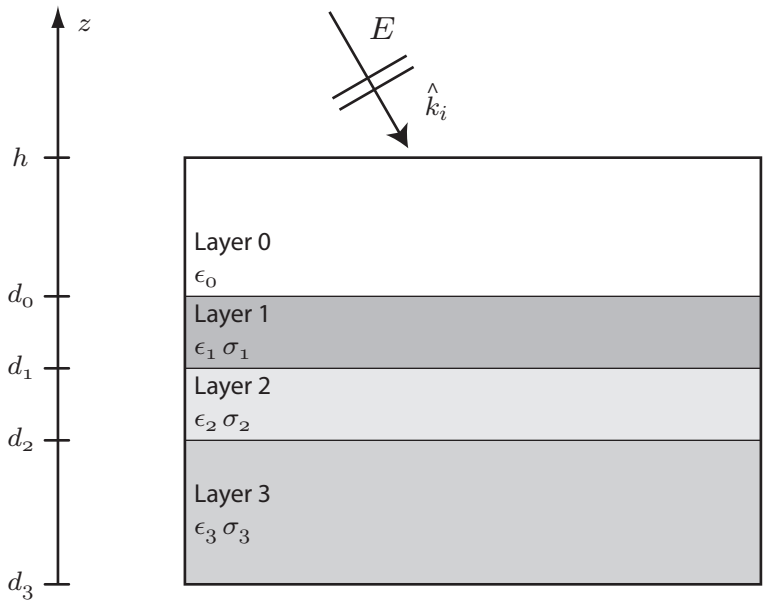

Fig. 4.1: Geometry of a multi-layered medium with stratification perpendicular to the z-axis.

physical make-up of medium. For example, a two-layer model can be used when we are interested in modeling first-year sea ice, where the upper layer would be air, and the lower layer would be sea ice. A three-layer model would be appropriate when we are modeling snow-covered sea ice. Many different types of scattering models are available in the literature (see the discussion and references in Chapter 2 for more details).

One of our main objectives was to develop an appropriate numerical technique or method for simulating the scattering from sea ice. As a starting point, we considered commercially available software packages that had the potential to numerically solve the sea ice scattering problem, in addition to studying the AWT and RT formulations presented in Chapter 2, Section 2.3. For example, we attempted to use a program

that solved the electric field integral equation using the method of moments, but it was not capable of modeling dielectric objects in layered media. We also attempted to use a program based on the finite element method (FEM), but it lacked the capability of a plane wave source that accounts for multiple layers, which was necessary for our model. We then explored techniques that used the well-known FDTD method, due to its prevalence in the literature, and since Nassar had successfully used it to model sea ice scattering [47]. Again, we found that using commercially available software did not provide us with the flexibility that was needed for implementation of the remote sensing simulation. As in the case of the FEM program, the formulations of existing FDTD solvers did not permit us to have an incident field for layered media. Without an incident field that accounts for the layers, the model would consist of a layered object floating in a free-space background, which is physically incorrect.

At this point, it was clear that a customizable code was required to provide the simulation tool we wanted. A fully-parallelized FVTD computational engine was in development in our Computational Electromagnetics Group, and so, collaboration and expertise in the development was available. The FVTD method has the potential to deal with some of the short-comings of the FDTD method (as described later in this chapter). To our knowledge, in spite of its potential benefits, the FVTD method had not been reported for simulating electromagnetic scattering from sea ice. This is likely since FVTD solvers for electromagnetics are not commonly available and custom code must be developed. Furthermore, the use of a time-domain method would

provide the desirable capability of obtaining scattering results at multiple frequencies simultaneously. We would like to eventually examine the frequency dependence of sea ice scattering using a modeling tool, since the requirement of separate instruments for measurements at a large number of frequencies is not practical in our ship-based research. While it is feasible to consider investing time and development efforts into developing a frequency domain method with similar capabilities, we have chosen to explore the use of the FVTD method in this thesis.

Before continuing to discuss the details of the methods, we outline our modeling steps for calculating scattering in multi-layered media:

1. Visualize the geometry of the complete problem that we are trying to model, which includes multiple layers and any number of inhomogeneities.

2. Decompose the problem into two separate problems, a FDTD total-field simulation for the layered media, and a FVTD scattered-field simulation which will incorporate the inhomogeneities.

3. Calculate the total-field 1D-FDTD solution to the propagation of a plane-wave through the multi-layered media (without any inhomogeneities present), and which contains information on the reflection and transmission of the wave at the interfaces.

4. Use the result of the 1D-FDTD solution for layered media as the source for the scattered-field formulation of the FVTD method and calculate the scattering

from the inhomogeneities that are present in the layered media. Scattered-fields are only generated at the inhomogeneities and they are easily absorbed by the boundary condition on the FVTD computational domain.

Material in this chapter has been accepted for publication in the IEEE Transactions on Antennas and Propagation [89][1].

4.1 A Scattered-Field Formulation for Scattering from Objects in Multi-layered Media

The study of electromagnetic wave scattering from objects in multi-layered media is a widespread problem with diverse applications including remote sensing of earth environments [90] and buried object detection [91], [59]. In contrast to the problem where the target or object of interest lies in free-space, the formulation and subsequent analysis of the multi-layered media are complicated due to the layer interfaces that govern the propagation of the interrogating incident-field. Determining a simple way to account for the layers is a non-trivial task, which has led to a variety of techniques in the literature for modeling subsurface problems [92] (and references therein), [93]. As stated in [60], a variety of analytic methods have been developed and are capable of describing the propagation through multi-layered media; however, it is challenging to utilize these methods in an existing numerical solver.

[1] © 2011 IEEE. Reprinted, with permission, from D. Isleifson, I. Jeffrey, L. Shafai, J. LoVetri, and D. G. Barber, "An Efficient Scattered-field Formulation for Objects in Layered Media using the FVTD method," *IEEE Trans. Antennas Propag.*, AP1010-1176.R1, 2011.

Differential-equation-based techniques are particularly well suited for modeling wave interactions with inhomogeneities in a multi-layered medium since the incorporation of an inhomogeneity does not increase the number of unknowns that must be solved [60]. The ubiquitous FDTD method [54] has been used in this respect, and while it is appropriate for many geometries, it is deficient in that it requires a high level of discretization in order to resolve objects with curved features. In many subsurface scattering problems, the inhomogeneities exhibit curved features (e.g. brine inclusions in sea ice, landmines, cancerous tumors), and so, a method that takes the curved features into account would be useful. One such method is the FVTD method (see Bonnet *et al.* [56], and Firsov *et al.* [57], which is particularly well-suited to modeling curved features due to its ability to use a conforming irregular grid. With appropriate interpolation methods, the solutions for the multi-layered problem that have been developed for the FDTD method can be used with the FVTD method.

When using a scattered-field technique to perform calculations, knowledge of the incident field at the inhomogeneity for the entire time history of the simulation is required. When the medium is multi-layered, the incident field at the inhomogeneity is the resultant of various reflections from and transmissions across the layer interfaces. The scattered-fields generated by the inhomogeneity then propagate in the multi-layered medium and are absorbed at the boundaries. In time-domain differential-equation-based methods the boundary conditions are more efficient at absorbing normally incident scattered fields, and so, incorporation of the incident-field into

the numerical method and solving for only the scattered-field allows the boundary condition to be more effective.

A method for generating a total-field/scattered-field (TF/SF) source for general layered media was presented in [94]. Continued interest in developing the technique is evident in the variations that have been presented in the literature (for example, [95], [96]). Previously, [60] presented an FDTD method for modeling scatterers in stratified media, but they limited their study to time-harmonic plane-waves. In this work, we adapt the general TF/SF source for use in a scattered-field formulation of the FVTD method and show how it can be used for scattering from objects within a multi-layered medium. The focus of [94] is mostly on computational aspects such as stability, dispersion, and evanescent waves; their examples are strictly multi-layered media without any inhomogeneities. In contrast, our work focuses on the utilization of the method for providing an incident-field and calculating the scattering from inhomogeneities lying within the medium. Furthermore, our work considers an interpolation scheme that permits an irregular mesh, such as that utilized in the FVTD calculation. To validate our method, we compare with other published data for canonical shapes lying within a half-space medium and below a lossy layer. Incorporation of the scattered-field formulation for multi-layered media in the FVTD engine provides a new tool for modeling complex layered media and has future potential to be used for modeling electromagnetic interactions in remote sensing studies.

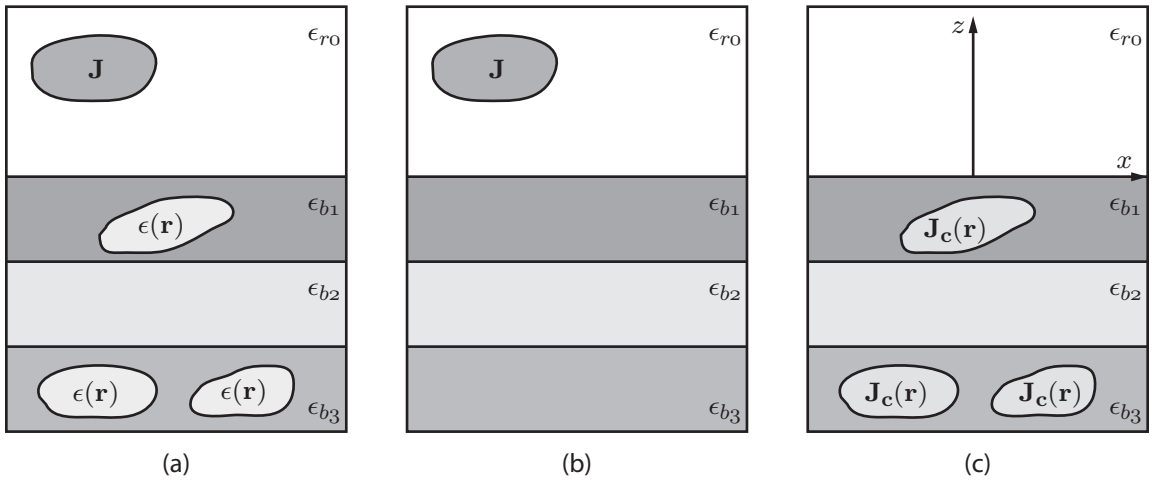

Fig. 4.2: Hypothetical geometry illustrating the decomposition of the fields in the scattered-field formulation. a) Total-field geometry with the source, $\mathbf{J}$, in the presence of multiple layers and inclusions ($\epsilon(\mathbf{r})$), each with possibly different dielectric constants, b) incident-field geometry with only the layers and the source, and c) scattered-field geometry where the contrast sources ($\mathbf{J}_c(\mathbf{r})$) radiate in the presence of the multi-layered background medium.

4.2 Formulation

In this section we formulate the total-field/scattered-field (TF/SF) background theory. Details of the practical application of this general concept in an FVTD numerical solver are given. We present numerical results for several canonical shapes for validation.

Let us denote the time-domain electric field intensity as $\mathbf{E}(\mathbf{r}, t)$, the time-domain magnetic field intensity as $\mathbf{H}(\mathbf{r}, t)$, the relative permittivity as $\epsilon(\mathbf{r})$, the relative permeability as $\mu(\mathbf{r})$, and the impressed time-domain electric current as $\mathbf{J}(\mathbf{r}, t)$. Using

the standard incident-field/scattered-field decomposition we have

$$\mathbf{E}(\mathbf{r},t) \triangleq \mathbf{E}^{inc}(\mathbf{r},t) + \mathbf{E}^{sc}(\mathbf{r},t), \tag{4.1}$$

$$\mathbf{H}(\mathbf{r},t) \triangleq \mathbf{H}^{inc}(\mathbf{r},t) + \mathbf{H}^{sc}(\mathbf{r},t), \tag{4.2}$$

where the incident fields are defined to exist in a background media, with $\epsilon_b(r)$ and $\mu_b(r)$, and are produced by the impressed current $\mathbf{J}(\mathbf{r},t)$. That is,

$$\nabla \times \mathbf{E}^{inc}(\mathbf{r},t) = -\mu_b(\mathbf{r})\frac{\partial \mathbf{H}^{inc}(\mathbf{r},t)}{\partial t} \tag{4.3}$$

$$\nabla \times \mathbf{H}^{inc}(\mathbf{r},t) = \epsilon_b(\mathbf{r})\frac{\partial \mathbf{E}^{inc}(\mathbf{r},t)}{\partial t} + \mathbf{J}(\mathbf{r},t). \tag{4.4}$$

The scattered field is then produced by the difference between the true media, $\epsilon(\mathbf{r})$ and $\mu(\mathbf{r})$, and the background. After some algebraic manipulation,

$$\nabla \times \mathbf{E}^{sc}(\mathbf{r},t) = -\mu(\mathbf{r})\frac{\partial \mathbf{H}^{sc}(\mathbf{r},t)}{\partial t} - \mathbf{M}_c(\mathbf{r},t) \tag{4.5}$$

$$\nabla \times \mathbf{H}^{sc}(\mathbf{r},t) = \epsilon(\mathbf{r})\frac{\partial \mathbf{E}^{sc}(\mathbf{r},t)}{\partial t} + \mathbf{J}_c(\mathbf{r},t), \tag{4.6}$$

where the contrast magnetic and electric contrast sources are defined as

$$\mathbf{M}_c(\mathbf{r},t) = [\mu(\mathbf{r}) - \mu_b(\mathbf{r})]\frac{\partial \mathbf{H}^{inc}(\mathbf{r},t)}{\partial t} \tag{4.7}$$

$$\mathbf{J}_c(\mathbf{r},t) = [\epsilon(\mathbf{r}) - \epsilon_b(\mathbf{r})]\frac{\partial \mathbf{E}^{inc}(\mathbf{r},t)}{\partial t}. \tag{4.8}$$

For non-magnetic media, $\mathbf{M}_c(\mathbf{r}, t) = 0$. If we take the incident-field to propagate in the layered background medium, then it is clear from (4.8) that the scattered-field is generated by equivalent sources at the inhomogeneities. The fact that the sources for the scattered-field occur only at the inhomogeneities means that the field impinging on the boundaries is more easily absorbed by whatever absorbing boundary condition is being used. The incident-field still contains all the information on the interactions of the waves as they propagate from one layer to another and scatter from the layer interfaces. One of the benefits of using the TF/SF formulation is that the incident-field can be specified either analytically or numerically.

4.3 Numerical Implementation

In order to demonstrate the utility of the TF/SF formulation as a general concept, we apply the method into the framework of an existing FVTD numerical solver. This is similar to the approach used in [60], where a time-harmonic plane-wave source was applied to a scatterer in a finely-stratified layered medium. In our work, we use the finite-volume time-domain (FVTD) method to time-evolve the scattered-field given a numerically computed (as opposed to analytically defined) incident-field source term. A technique similar to the one presented here can be used with any time-domain field solver.

4.3.1 FVTD Computations

The FVTD method is a robust and flexible scheme for numerically simulating three-dimensional electromagnetic problems [56], [57]. It is an $O(N)$ solver, which means that it scales linearly with the number of elements in the mesh. One of the advantages FVTD has over the FDTD algorithm is that both structured and arbitrary unstructured meshes are equally suitable discretizations for FVTD simulations. This implies that the volumetric mesh can be created to naturally follow oblique surfaces and no alteration to the algorithm is required to compensate for an inaccurate physical model.

The FVTD formulation used for the numerical simulations produced in this work is a cell-centered, upwind, characteristic-based numerical engine for meshes consisting of first-order polyhedral elements [57]. It is second-order accurate in both time and space. The engine is capable of solving Maxwell's equations in the time-domain using either a total- or scattered-field formulation, the latter permitting arbitrary (i.e. non-homogeneous) background media. The numerical implementation has been parallelized for distributed parallel environments by decomposing the computational domain into subdomains using orthogonal-recursive bisection (ORB). Each subdomain is assigned to a unique processor and the underlying system of partial differential equations is solved locally on each processor by introducing a halo/ghost duplication of elements lying on the boundary of a processor's domain [57].

The upwind formulation explicitly imposes the electromagnetic boundary conditions at the facets of each mesh element. Not only does this achieve accurate modeling

of irregularly shaped inhomogeneous objects, but also allows for very simple, but effective absorbing boundary conditions (ABC) at the edges of the computational domain without having to introduce perfectly matched layers (PML). These ABCs are known as the Silver-Müller conditions. PML absorbing boundary conditions have also been implemented [97], although we have not implemented them in our FVTD engine. Due to its advantages, FVTD is an excellent candidate for solving field problems with a large number of small inhomogeneities.

4.3.2 The Plane-Wave Injector

When simulating multi-layered media, truncating a plane-wave in a total-field formulation is very inefficient because the incident-wave vector is impinging normally (or close to normally) to the ABC. This is the worst possible case for the ABC to absorb the wave. Additionally, spurious reflections occur where the layer interfaces meet the boundary conditions, corrupting the desired scattered-fields from objects within the layered medium. In effect, it is impossible to distinguish between scattered-fields from the objects and erroneous scattered-fields from the ABC.

One way to mitigate this problem is through the use of the scattered-field (SF) formulation. A total-field simulation can be performed to obtain the total-fields for a wave propagating in layered media. We then use this total-field as the incident-field in a scattered-field formulation. A hypothetical SF decomposition is shown in Fig. 4.2 for the case of multi-layered media. Following [94], we utilize a 1D-FDTD solution for a

wave propagating through layered media at arbitrary incidence angle, with appropriate modifications for the FVTD method. For completeness, the derived expressions for TE and TM wave propagation are summarized here.

The TE equations for plane wave propagation through multi-layered media are given as:

$$\begin{aligned} \frac{\partial E_y}{\partial z} &= \mu_0 \frac{\partial H_x}{\partial t}, \\ \frac{\partial H_x}{\partial z} &= \epsilon_0(\epsilon_r - \epsilon_{r0} sin^2\theta)\frac{\partial E_y}{\partial t}, \\ H_z &= Y_0\sqrt{\epsilon_{r0}} sin\theta E_y, \end{aligned} \tag{4.9}$$

where θ is the incidence angle measured between the direction of propagation and the z-axis, $Y_0 = \sqrt{\epsilon_0/\mu_0}$ is the intrinsic admittance of free space, and ϵ_{r0} is the dielectric constant of the uppermost (or 0^{th}) layer.

Similarly, the TM equations are given as:

$$\begin{aligned} \frac{\partial E_x}{\partial z} &= -\mu_0 \frac{\partial H_y}{\partial t}\frac{(\epsilon_r - \epsilon_{r0} sin^2\theta)}{\epsilon_r}, \\ \frac{\partial H_y}{\partial z} &= -\epsilon_0\epsilon_r \frac{\partial E_x}{\partial t}, \\ E_z &= \frac{Z_0\sqrt{\epsilon_{r0}} sin\theta}{\epsilon_r} E_y, \end{aligned} \tag{4.10}$$

where $Z_0 = \sqrt{\mu_0/\epsilon_0}$ is the intrinsic impedance of free space.

These equations resemble the familiar transmission line equations and with ap-

propriate descriptions of the dielectric profile in the z-direction, they describe the propagation of a plane-wave through layered media. In order to include lossy material, a variation to the TM equations must be made (not demonstrated in this paper, but described in [94]). To solve the TE or TM equations, we discretize the equations, following the approach of [55], where the electric and magnetic field components are interleaved, and we use a central-difference approximation. We set the temporal discretization to obey the Courant stability criterion, $\Delta t \leq \Delta z/v_0$, where v_0 is the velocity of propagation in the layer with the lowest dielectric constant. We apply a basic PML boundary condition at the upper and lower bounds of the 1D-solution grid, but also pad the solution domain to minimize the error created by the boundary (i.e. add more distance for the wave to travel than is necessary for the FVTD solution). This has no impact on the memory required to store the 1D-solution since we only keep the portion which will correspond to the variation required within the FVTD domain, but it does remove artificial reflections created from the boundaries in the 1D-solution.

In practice, the 1D-solution is interpolated into the 3D irregular mesh that is used in the FVTD computations. A principle plane containing the time history of the plane wave propagation through layered media is made to coincide with the xz-plane. To find the field values along this principle plane, we need only a time shift, as this is a property of plane wave propagation. This concept is illustrated in Fig. 4.3, where the principle plane is shown to coincide with the xz-plane, and $\tau = x_1 sin(\theta)/c_0$ (c_0 is

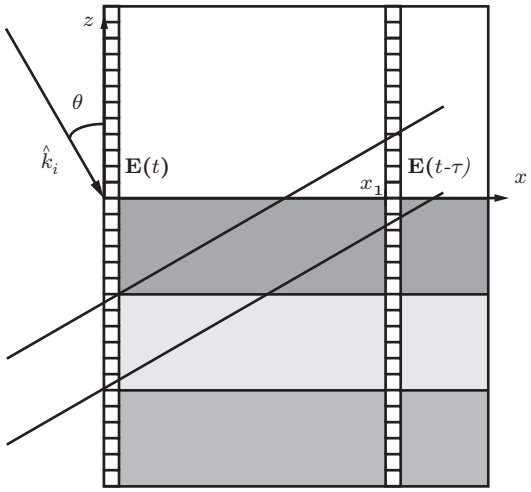

Fig. 4.3: Calculation of field values on the principle plane using the time-delay factor, τ. The field calculated at x_1 are the fields calculated along the z-axis with an appropriate time-delay.

speed of light in a vacuum). The solution for wave propagation along the negative z-axis is calculated and the time-delayed result is utilized to find the field value at a location x_1. To obtain a 3D representation, we utilize the invariance of the solution along the other coordinate axis (y-axis).

4.3.3 Interpolation of the 1D-FDTD Solution to FVTD Grid

Many practical implementation issues exist, such as choosing an appropriate interpolation method and ensuring that the spatial discretization of the auxiliary 1D-FDTD simulation does not cause dispersion in the main FVTD simulation. If the FVTD grid were regular (as would be used in a 3D-FDTD grid), we could follow the method of [94] and increase the spatial sampling by an odd factor and thereby ensure that the interfaces were preserved. Moreover, since the auxiliary FDTD simulation takes

a small fraction of the time needed for the overall FVTD scattering simulation, we choose the spatial discretization to be much smaller than that of the overall FVTD mesh. Cubic spline spatial interpolations and nearest-neighbor temporal interpolations are performed to find the corresponding field values in the centroids of the $3D$ elements (tetrahedrons) that make up the FVTD mesh.

The results of the incident-field propagation are calculated and stored in arrays in memory. They are potentially accessed only during the update scheme of the FVTD simulations, which checks to see if the contrast between the background mesh (that which is seen by the incident field) and the scattered field mesh are non-zero. When they are non-zero, this indicates the presence of a contrast source (i.e. $\mathbf{J}_c(\mathbf{r}, t) \neq 0$) and a scattered-field is generated at that particular mesh element. This means that results of the incident-field interpolations are only used when needed and they are not calculated and stored throughout the entire mesh, which would be inefficient.

4.4 Numerical Results and Discussion

In this section we calculate the scattered near-field values for a variety of objects located within a planarly-layered medium. Canonical examples are chosen such that comparisons can be made with other published data in the literature. We have found that there is a dearth of examples that compute and provide graphical results for the near-field scattering from objects within multi-layered media, in spite of the fact that this problem is conceptually well-known. In particular, we provide comparisons with

the work in [93] (who provides a method based on the Born approximation) and [98] (who introduced a method based on the method of moments).

The computational geometry was created using a freeware mesh-generating program, GMSH [99], which was also used to transform the physical description into a mesh for FVTD computations. The time function of the input waveform for all scattering simulations was a Gaussian derivative:

$$f(t) = \frac{2A(t-t_0)}{b^2} exp(-(t-t_0)^2/b^2), \tag{4.11}$$

where $A = 1$, $t_0 = 0.2$ ns, and $b = 70$ ps. The constants in equation (4.11) were chosen such that sufficient energy would propagate at the frequency of interest (specifically, 6 GHz).

A plot of the input time function in the time and frequency domain are given in Fig. 4.4. From the graph, we see that there is energy available across a broad spectrum of frequencies. This input time function is used throughout this thesis, with the exception of the propagation example presented in Section 4.4.1.

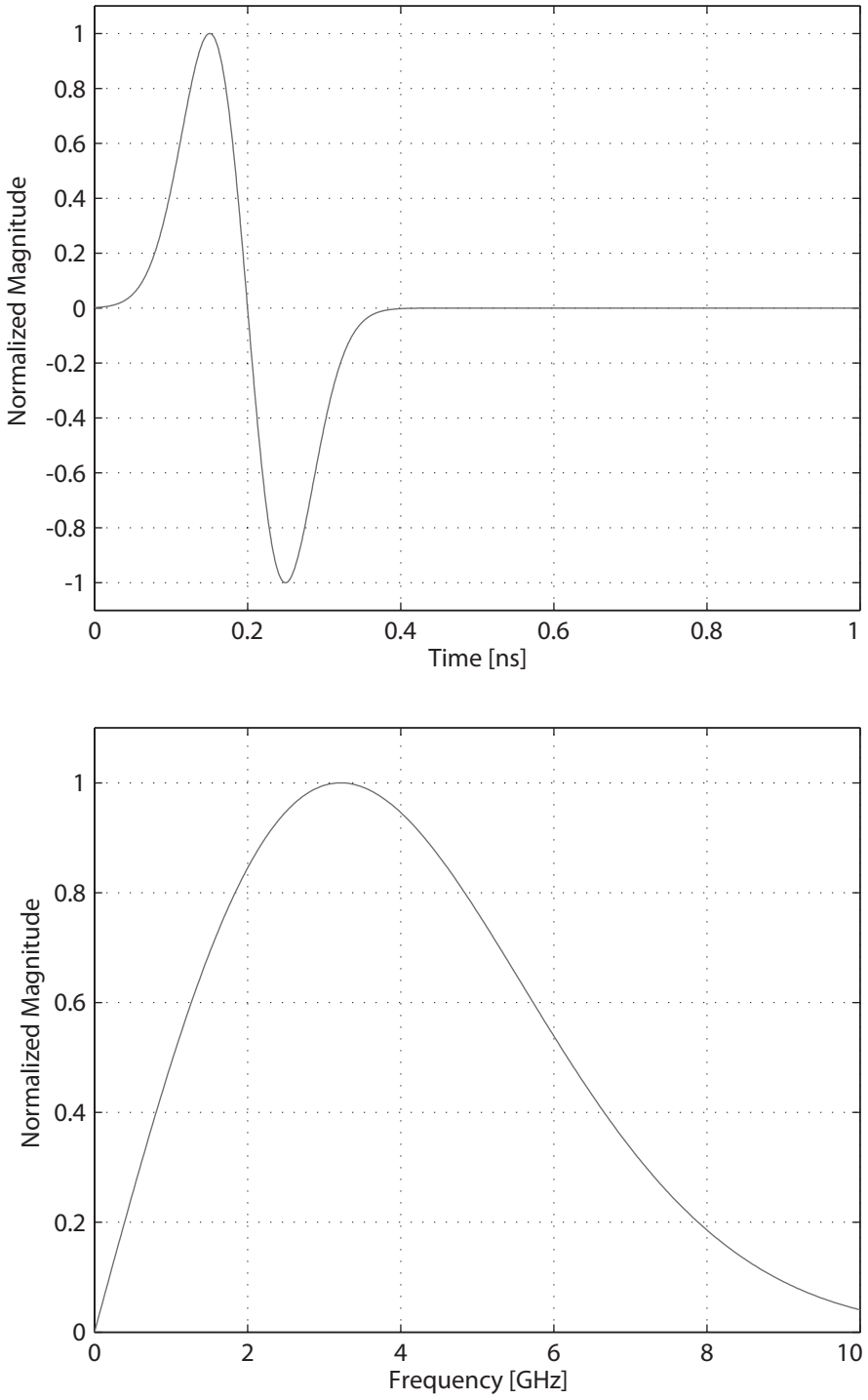

Fig. 4.4: The input time function (a Gaussian derivative) in time-domain (upper figure) and transformed into the frequency domain (lower figure).

4.4.1 Propagation in a Multi-layered Medium

To begin, we present the propagation of a time-domain plane-wave through a multi-layered medium. In this case, we do not have any objects that will cause scattering, so the reflections are caused only by layer interfaces within the computational domain. The time function of the input waveform for this example is a Gaussian pulse:

$$f(t) = A\, exp(-(t - t_0)^2/b^2), \tag{4.12}$$

where $A = 1$, $t_0 = 0.15$ ns, and $b = 50$ ps. A Gaussian pulse was chosen since it is easier to see the characteristics of the pulse (versus a Gaussian derivative) as it travels through the medium.

The first case considered is a dielectric half-space. The geometry of the half-space problem is imposed on Fig. 4.5. The x-dimension is 0.12 [m], the y-dimension is 0.015 [m], and the z-dimension is 0.12 [m] in total. We placed several observation points parallel to the z-axis in order to provide a time-domain plot of the propagation of the wave through the computational domain. We demonstrate the propagation of the wave through the computational domain in a time-series of frames, as shown in Fig. 4.5. The Gaussian pulse input waveform propagates downwards and undergoes reflection and transmission upon reaching the dielectric interface. Field values are given at four time instants (the 400th, 500th, 600th, and 800th timesteps) to show the propagation of the wave.

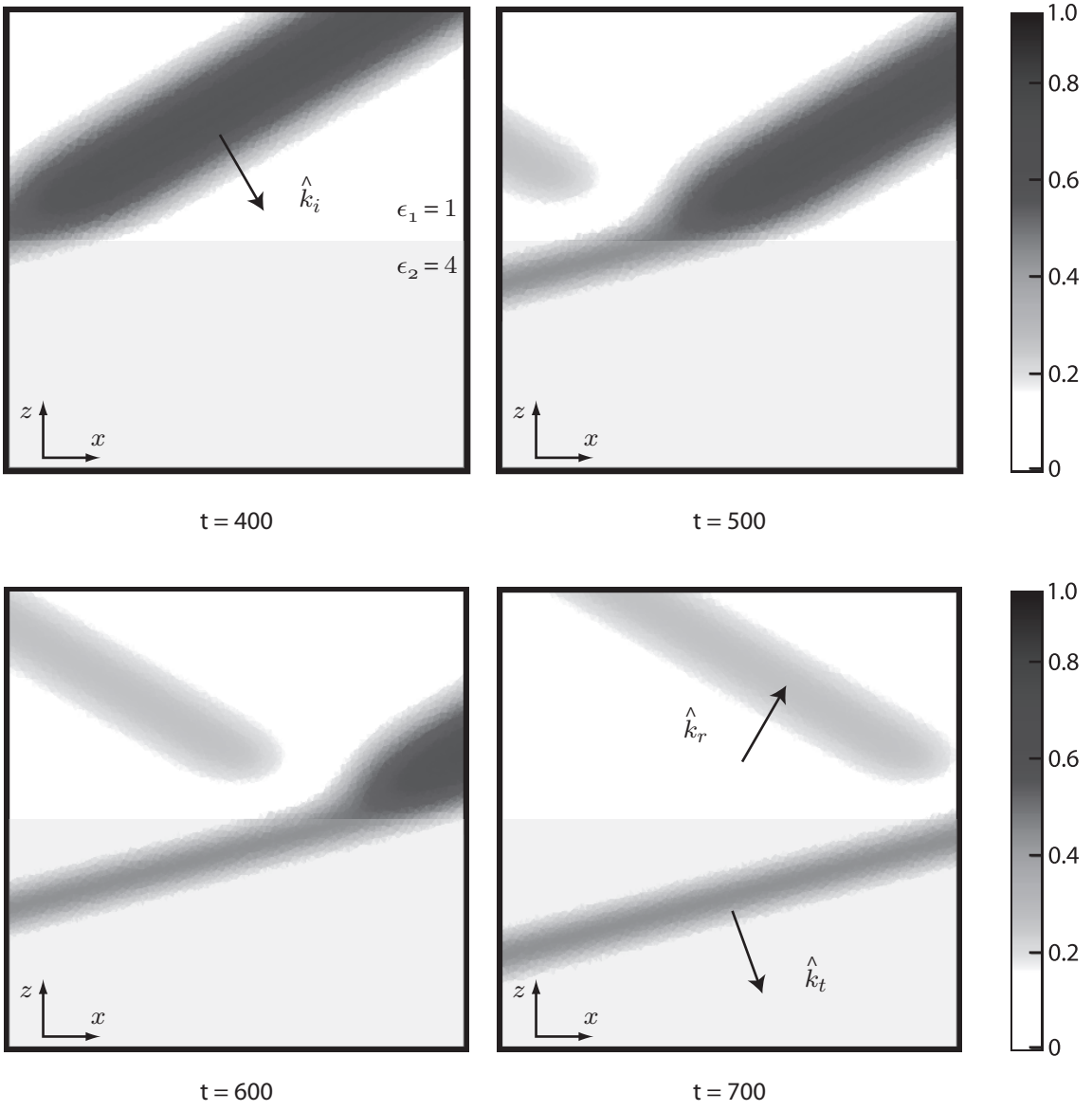

Fig. 4.5: Time-series of field values in the FVTD mesh as a function of time for a TE wave incident upon a half-space at an incident angle of 30°. The Gaussian pulse input waveform propagates downwards and undergoes reflection and transmission upon reaching the dielectric interface. t=400, 500, 600, 800 indicates the 400th, 500th, 600th, and 800th timesteps, respectively.

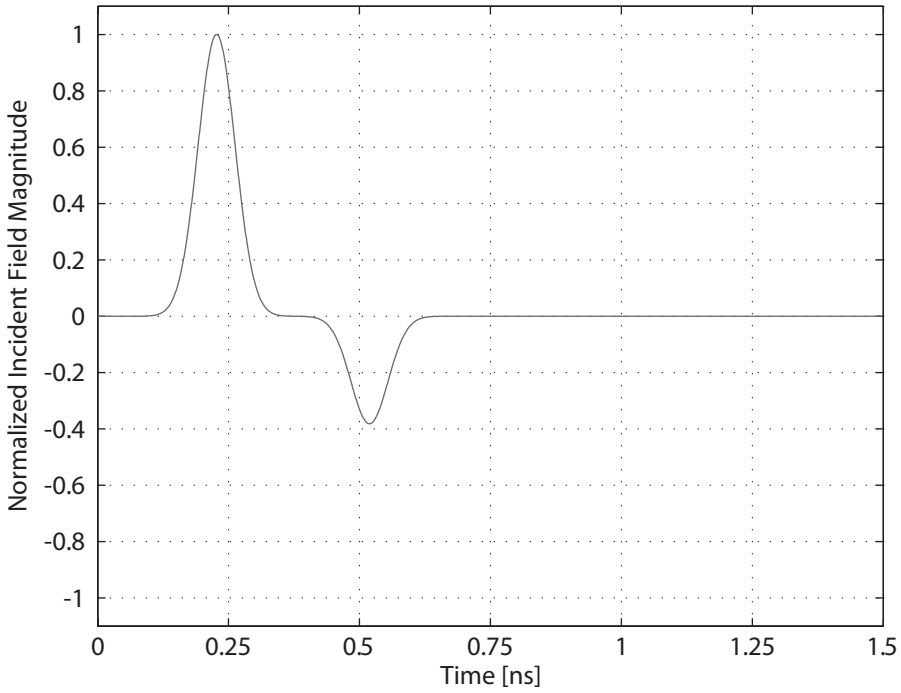

Fig. 4.6: Time history of the y-component of the electric field at an observation point located at x = 0.03, y = 0.0075, z = 0.05. The peak of the initial pulse is seen at about 0.23 ns and the peak of the reflected pulse is seen at about 0.52 ns. The reflected pulse is negative since the lower half-space has a larger dielectric constant than the upper half-space.

While the images of Fig. 4.5 are useful for visualizing the fields throughout the computational domain, they require a lot of storage. More often, we visualize the field results at individual observation points. As an example, an observation point was placed at x = 0.03, y = 0.0075, and z = 0.05, which is above the surface. The time-domain electric fields at that observation point are shown in Fig. 4.6. The incident pulse propagates past the observation from 0.12 ns to 0.32 ns and the reflected field from the dielectric half-space is seen from 0.42 ns to 0.62 ns. The (negative) peak value of the reflected field is -0.3816. For a semi-infinite half-space with dielectric

constant of $\epsilon_r = 4$, the Fresnel reflection coefficient can be calculated as -0.3955, which gives a relative error of about 3%. We also performed the same simulation for normal incidence and found that the peak value of the reflected field was -0.3334 (not shown in the figure). The Fresnel reflection coefficient would give a value of -0.3333, which gives a relative error is less than 0.1%. As the incidence angle increases, we see an increase in the error, similar to other FDTD researchers.

The second case is a series of lossy dielectric layers. Again, the input waveform is a Gaussian pulse. The geometry of the multi-layer problem is imposed on Fig. 4.7. The x-dimension is 0.12 [m], the y-dimension is 0.015 [m], and the z-dimension is 0.12 [m] in total. We placed several observation points centered parallel to z-axis in order to provide a time-domain plot of the propagation of the wave through the computational domain. We demonstrate the propagation of the wave through the computational domain in a time-series of frames, as shown in Fig. 4.7. The Gaussian pulse input waveform propagates downwards and undergoes reflection and transmission upon reaching the dielectric interface. Field values are given at four time instants (the 400th, 600th, 700th, and 800th timesteps) to show the propagation of the wave.

We placed an observation point was placed at x = 0.03, y = 0.0075, and z = 0.05, which is similar to the half-space example. The time-domain electric fields at that observation point are shown in Fig. 4.8. The incident pulse propagates past the observation from 0.12 ns to 0.32 ns and the reflected field from the dielectric halfspace is seen from 0.42 ns to 0.62 ns. In this case, we observe multiple reflected pulses

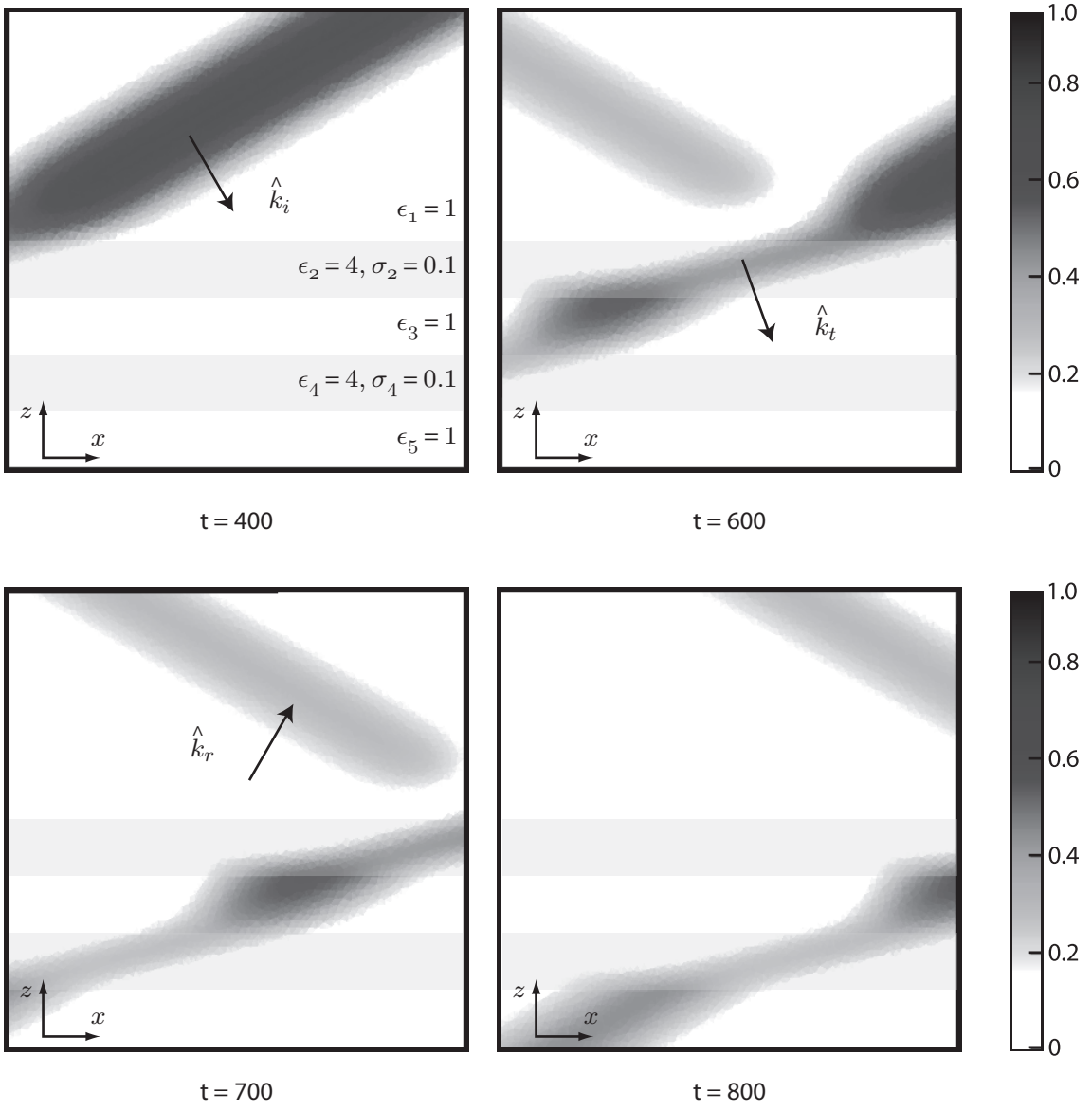

Fig. 4.7: Time-series of field values in the FVTD mesh as a function of time for a TE wave incident upon a multi-layered medium at an incident angle of 30°. The Gaussian pulse input waveform propagates downwards and undergoes reflection and transmission upon reaching the dielectric interface. t=400, 600, 700, 800 indicates the 400th, 600th, 700th, and 800th timesteps, respectively.

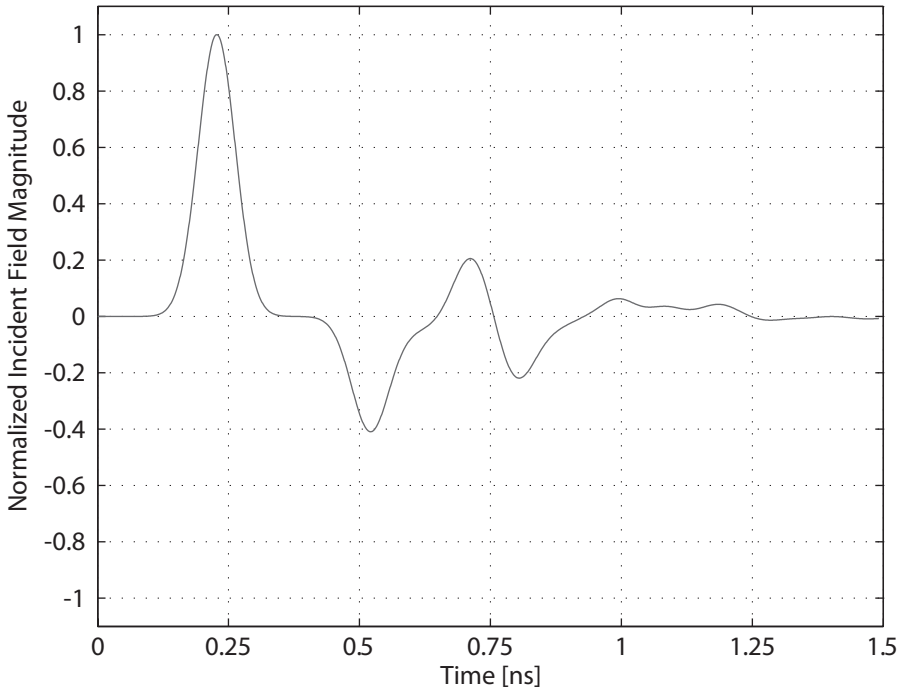

Fig. 4.8: Time history of the y-component of the electric field at an observation point located at x = 0.03, y = 0.0075, z = 0.05 (above a multi-layered medium). The peak of the initial pulse is seen at about 0.23 ns and the peak of the first reflected pulse is seen at about 0.52 ns. Multiple pulses are observed at the observation point due to the reflections and transmissions across the multiple layers.

corresponding to the multiple layers. The magnitude of the pulses decrease partially due to the multiple reflections and transmissions, and partially due to the loss in the layers.

4.4.2 Scattering from a Dielectric Sphere

For our first scattering example, we consider a dielectric sphere in a free-space background. In this case, we are able to compare our results with the commercially available software program, FEKO ©. The permittivity value of the sphere is set

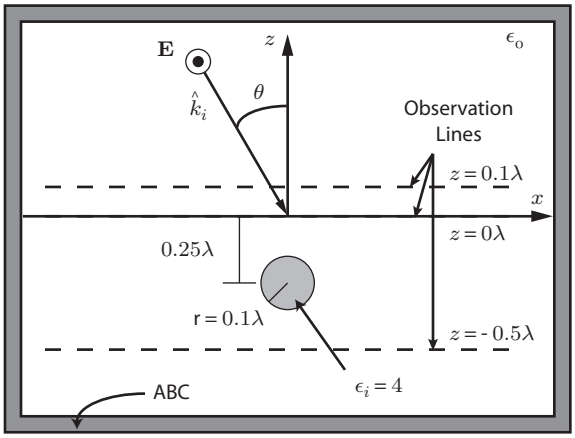

Fig. 4.9: Geometry of the FVTD computational domain for a dielectric sphere in free space. Observation lines are indicated by dashed lines in the diagram.

to $\epsilon_i = 4$ and the radius of the sphere is $\lambda/10$. The geometry of the problem (for FVTD) is given in Fig. 4.9 and the results of our computations using both FVTD and FEKO at $z = -0.25\lambda$, $z = 0\lambda$, and $z = 0.01\lambda$ are given in Fig. 4.10. The excellent agreement between the results shows the validity of the scheme.

4.4.3 Scattering from a Dielectric Cube

For our next example, we consider a dielectric cube buried in a half-space medium. Both the half-space and the dielectric cube are lossy, with permittivity values of $\epsilon_b = 3 - j0.1$ and $\epsilon_i = 2.9 - j0.05$. To calculate the conductivity that must be used in the FVTD simulations, we used a frequency of 6 GHz, which gives conductivities as $\sigma_b = 0.03338$ $[S/m]$ and $\sigma_i = 0.01669$ $[S/m]$. Our results are normalized to the free-space wavelength, as in [93]. The geometry of the problem is given in Fig. 4.11 and the results of our computations at $z = 0.1\lambda$ are given in Fig. 4.12. In comparison

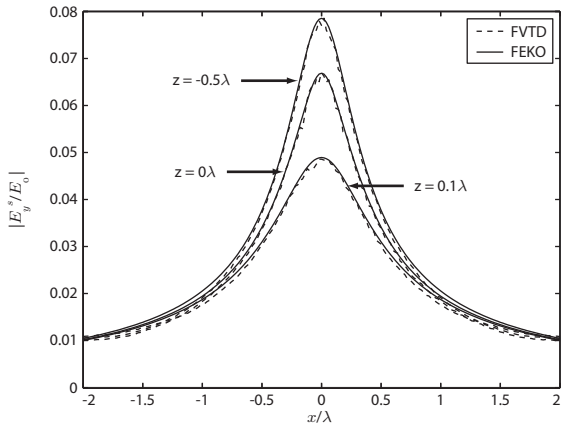

Fig. 4.10: Scattered electric fields for a dielectric sphere in free space. FVTD results are compared with FEKO ©.

with [93], our results are slightly higher; however, in comparison with [98], our results are very similar. For example, our peak value at $z = 0.2\lambda$ is 0.002, while [93] reports 0.0017 and [98] reports 0.002. The difference is associated with the error in using the Born approximation [98]. The decay of the curve appears to be in agreement as well.

4.4.4 Scattering from a Dielectric Box

To show the variation of the scattered electric fields as a function of incidence angle, we consider another one of the examples presented in [93]. In this case, the buried object is a rectangular box, with a size given by 0.6λ, 0.2λ and 0.066λ for the x, y, and z-dimensions, respectively. The geometry of the problem is given in Fig. 4.13 and the results of our computations are given in Fig. 4.14. For $\theta_i \neq 0^\circ$ the peak of the scattered field has shifted toward the specular direction and the magnitude of the peak decreases as the incidence angle increases. This is similar to the result

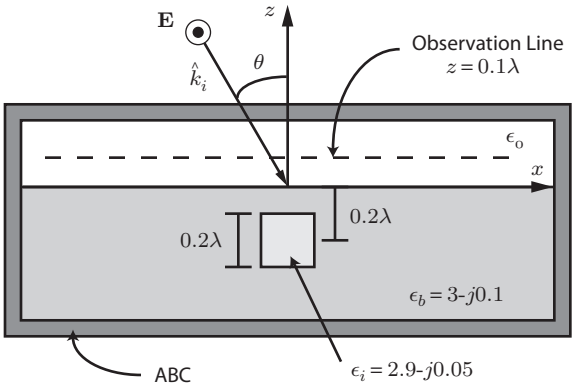

Fig. 4.11: Geometry of the FVTD computational domain for a lossy dielectric cube buried in a lossy half-space. Observation lines are indicated by dashed lines in the diagram.

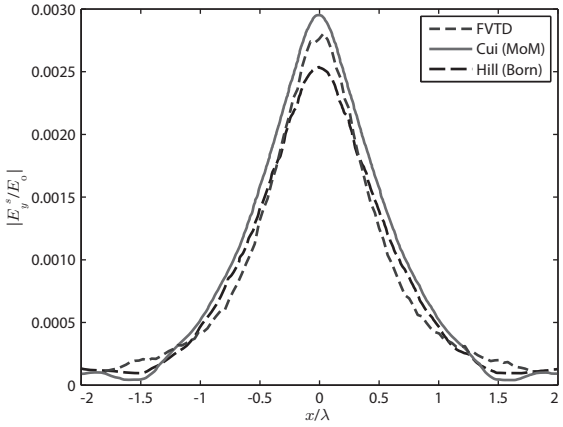

Fig. 4.12: Scattered electric fields for a lossy dielectric cube buried in a lossy half-space at $z = 0.1\lambda$. FVTD results are compared with [98] (Cui, MoM) and [93] (Hill, Born Approximation).

observed in [93], although our magnitudes are slightly different because those in [93] are obtained using an approximate technique.

4.4.5 Scattering from a Dielectric Slab in a Half-Space

The previous examples considered were weak scatterers, i.e. the dielectric contrast is not very large. For this example, we consider a stronger scatterer, following the examples in [98]. Both the half-space and the dielectric slab are lossy, with permittivity values of $\epsilon_b = 4 - j0.5$ and $\epsilon_i = 10 - j5$. At the frequency of 6 GHz the conductivities are $\sigma_b = 0.16689$ $[S/m]$ and $\sigma_i = 1.6689$ $[S/m]$. The geometry of the problem is given in Fig. 4.15 and the results of our computations are given in Fig. 4.16. In comparison with [98], our results are similar, but slightly lower, similar to the example of the dielectric cube. For example, our peak value at $z = 0.002\lambda$ is 0.081, while [98] reports 0.092 at $z = 0$, yielding a relative error of about 12%. As another example, our peak value at $z = 0.01\lambda$ is 0.0599, while [98] reports 0.066 at $z = 0.01\lambda$, yielding a relative error of about 9%. We consider this relative error to be acceptable considering the differences in the computational methods. As an additional test, we rescaled our simulation results to the peak value of the result at $z = 0$ and these results are presented in Fig. 4.17. It is clear that our results match up extremely well with those of [98] as long the as they are normalized.

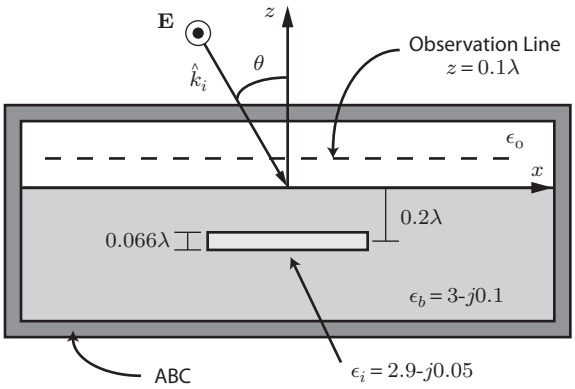

Fig. 4.13: Geometry of the FVTD computational domain for a lossy dielectric box buried in a lossy half-space. Box dimensions are 0.6λ, 0.2λ and 0.066λ for the x, y, and z-dimensions, respectively.

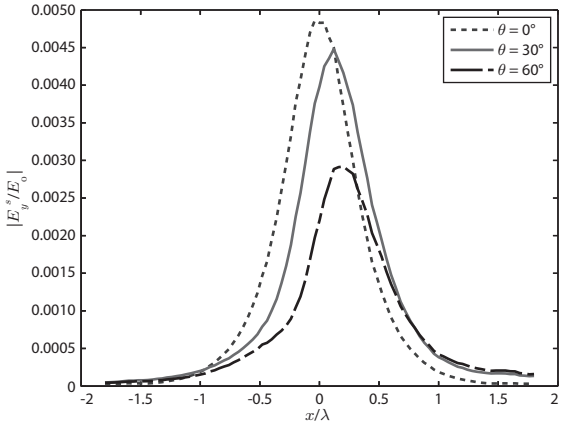

Fig. 4.14: Scattered electric fields for various incidence angles for a lossy dielectric box buried in a lossy half-space.

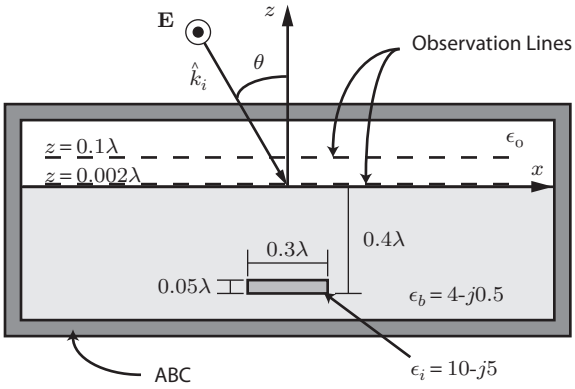

Fig. 4.15: Geometry of the FVTD computational domain for a lossy dielectric slab buried in a lossy half-space. Slab dimensions are 0.3λ, 0.3λ and 0.05λ for the x, y, and z-dimensions, respectively.

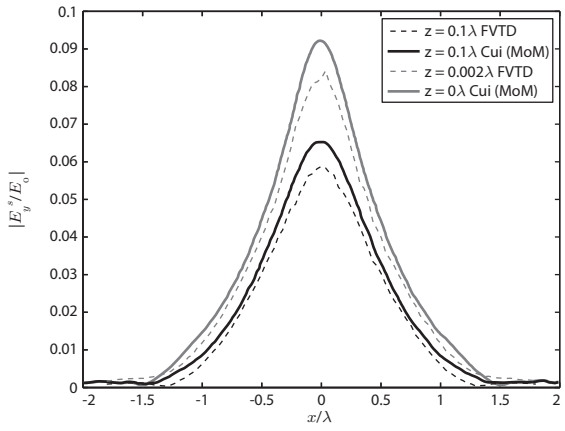

Fig. 4.16: Scattered electric fields for a lossy dielectric slab buried in a lossy half-space. FVTD results are compared with [98] (Cui, MoM).

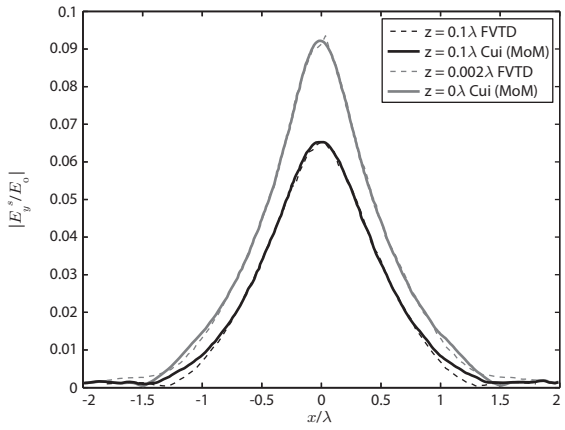

Fig. 4.17: Scattered electric fields for a lossy dielectric slab buried in a lossy half-space. FVTD results are normalized to [98] (Cui, MoM).

4.4.6 Scattering from a Dielectric Slab in Multi-layered Media

As a modification to the dielectric slab example, we consider the same slab buried under a lossy dielectric layer. Again, the half-space and the dielectric slab are lossy, with permittivity values of $\epsilon_b = 4 - j0.5$ and $\epsilon_i = 10 - j5$, with the lossy layer of $\epsilon_1 = 6 - j2$. The conductivity of the lossy layer is $\sigma_1 = 0.66756$ $[S/m]$. The geometry of the problem is given in Fig. 4.18 and the results of our computations are given in Fig. 4.19. In comparison with [98], our results are very similar. For example, our peak value at $z = 0.002\lambda$ is 0.0387, while the corresponding peak value reported in [98] is 0.042, yielding a relative error of about 8%. As another example, our peak value at $z = 0.01\lambda$ is 0.0283, while [98] reports 0.031 at corresponding to the same height above the surface, yielding a relative error of about 9%. We consider this to be acceptable considering the differences in the computational methods. Again, as an additional test, we rescaled our simulation results to the peak value of the result at

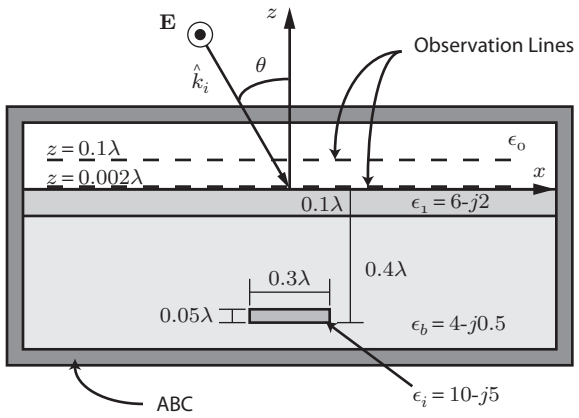

Fig. 4.18: Geometry of the FVTD computational domain for a lossy dielectric slab buried in a lossy multi-layered medium. Slab dimensions are 0.3λ, 0.3λ and 0.05λ for the x, y, and z-dimensions, respectively.

$z = 0$ and these results are presented in Fig. 4.20. This scale-factor was the same value as in the previous example (slab in a half-space). It is clear that our results match up extremely well with those of [98] as long as they are normalized. Since the slab buried in a half-space and the slab buried in a multi-layered medium had the same scale-factor, we hypothesize that this is a constant difference between the two methods. The exact nature of the difference cannot be determined at this point; however, we are confident that our methodology is sound due to our accurate comparison with the sphere in free-space using FEKO ©.

4.4.7 Scattering from Dielectric Spheres

In most of our previous examples we used shapes with a cubic geometry, yet in our introduction we suggested that one of the major benefits of using the FVTD method versus the FDTD method was the ability to have a mesh conform to an irregular

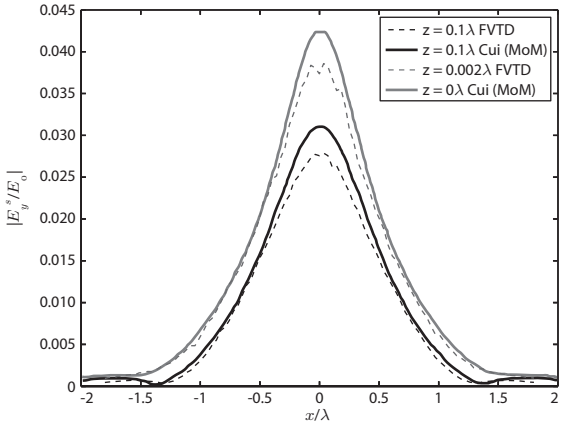

Fig. 4.19: Scattered electric fields for a lossy dielectric slab buried in a lossy multi-layered medium. FVTD results are compared with [98] (Cui, MoM).

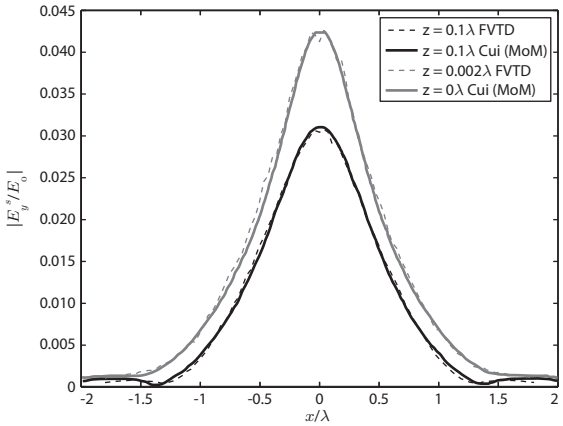

Fig. 4.20: Scattered electric fields for a lossy dielectric slab buried in a lossy multi-layered medium. FVTD results are normalized to [98] (Cui, MoM).

surface. In this example we present the scattering for multiple spheres buried in a dielectric half-space. This type of problem is very common in scattering simulations of geophysical media, where the sub-surface can be populated with regions of dielectric discontinuity (for example, brine pockets in sea ice). The proximity of spheres is also an issue in studies involving the homogenization of random media [100]. The geometry of the computational domain for the case of two spheres is shown in Fig. 4.21. We simulated the scattering from both spheres simultaneously, from sphere 1 only (the left-hand sphere in Fig. 4.21), and from sphere 2 only (the right-hand sphere in Fig. 4.21). The simulation results are presented in Fig. 4.22, where we have also plotted the superposition of the scattering from sphere 1 and sphere 2. It is clear from the plotted results that multiple spheres must be simulated simultaneously since an attempt to approximate the scattering by superposition does not apply when the spheres are in close proximity. The importance of the proximity effect was also discussed in [101], particularly with regards to discrete modeling in remote sensing studies. Since our future work includes modeling electromagnetic scattering for remote sensing, it is important that we should examine and consider these effects before embarking on such modeling studies.

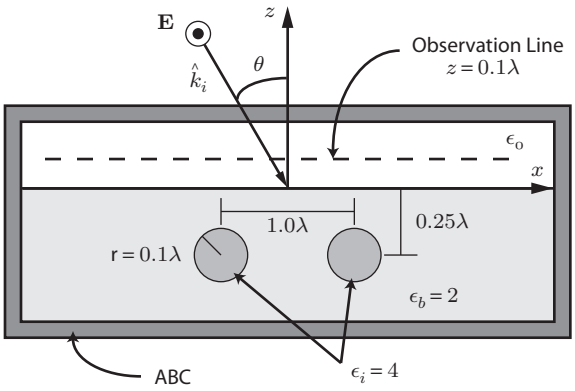

Fig. 4.21: Geometry of the FVTD computational domain for dielectric spheres buried in a half-space. Sphere radii are 0.1λ, separation is 1.0λ, sphere centers are at $z = -0.25\lambda$.

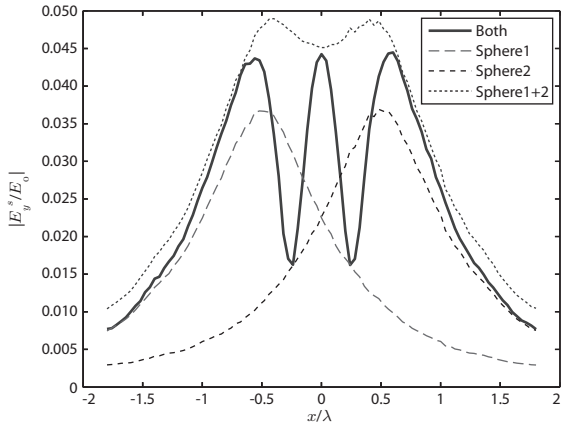

Fig. 4.22: Scattered electric fields for spheres buried in a half-space. Solid line: simultaneous scattering from both spheres, dotted line: superposition of sphere 1 and sphere 2 scattered fields.

4.5 Chapter Conclusions and Discussion

Through incorporating the scattered-field formulation for multi-layered media in an FVTD engine, an efficient method of modeling complex layered media has been developed. We have presented details of the method used to calculate electromagnetic scattering from objects buried in multi-layered media, which has a wide range of potential application. Our method is capable of calculating the scattering from multiple objects with minimal increase in the number of unknowns in the computation. Comparisons with other published data in the literature provided good agreement, giving us confidence in the FVTD implementation that we have developed.

This novel numerical technique can be used to simulate the scattering of geophysical media by assigning appropriate values of the layer dielectrics. Moreover, since we are interested in simulating backscattering for the purposes of comparison with experimentally measured scattering, further development is needed. Primarily, since the layer interfaces are perfectly smooth, there is no backscatter at all. The following chapter presents some methods that are required to use the developed techniques in a scattering model for remote sensing.

5. SIMULATION TECHNIQUES FOR ROUGH SURFACE SCATTERING AND WAVE PROPAGATION

In this chapter, we address fundamental modeling concepts that are generally present in an electromagnetic remote sensing model. First, we discuss how the results of our numerical simulations will be translated into variables that we can compare with the radar measurements. This includes the development of a Monte Carlo method and an approximation method to perform the near-field to far-field transformation. Next, we develop a technique for modeling the scattering from a rough surface using the FVTD method. Finally, we present a numerical technique that shows how FVTD can be used to calculate an average dielectric of an inhomogeneous dielectric medium, or alternatively, shows how FVTD can be used to calculate volumetric scattering. The chapter concludes with a discussion of implications of our model for the application of sea ice remote sensing.

5.1 Components of a Remote Sensing Model

The prime variable retrieved from the scatterometer system is the normalized radar cross section (abbreviated as NRCS, and symbolically denoted as σ^0). The output of our Monte Carlo simulation technique must therefore be the NRCS in order to facilitate comparison between simulation results and measured results. This value is obtained through the application of Monte Carlo simulation techniques and the application of the near-field to far-field transformation in the FVTD method.

5.1.1 A Monte Carlo Method for Rough Surface Scattering Simulations

As was presented in Chapter 2, Monte Carlo techniques fall into the category of non-deterministic methods. The stochastic aspect of our Monte Carlo method comes from the generation of many different realizations of a random rough surface. Each individual realization of the random rough surface provides a unique sample. This is in contrast to our examples in the previous chapter, which were deterministic in that our scattering objects and layers were fixed in time and space.

In order to calculate the NRCS of a random medium, the statistical properties of the scattered power must be used. The scattered-field from a random medium can be separated into the coherent and incoherent components. In essence, the coherent component is the mean value of the field, whereas the incoherent component is the variance of the field. For a complex random variable, $\rho = a + jb$, where $j = \sqrt{-1}$, the

variance, var$\{\rho\}$ is given by [78]:

$$\text{var}\{\rho\} = \langle \rho\rho^* \rangle - \langle \rho \rangle \langle \rho^* \rangle, \tag{5.1}$$

where $\langle . \rangle$ denotes ensemble averaging of the quantity within the angled brackets.

In the case of randomly rough surfaces, this random variable is the scattered field. When the surface is completely smooth, then the variability vanishes and the scattered field is completely specular (i.e. zero backscatter). Increasing the roughness of the surface generally increases the backscatter, but there are also dependencies on other variables such as frequency and roughness scales. These are discussed later in this thesis.

For an area-extensive target, such as a rough half-space, the normalized radar cross section is computed using the far-field quantities in the following expression [38]:

$$\sigma^0(\theta_{sc}, \phi_{sc}, \theta_{inc}, \phi_{inc}) = \lim_{R \to \infty} 4\pi R^2 \frac{\langle S^{sc}(\theta_{sc}, \phi_{sc}) \rangle}{A_0 S^{inc}(\theta_{inc}, \phi_{inc})}, \tag{5.2}$$

where A_0 is the area of illumination, $S^{sc}(\theta_{sc}, \phi_{sc})$ is the scattered power in the direction θ_{sc}, ϕ_{sc}, $P^{inc} = A_0 S^{inc}(\theta_{inc}, \phi_{inc})$ is the incident power.

We are interested primarily in the incoherent power, which can be obtained using the following expression:

$$P^{incoherent} = \left\langle |E^c - E^n|^2 \right\rangle \tag{5.3}$$

where the superscript c represents the coherent field and n represents the field from the n^{th} Monte Carlo simulation. We are interested in calculating the incoherent fields since the backscatter at microwave frequencies should be primarily incoherent. Removal of their influence is achieved through the use of equation (5.3).

The expression for calculating the NRCS, equation (5.2), requires far-field values. Obtaining these far-field values requires an approximation technique, which is presented in the next sub-section.

5.1.2 Near-Field to Far-Field Transformation

The uniqueness theorem states that the field within a closed region is uniquely defined by the tangential components of the electric or magnetic fields on the boundary of the region. By the surface equivalence theorem, the fields outside of a closed surface can be found by "placing" an equivalent surface electric current density, $\mathbf{J}_s$, and surface magnetic current density, $\mathbf{M}_s$, on the surface, such that the fields outside of the surface are equal to the radiation produced by the actual sources within the surface. While theoretically exact, the final accuracy depends on the how accurately the tangential fields can be described.

One of the primary goals of our work is to create a model that provides a favorable comparison with the NRCS measured by the scatterometer. The scatterometer has a finite beamwidth, and so, we make an approximation on the description of the tangential fields. We consider the footprint of the antenna to lie solely over the FVTD

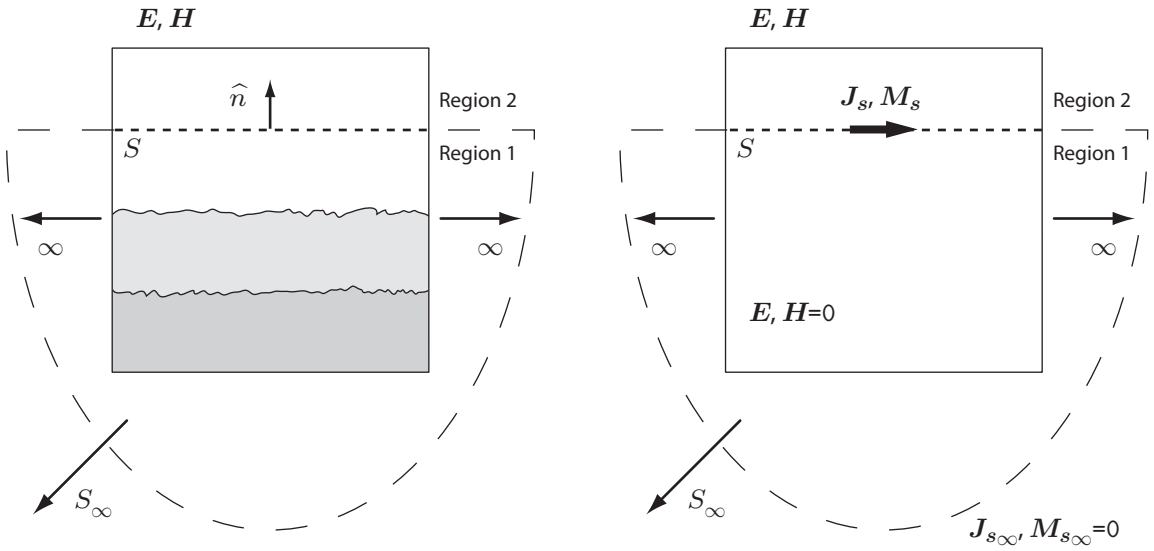

Fig. 5.1: An approximation to the equivalent surface in the near-field to far-field transformation

computational domain. The incident fields vanish in all regions outside of the FVTD computational domain (i.e. they are considered to be outside of the footprint of the antenna pattern on the surface of the volume of interest). Since there is no illumination, there can be no scattered-field generated, and therefore there is no contribution to the radiated fields. This is illustrated in the left-hand image of Fig. 5.1, where we show the equivalent surface, which is the union of S and S_∞. By applying an approximation of the surface equivalent theorem, the right-hand image of Fig. 5.1 is obtained, where the fields on surface $S_\infty \to 0$, or equivalently, $\mathbf{J}_{s\infty} = \mathbf{M}_{s\infty} = 0$. In this case, only $\mathbf{J}_s = \mathbf{M}_s \neq 0$ and these fields are used to compute the far-field transformation.

This method works when the scattering object consists of a large number of distributed scattering centers, such as a randomly rough surface or randomly distributed

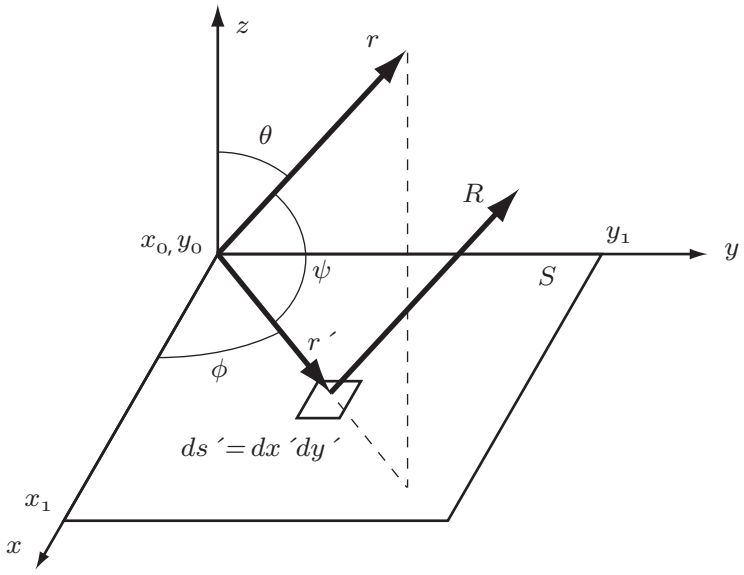

Fig. 5.2: The coordinate system used for the computation of the far-field transformation.

spheres in space. The approximation does not appear to be valid for when there is a single object, in which case, the fictitious surface should completely bound the scattering object and the appropriate Green's function should be used to transform the fields in the FVTD computational domain to the far-field.

Given that the fields on S are approximately described, we can apply a far-field transformation. Referring to the geometry of Fig. 5.2, we assume that the electric and magnetic fields exist on the finite surface S and are zero elsewhere. The equivalent electric and magnetic currents are calculated using the following equations:

$$\mathbf{J} = \hat{n} \times \mathbf{H}, \tag{5.4}$$

$$\mathbf{M} = -\hat{n} \times \mathbf{E}, \tag{5.5}$$

and for far-field observations, we approximate R as:

$$R \cong r - \mathbf{r}' \cos\psi, : \text{ for phase variations,} \tag{5.6}$$

$$R \cong r, : \text{ for amplitude variations.} \tag{5.7}$$

We calculate the radiation integrals using the following equations [102]:

$$E_r \cong 0 \tag{5.8}$$

$$E_\theta \cong -\frac{jke^{-jkr}}{4\pi r}(L_\phi + \eta N_\theta) \tag{5.9}$$

$$E_\phi \cong +\frac{jke^{-jkr}}{4\pi r}(L_\theta - \eta N_\phi) \tag{5.10}$$

$$H_r \cong 0 \tag{5.11}$$

$$H_\theta \cong \frac{jke^{-jkr}}{4\pi r}(N_\phi - \frac{L_\theta}{\eta}) \tag{5.12}$$

$$H_\phi \cong -\frac{jke^{-jkr}}{4\pi r}(N_\theta + \frac{L_\phi}{\eta}) \tag{5.13}$$

$$\tag{5.14}$$

where N_θ, N_ϕ, L_θ, and L_ϕ are calculated as:

$$N_\theta = \int_S [J_x \cos\theta \cos\phi + J_y \cos\theta \sin\phi - J_z \sin\theta] e^{+jk\mathbf{r}'\cos\psi} ds' \tag{5.15}$$

$$N_\phi = \int_S [-J_x \sin\phi + J_y \cos\phi] e^{+jk\mathbf{r}'\cos\psi} ds' \tag{5.16}$$

$$L_\theta = \int_S [M_x \cos\theta \cos\phi + M_y \cos\theta \sin\phi - M_z \sin\theta] e^{+jk\mathbf{r}'\cos\psi} ds' \tag{5.17}$$

$$L_\phi = \int_S [-M_x \sin\phi + M_y \cos\phi] e^{+jk\mathbf{r}'\cos\psi} ds' \tag{5.18}$$

and where $k = 2\pi/\lambda$.

When using our FVTD-based scattering model, we calculate the far-fields in a post-processing step, after the simulation has terminated. The electric and magnetic fields that are used in our calculation of these equations are time-harmonic values, and so, a technique to obtain the time-harmonic component at a desired frequency is needed. This is accomplished through the Discrete Fourier Transform (DFT), as discussed next.

5.1.3 Discrete Fourier Transform

In our model, we ultimately desire the solution at several discrete frequencies. Therefore, a frequency domain method is used to calculate the near-field to far-field transformation. A plane of observation points are placed in the simulation space parallel to the xy-plane, but slightly above the surface (surface S in Fig. 5.1). We have the option of storing the complete time history of the scattered fields at the observation point, computing a Fast Fourier Transformation (FFT) on each of these points, and subsequently finding the frequency component of interest; however, this is inefficient for two reasons.

First, the amount of memory required to store the observations points becomes quite prohibitive. For example, using an array that is 31 by 31 points yields 961 observation points, each with six scattered field components and six incident field components. If there are 2000 timesteps, then that translates to 24000 $\times$ 961 values,

or about 23 million values. This is much larger than storing only the required frequency domain component, which would require $961 \times 6 \times 2$, or 11532 values (6 complex-valued field components).

Second, if we want the value of the field at a frequency of 5.5 GHz, then we must take the FFT with sufficient zero-padding to obtain the desired frequency component. Even so, we may find that the result is not exactly 5.5 GHz (for example it could be actually at 5.498 GHz). Although the error is minor, it is an error that we can eliminate by performing a Discrete Fourier Transform (DFT) on the fly during the FVTD computations. We perform the DFT at each of the observation points and then discard previous time values. We can look at the output of the DFT calculation to see if the results converged at each observation point. After the FVTD simulation has terminated, a simple numerical integration is performed to calculate the radiation integrals [103].

5.1.4 Calculation of the NRCS

With the far-field components available, we now have all of the field values that are needed to calculate the NRCS by equation (5.2). We place a plane of observation points parallel to xy-plane and above all scattering objects in the computational domain. Both the time-harmonic scattered-field and incident-field values are stored at these locations.

We first calculate the incident power upon the surface by setting up a computational

geometry that is only free space. In this FVTD simulation, the incident field for layered media is therefore propagating only in free space and is not perturbed by any layered dielectric. The incident power can be calculated using the following integral, which is evaluated numerically on the same observation plane as the scattered field, and uses the time harmonic values of the field quantities. This quantity must be calculated for each separate incidence angle.

$$P^{inc} = \frac{1}{2} Re \left\{ \int_{y_1}^{y_2} \int_{x_1}^{x_2} \mathbf{E}^{inc} \times \mathbf{H}^{inc*} dx dy \right\}. \tag{5.19}$$

where x_1 and x_2 are the bounds of the observation plane in the x-dimension, y_1 and y_2 are the bounds of the observation plane in the y-dimension, and $\mathbf{E}^{inc}$ and $\mathbf{H}^{inc*}$ are the time-harmonic incident-field values, and the $*$ denotes the complex conjugate.

We perform a series of Monte Carlo simulations on a number of realizations of a random media and store the scattered-fields on the same observation plane for each realization. The near-field to far-field transformation is calculated for each realization separately, and then the incoherent component of the power in the scattered fields is extracted using equation (5.3). Finally, we use the incoherent component of the power in the calculation of the NRCS by equation (5.2) and take the value that corresponds to the backscattering direction ($\theta_{sc} = -\theta_{inc}$). This gives us the variable (i.e. σ^0) that we need for comparison with other modeling techniques and with experimentally obtained scatterometer data.

5.2 Rough Surface Modeling

Since the interfaces of a multi-layered medium can be rough in general, we sought a way to physically model the variations of the surface for use in the FVTD engine. We used the method provided by Bergström *et al.* [104] to initially define the rough surface. Their method gave us an N-by-N array of points whose values represent the heights of the rough surface, but we needed a way to transform the definition of the rough surface into a physical surface for the FVTD engine. We also needed to provide a comparison with some other method in order to validate our technique. This section describes the statistical definitions of a randomly rough surface, provides a method to create a geometry for use in the FVTD engine, and demonstrates the method for a variety of rough surface parameters.

Material in this section has been published by the IEEE [105] [1].

5.2.1 Generation of a Rough Surface

A randomly rough surface can be characterized by its autocovariance function (ACF) and its height distribution function (HDF). The ACF describes the lateral variation of distribution (associated with the correlation length, L_c), while the HDF describes the height deviation from a mean value (denoted as σ_r). Commonly used ACFs for rough surfaces include the Gaussian, 1.5-power, and the exponential [40]. Since it

[1] © 2011 IEEE. Reprinted, with permission, from D. Isleifson, L. Shafai, and D. G. Barber, "Numerical Scattering from 3D Randomly Rough Surfaces using FVTD," *2011 IEEE International Symposium on Antennas and Propagation and USNC-URSI National Radio Science Meeting.*

is difficult to obtain field measurements of sea ice surface statistics, the benefit of using one type of ACF over another is not clear [47]. To generate a rough surface, the method presented in [104] and originally given in [106], is employed. The surface is constructed from a 2D matrix of uncorrelated random points, $z_u = f(x, y)$, using a random number generator with a Gaussian distribution.

A Gaussian filter (5.20),

$$F(x, y) = \frac{2}{L_c\sqrt{\pi}} exp(-2(x^2 + y^2)/L_c^2), \tag{5.20}$$

provides the means to obtain a correlation of the points through a convolution operation of the random points with the filter (5.21),

$$z(x, y) = \int_{-\infty}^{\infty}\int_{-\infty}^{\infty} F(x - x', y - y') z_u(x', y') dx' dy'. \tag{5.21}$$

In practice, the convolution operation is performed using an inverse discrete Fourier transform.

There are some general rules that must be followed in order to ensure that the rough surface actually follows a Gaussian distribution as desired. By the Nyquist sampling theorem, there must be more than two points per correlation length. For example, on a surface that has a linear dimension of 0.15 m, with $L_c = 0.01$ m, there must be at least $N = 30$ samples to represent the surface.

The output of the rough surface generator is an N-by-N array of points. The

FVTD engine uses a program called GMSH [99] to create a computational mesh upon which it performs computations. In GMSH, the user must specify the physical description of the domain that will be meshed. For example, consider modeling the scattering from a sphere, as we did in Chapter 4. A user provides a series of points that define the sphere, connects them with curved lines, and then bounds the surface of the sphere. Finally, the object's volume is defined and the program uses a mesh generating algorithm to find an optimal geometrical configuration of the mesh elements. The tetrahedral elements are optimized to be as regular as possible, avoiding making extremely small facets which would make the FVTD computations require an extremely small time-step for its solution.

When creating a 2D randomly rough surface, we must prescribe the z-value of each of the points on a 2D N-by-N array of points. In the limiting case, if the values are all the same, then the surface is perfectly flat. We take values from the 2D N-by-N array of points and place them on a regular grid in the GMSH geometry. The next step is to connect the points and create a surface. Straight lines could be drawn to connect the points in a square gridded-fashion, but we found that this created an excessive computational burden on the mesh generator (i.e. it took a very long time to generate a mesh). We also found that the size of elements became very small, creating a high computational demand on the FVTD engine. Instead of connecting the lines in a square grid, we created a geometry by using a spline to connect three points, as shown in Fig. 5.3. In this manner, we kept the Gaussian statistics of the surface by

ensuring that the splines went through the grid points. At the same time, we reduced the number of surfaces that GMSH needed to optimize and reduced the "jaggedness" of the surface. At the edge of the rough surface, we tapered the surface to the mean z-value of the surface. For the FVTD scattered-field solver, the mesh elements that were above the rough surface were assigned to one physical volume (consisting of free-space), while mesh elements below the rough surface were assigned to a separate physical volume (consisting of a solid dielectric).

5.2.2 Simulation of Scattering from a Rough Surface

To conceptualize the scattering from a rough surface, we consider the situation to be similar to that of radiation from an aperture in aperture theory. Referring to the geometry of Fig. 5.1, we assume that the electric and magnetic fields exist on the finite surface S and are zero elsewhere. A fictitious surface is created, completely bounding the lower half-space. The effective area of illumination is assumed to coincide with the fictitious surface and the equivalent surface currents ($\mathbf{J}_s$ and $\mathbf{M}_s$, not to be confused with the contrast sources $\mathbf{J}_c$ and $\mathbf{M}_c$) can be found. Outside of the effective area of illumination, the contribution of the fields is considered to vanish (i.e. no contribution at all). Our hypothesis is that the rough surface itself can be tapered (i.e. it becomes smooth at the edges) in place of tapering the incident field, a concept which is illustrated in Fig. 5.3. Additionally, providing a tapering method for the plane-wave injector for multiple layers would become rather complicated, and so, we

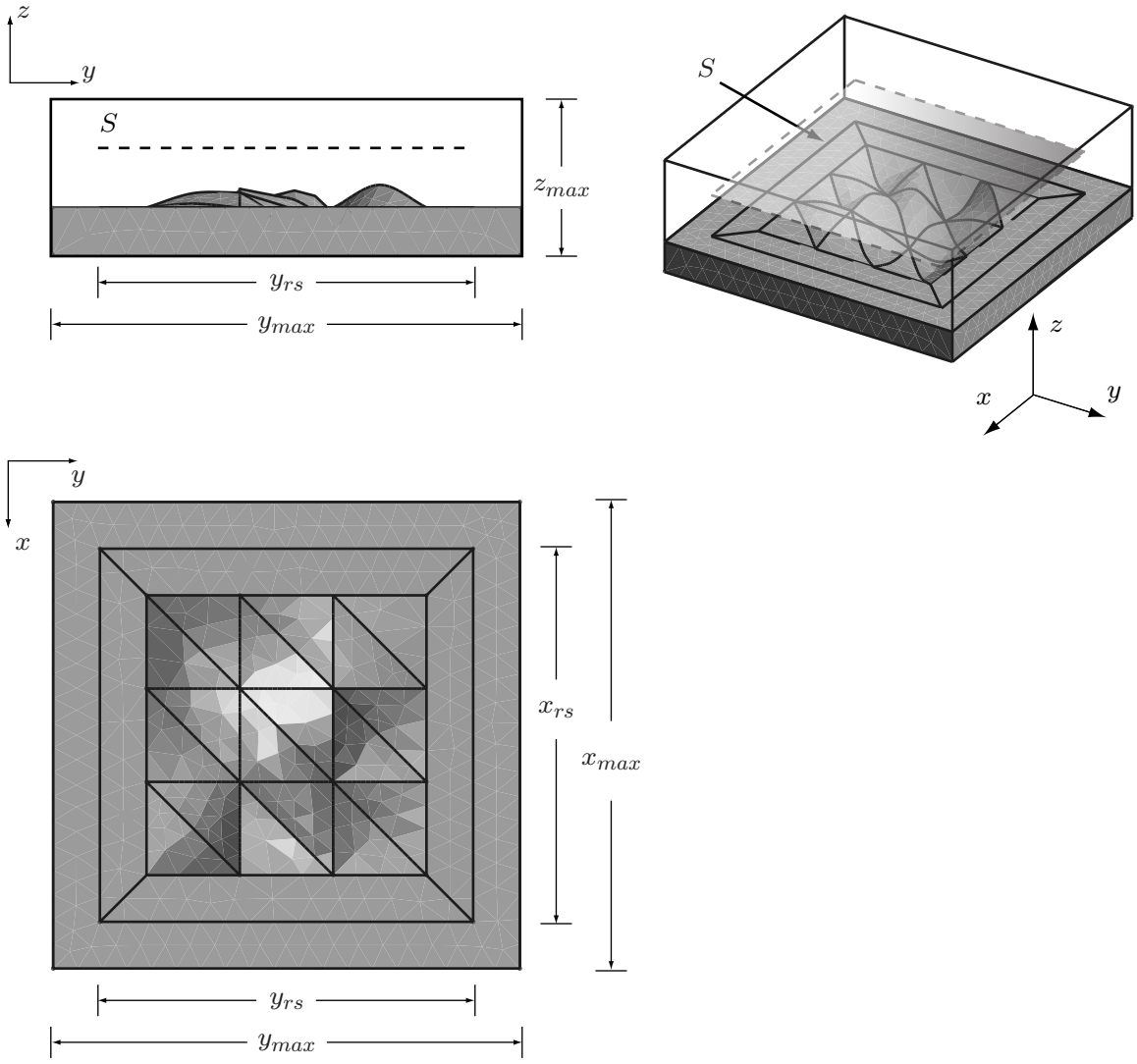

Fig. 5.3: Small version of the mesh used in the rough surface scattering computations. The upper left figure shows a side view of the mesh and indicates the location of the integration surface, S. The lower left figure shows a top view of the mesh and demonstrates how the rough surface geometry was created by placing the points on a triangular grid. The upper right figure shows an isometric view of the rough surface mesh and also shows the location of the integration surface, S, with respect to the rough surface and the computational boundaries.

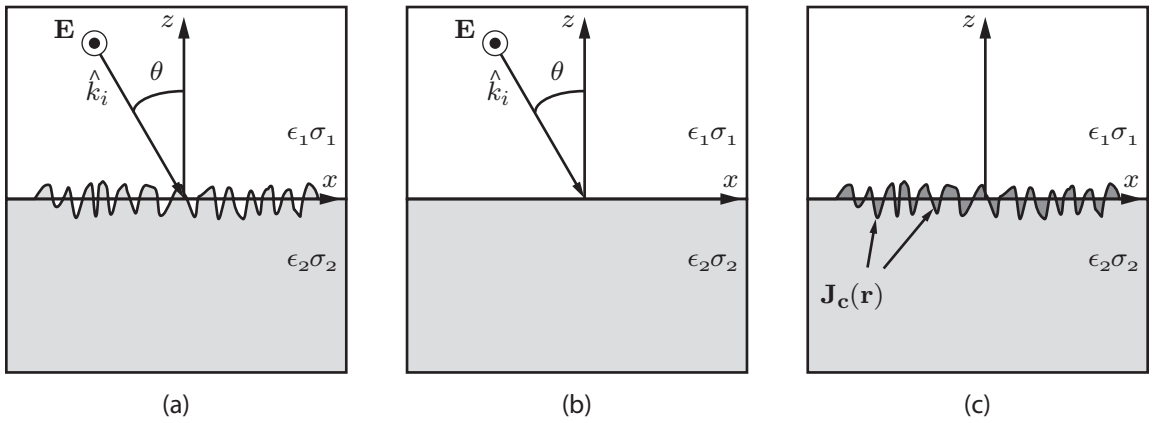

Fig. 5.4: Hypothetical geometry illustrating the decomposition of the fields in the scattered-field formulation for the rough surface scattering problem. a) Total-field geometry with the plane-wave source, **E**, incident upon a rough surface, b) incident-field geometry with only the dielectric half-space and the plane-wave source, and c) scattered-field geometry where the contrast sources, ($\mathbf{J}_c(\mathbf{r})$) which represent the rough surface undulations, radiate in the presence of the half-space background medium.

chose this method.

In Fig. 5.4 we show the scattered-field decomposition, which is similar to Fig. 4.2, except that the contrast sources now lie on the dielectric boundary and the source is a plane-wave. The incident-field is rather simple in this case – it is a plane-wave incident upon a dielectric half-space. The scattered-field is a consequence of the contrast sources caused by the rough surface dielectric discontinuity. By judiciously choosing the computational domain size, we can position a rough surface within the FVTD solution space, such that the propagating scattered-fields will be absorbed by the ABC.

Other researchers have chosen to use an illumination that has a Gaussian taper in

the spatial domain (for example, Fung *et al.* [107], and Hastings *et al.* [108]). This ensures that the incident field does indeed vanish at the edges of the computational domain. In a similar idea to our proposed method, Altuncu *et al.* [109] utilizes the concept of a locally rough interface to model scattering sources above and below a planar interface. Additionally, Marchand and Brown [110] warned that there could be pitfalls in using a plane-wave to illuminate a finite rough surface since the ends of the surface could give large spikes in the surface current, but by using our proposed scattered-field method we observe that the spikes are not there since our scatterers are effectively discrete objects.

Studies on the number of realizations required to reach convergence have been conducted in the past (as discussed by Warnick and Chew [111]). The exact number is not certain, but certainly more realizations increase the accuracy. The cost of conducting more simulations must be weighed against the benefits. Observation of the convergence of the solution as more realizations are added provides confidence in the method. An example plot of the convergence is provided in the demonstration of the technique in the next sub-section.

5.2.3 Numerical Results and Discussion

A series of parametric studies was performed to show the applicability of the proposed method in rough surface scattering. In all examples, we have generated a Gaussian rough surface, as described in Section 5.2.1. The meshes are similar to those shown in

Fig. 5.3. Monte Carlo simulations were performed in parallel on a computing cluster in order to reduce the computation time per simulation.

For statistical purposes, 20 rough surface examples were generated for each set of roughness parameters. The statistics on the rough surface were examined in each case to ensure that the correct surface distribution was used in the comparisons with the small perturbation model (SPM) for rough surface scattering. As an example, the HDF of one of the Monte Carlo runs (Simulation RS2) is plotted in Fig. 5.5 and the ACF is plotted in Fig. 5.6. The plot of Fig. 5.5 shows that the height distribution does indeed follow a Gaussian distribution, as desired. The prescribed correlation length and height variance are slightly different from the actual values obtained when generating the surfaces due to the finite size and number points used to represent the rough surface. When performing a comparison with the SPM, the actual values from the statistical analysis were used, rather than the originally prescribed correlation values. For example, the ACF in Fig 5.6 shows an evaluated correlation length of $L_c = 0.00488$, which is slightly different from the prescribed value of $L_c = 0.005$. The deviation of the calculated ACF from the ideal Gaussian is a result of the finite size of our simulation space, and so, we acknowledge this as a source of modeling error.

We conducted many simulations and conceptual tests (discussed later in this section) which are summarized in Table 5.1. The terms RS1, RS2, and RS3 are simply a naming convention that we used to describe separate Monte Carlo runs. The value of σ_r was kept constant through our simulations, while the correlation length L_c was

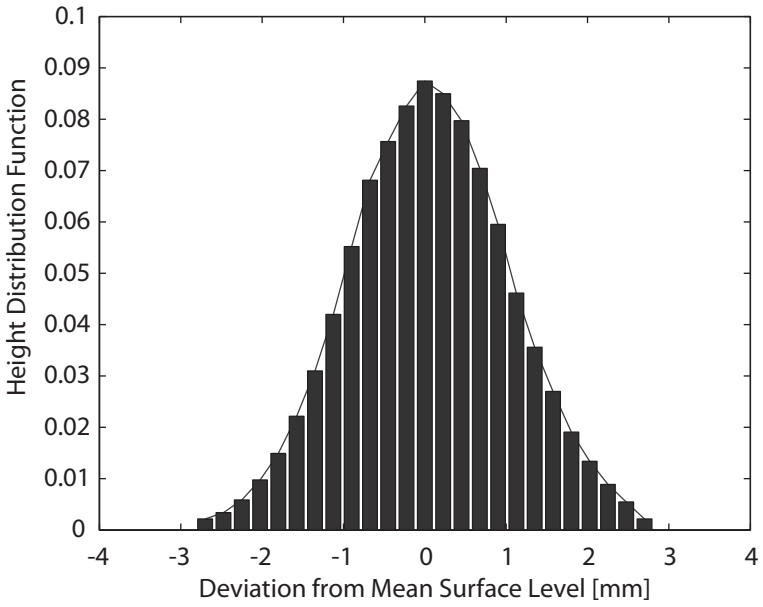

Fig. 5.5: Height Distribution Function (HDF) for rough surface simulation RS2. Bars represent the distribution of the height of surface points about the mean value of $z = 0$ in 25 bins, while the line represents the Gaussian distribution from all surface points.

varied. In creating a rough surface, we must prescribe the height deviation (σ_r) and the correlation length (L_c). While ten correlation lengths have been prescribed in some studies, acceptable results have been obtained using shorter lengths, so long as the number of realizations is sufficient. The caveat is that interactions with long wavelengths may not appear and therefore is a limitation [111].

Tab. 5.1: Rough Surface Parameters

Sim. ID	$\sigma_r[m]$	$L_c[m]$	$L[m]$	L/L_c
RS1	0.0005	0.005	0.15	30
RS2	0.0005	0.010	0.15	15
RS3	0.0005	0.015	0.15	10

Once the statistical description of the surfaces had been prescribed, GMSH [99]

was used to transform the physical description into a mesh for FVTD computations as described in Section 5.2.1. Each realization of the statistical surface had a mesh consisting entirely of 3D tetrahedral elements. The geometry of the computational domain was chosen with the x- and y-dimensions equal in size, with the value dependent upon the size of the rough surface. The z-dimension was chosen to be 2 cm in height – 1 cm of free-space above 1 cm of dielectric (which would correspond to $z_{max} = 2$ cm as shown in Fig. 5.3). We set the dimensions as $x_{max} = y_{max} = 17$ cm, and $x_{rs} = y_{rs} = 15$ cm. These x- and y-dimensions were chosen in the interest of simulating a reasonably large rough surface, but also respecting the computational time and memory requirements that the computing cluster could permit. The z-values were chosen such that there would be some space between the scattering objects (i.e. the rough surface) and the absorbing boundary conditions. We later tried increasing the space and found that the results did not change significantly, but our computation time increased.

The time function of the input waveform the derivative of a Gaussian pulse, as given in equation (4.11). The constants in equation (4.11) were chosen such that sufficient energy would propagate at the frequencies of interest (specifically, 3.5, 5.5, and 7.5 GHz).

A plane of observation points was placed above the rough surface within the free-space region of the computational domain to generate the fictitious surface upon which we compute the equivalent surface currents for the near-field to far-field transformation.

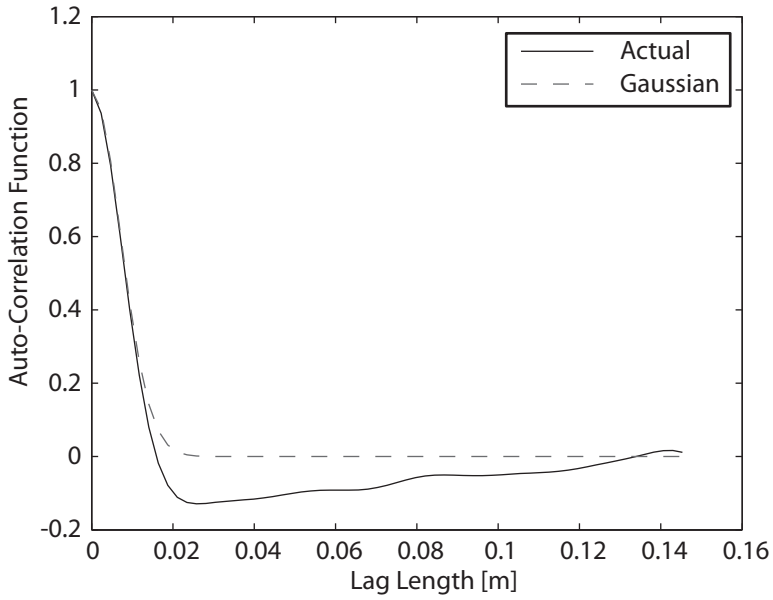

Fig. 5.6: Auto-Covariance Function (ACF) for rough surface simulation RS2. Solid line indicates actual calculated values of the lag lengths for the auto-correlation; dashed line indicates a Gaussian distribution from the σ_r and L_c values.

This is the integration surface, S. The plane was discretized with a spacing of 0.005 m, giving an array that was 31 by 31 points, or 961 points in total. The integration surface, S, was placed at a height of $z = 0.008$. Using a constant value of σ_r throughout all simulations allowed us to use the same height of observation points above the rough surface.

In order to validate our method, we compared our results with the well-known small perturbation model (SPM), originally proposed in [46]. SPM results are approximately valid when $kL_c < 3.0$ and $k\sigma_r < 0.3$, where $k = 2\pi/\lambda_0$ [112]. Table 5.2 shows values of kL_c and $k\sigma_r$ for our simulation parameters, indicating that the roughness parameters are within the range of validity for the SPM, and therefore the SPM results

can be used as a comparison for the present FVTD method.

Tab. 5.2: SPM Validity

Sim. ID	Frequency	k	kL_c	$k\sigma_r$
RS1	3.5 GHz	73.3038	0.3438	0.0718
	5.5 GHz	115.1917	0.5403	0.1128
	7.5 GHz	157.0796	0.7368	0.1538
RS2	3.5 GHz	73.3038	0.7394	0.0712
	5.5 GHz	115.1917	1.1619	0.1119
	7.5 GHz	157.0796	1.5844	0.1526
RS3	3.5 GHz	73.3038	1.0831	0.0719
	5.5 GHz	115.1917	1.7020	0.1129
	7.5 GHz	157.0796	2.3210	0.1540

Fig. 5.8 shows the final results of the simulation study for RS1 and RS3 at the frequencies of 3.5, 5.5, and 7.5 GHz in order to show the behavior as a function of frequency, as well as incidence angle. For comparison, the results of the SPM model are also plotted. Fig. 5.7 shows how the solution converges for the specific example of 5.5 GHz and an incidence angle of 30° in Simulation RS1. This type of plot is typical of the results generated for all incidence angles and for all frequencies.

In generating the results for RS1, the incidence angle was varied from 0° to 50° in 5° increments (11 incidence angles). Since the number of realizations was 20, each point on the graph is the average of 20 separate simulations, meaning that a total of $11 \times 20 = 220$ simulations were required for the FVTD results on each RS1 graph. Due to computational time limitations, for RS2 and RS3 the incidence angle was varied from 0° to 50° in 10° increments (6 incidence angles). Since the number of realizations was 20, each point on the graph is the average of 20 separate simulations,

meaning that a total of $6 \times 20 = 120$ simulations were required for the FVTD results on each RS3 graph.

To evaluate the agreement between the FVTD method and the SPM method, we use a simple visual interpretation and we also calculate an error estimate based on an L^2-norm, which is defined in equation (5.22). A summary of the calculations of an L^2-norm for each rough surface and for each frequency is given in Table 5.3. The L^2-norm is given by the following expression:

$$f(\epsilon) = \sqrt{\frac{\sum_{i=0}^{Nangles} (\sigma_i^{FVTD} - \sigma_i^{SPM})^2}{\sum_{i=0}^{Nangle} (\sigma_i^{SPM})^2}}, \tag{5.22}$$

where N_{angles} represents the number of incidence angles that were simulated (for example, $N_{angles} = 11$ for RS1), σ indicates the calculated NRCS, and the superscripts FVTD and SPM refer to the FVTD simulation and SPM calculations. A low value of $f(\epsilon)$ indicates a good agreement between the FVTD and SPM results.

Visual interpretation of the results in Fig. 5.8 shows that the poorest modeling result is for RS1 at a frequency of 3.5 GHz since the results diverge from the SPM results at higher incidence angles (about 40° and greater). The best results appear to be for RS1 at a frequency of 5.5 GHz. Evaluation of the L^2-norm gives a slightly different interpretation. According to Table 5.3, the lowest error occurs for RS1 at a frequency of 5.5 GHz. The highest error occurs for RS3 at a frequency of 7.5 GHz, yet visually, the 2^{nd} order polynomial fit seems to follow the SPM results. It would

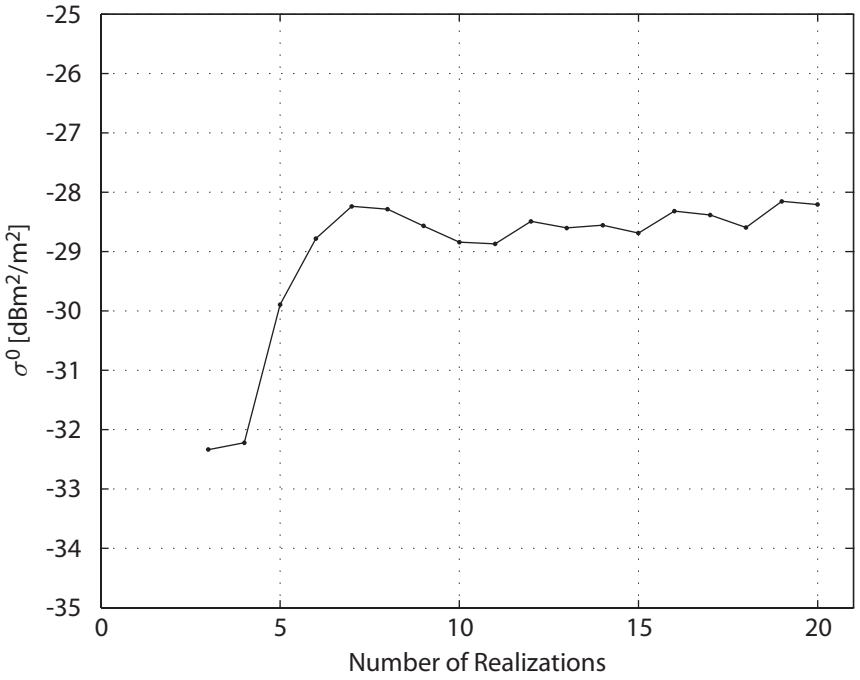

Fig. 5.7: Convergence of RS1 at 5.5 GHz. Results are shown for an incidence angle of 30°.

appear that the L^2-norm can give guidance towards which simulations are the best, but visual interpretation of the results is still necessary.

In summary, the proposed FVTD method appears to be in good agreement with the SPM model in the cases that we have tested. There is no specific limitation imposed by the FVTD method, and so, the FVTD rough surface scattering technique can be explored beyond the range of validity of SPM. This will be presented in the following chapter, where we use the proposed FVTD model for simulating scattering from a sea ice medium and compare it with experimental measurements of the NRCS.

As a test of concept, we changed the z-dimension parameters on RS1. We set $z_{max} = 2.5$ cm, with 1.25 cm of free-space above 1.25 cm of dielectric. We left

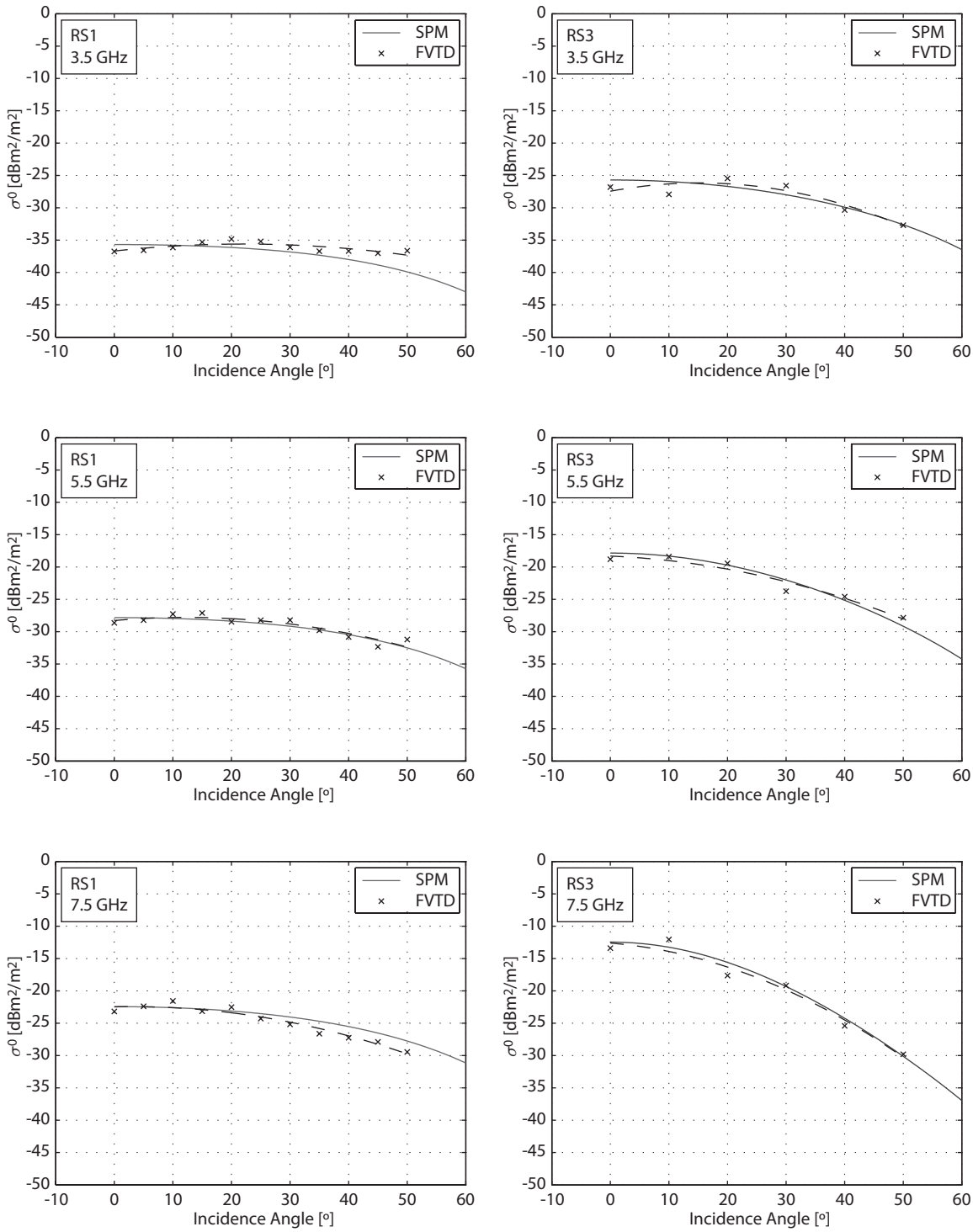

Fig. 5.8: Simulation results for RS1 ($L_c = 0.005$) and RS3 ($L_c = 0.015$). Frequencies are shown inset in the plots. Incidence angle is the monostatic transmit/receive, or backscatter, angle. A 2^{nd} order polynomial fit (dashed line) has been provided to the FVTD results to help with interpretation of the angular trend.

Tab. 5.3: Rough Surface Simulation Results

Sim. ID	Frequency	L^2-norm
RS1	3.5 GHz	0.0384
	5.5 GHz	0.0255
	7.5 GHz	0.0489
RS2	3.5 GHz	0.0478
	5.5 GHz	0.0403
	7.5 GHz	0.0456
RS3	3.5 GHz	0.0428
	5.5 GHz	0.0451
	7.5 GHz	0.0571

$x_{max} = y_{max} = 17$ cm, and $x_{rs} = y_{rs} = 15$ cm as in RS1. We created 20 new meshes with the exact same statistical description as RS1 (i.e. $\sigma_r = 0.001$ m, $L_c = 0.005$ m). Two integration surfaces, S, were placed in the domain, one at a height of $z = 0.008$ and another at a height of $z = 0.01$. Our results were only a fraction of a decibel different from the RS1 simulation. This indicates that in our RS1 simulations we had made our computational domain large enough that any reflections from the computational boundary did not impact our results. It also indicates that the height of the integration surface, S, above the rough surface was adequate since increasing the z showed an invariance of our results.

Further to this, we changed the x- and y-dimension parameters on RS3. We set the dimensions with $x_{max} = y_{max} = 0.21$ m, and $x_{rs} = y_{rs} = 0.15$ m. We centered the rough surface in the computational domain, and so, this corresponds to an increase in the spacing between the rough surface and the ABC. We left z_{max}=2 cm, as in RS1. We created 20 new meshes with the same statistical prescription as RS1 (i.e.

$\sigma_r = 0.001$ m, $L_c = 0.005$ m). The integration surface, S, was again placed at a height of $z = 0.008$ m. In comparison to our simulations of RS3, we found that there was at most a fraction of a decibel in change in the backscatter. Therefore, we conclude that our computational domain was adequate in size, and the absorbing boundary condition was placed far enough away from the scattering objects, such that there was minimal impact on the final simulation results.

As an additional test of concept, we changed the x- and y-dimension parameters on RS3. We set the dimensions with $x_{max} = y_{max} = 0.22$ m, and x_{rs}=y_{rs}=0.20 m. We left $z_{max} = 2$ cm, as in RS3. We created 20 new meshes with the same statistical prescription as RS3 (i.e. $\sigma_r = 0.001$ m, $L_c = 0.005$ m). The integration surface, S, was again placed at a height of $z = 0.008$ m. The plane was discretized with a spacing of 0.005 m, giving an array that was 41 by 41 points, or 1681 points in total. In our simulations, the incidence angle was varied from 0° to 50° in 10° increments (6 incidence angles). Simulations showed that with the larger x- and y-dimensions, our results were within about 2 dB of SPM for all frequencies tested, which is not much different from the results with the smaller x- and y-dimensions. We consider this acceptable due to the statistical nature of the problem. There are many other factors that can be investigated further here, and we therefore leave this for our suggested future work.

5.3 Dielectric Modeling

There are many challenges in modeling the dielectric properties of a medium and in Chapter 2 we suggested that we would study dielectric mixture models and discrete scatterer models for application in our simulation techniques. In fact, a common element in remote sensing studies is the approximation of a random medium as a homogeneous medium. In its simplest form, a dielectric mixture model does not take the scattering into account; however, we are planning on using the dielectric mixture models in sea ice scattering simulations.

We therefore outline our two major dielectric modeling challenges. First, we want to establish a simple method for approximating a random medium as a homogeneous medium. Second, we want to develop a method to randomly populate a volume with discrete scatterers that are representative of the inclusions that would normally be present in sea ice.

To address the first challenge, we set the goal of homogenizing a random medium, which means finding a method to replace the inhomogeneous medium with an equivalent medium consisting of a single value for the relative permittivity that is not spatially dependent. We utilize the scattered-field formulation of the FVTD method to solve for the wave propagation through a background medium that is randomly populated with spherical inclusions with a different value of permittivity. The equivalent permittivity is obtained through Monte Carlo simulations and an optimization process involving a look-up table (LUT) method. Results are compared with the theoretical Wiener bounds

and the Polder-Van Santen-de Loor (PVD) mixture model, which were presented in Chapter 2. We note that our approach is similar to that of [62]. To address the second challenge, (i.e. populating a volume with randomly located inclusions), we have implemented a Metropolis shuffle algorithm [113], which is discussed in the following subsection.

In our numerical examples we have chosen to simulate a well-studied problem, that is, the case of spheres in a host background. These initial examples were chosen to validate our method; however, there is not a strict limitation on the shape of the inclusions, so long as we follow the rules for discretization in the numerical solvers (FDTD and FVTD). Other examples could consist of hexagonal plates, spheroidal inclusions, or needle-like inclusion objects, and we leave this for future work.

Material in this section has been published by the IEEE [100] [2]

5.3.1 Random Medium Generation

There is a myriad of methods that could be used to generate a random distribution of spheres in a given volume. The volume fraction is a ratio specifying the volume which is occupied by the inclusion spheres with respect to the total volume of the computational domain. In our method we only consider hard spheres, in other words, spheres are not permitted to intersect, nor are they allowed to be in contact with each

[2] © 2010 IEEE. Reprinted, with permission, from D. Isleifson and L. Shafai, "Numerical Homogenization of Heterogeneous Media using FVTD Simulations," in Antenna Technology and Applied Electromagnetics the American Electromagnetics Conference (ANTEM-AMEREM), 2010 14th International Symposium on, 2010, pp. 1-4.

other. In order to create random distributions of spheres that do not violate the hard sphere requirement, we have chosen to employ a Metropolis shuffle algorithm [113]. We run the algorithm to create a random distribution of the spheres in space and repeat the randomization for many realizations. The Metropolis shuffle algorithm can be basically described by the following steps:

1. Initialize all spheres on a regular grid within the computational domain.

2. Generate a random movement vector for each sphere.

3. Check to see if the displacement is acceptable (i.e. no spheres intersect).

4. Repeat steps 2 and 3 for a series of passes to ensure randomness.

Fig. 5.9(a) shows the simulation space at step 1. of the Metropolis shuffle algorithm, when the spheres are initialized on a regular grid. Fig. 5.9(b) shows the simulation space after the sphere locations have been randomized using the Metropolis shuffle algorithm.

5.3.2 Plane-Wave Simulation

A plane-wave simulation method is required so that a comparison between an inhomogeneous and equivalent homogeneous medium can be performed. In order to simulate the time-domain wave propagating through free space and normally incident upon a half-space of constant dielectric, we use a 1D finite-difference time-domain (FDTD) solution [54]. A similar 1D FDTD solution for a wave propagating through

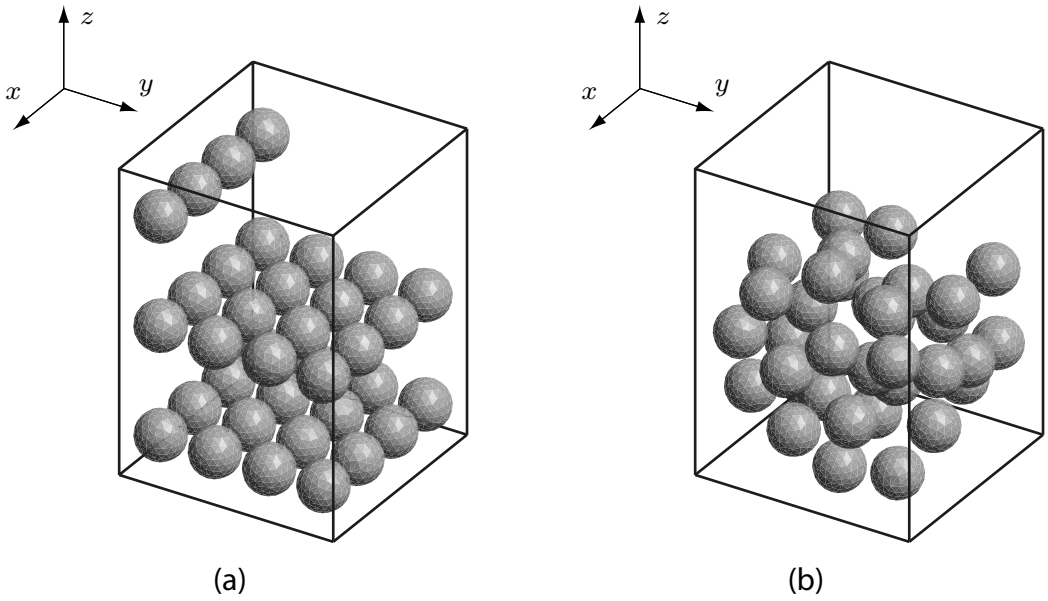

Fig. 5.9: Randomization of sphere locations for the hard sphere model.

free-space is interpolated into the FVTD computational domain, since the FVTD solution uses an irregular mesh (with tetrahedral elements). The outcome of the FVTD computation is a 3D solution to the wave propagation. The FVTD computational domain contains a random distribution of spheres with an inclusion dielectric (ϵ_i) in a free-space host background ($\epsilon_h = \epsilon_0$). Therefore the scattered-fields are a consequence of the wave interactions with the spheres and include multiple scattering effects. They can also be considered contrast sources since there is a dielectric difference between the background medium and the scattering objects.

5.3.3 Homogenization Method

Our goal is to find the solution to the half-space problem which is closest to the average wave propagation in the random media. We can then replace the random

medium with a homogeneous one that has the same propagation properties, resulting in a potential simplification of a scattering model containing inhomogeneities.

To obtain the equivalent dielectric properties of a randomized inhomogeneous medium, we must calculate the average wave propagation through a large number of random realizations and then perform a comparison with a homogeneous medium. Many realizations must be simulated to build up statistics on the random distribution of the spheres since each individual realization will result in a different result for the scattered fields, dependent upon the locations of the spheres. Through averaging a large number of simulations we can reduce the effects of fluctuations in individual realizations to build up an ensemble average.

Storing field values at all locations in the mesh is impractical, thus, we choose a series of points that are parallel to the z-axis, at the center of the computational domain as shown in Fig. 5.10. The field values are stored at each of these points for each realization, and then subsequently averaged across realizations. To summarize, we follow these basic steps:

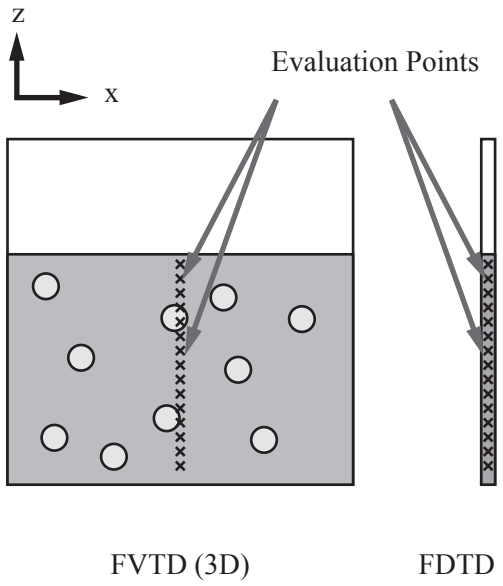

Fig. 5.10: Location of field evaluation points in the 3D FVTD mesh for comparison with the 1D FDTD simulations.

1. Generate a random realization of spheres in a dielectric background.

2. Calculate the FVTD solution to the wave propagation problem.

3. Store field values along a central beam as shown in Fig. 5.10.

4. Repeat steps 1 to 3 for many realizations.

5. Compute an ensemble average of the fields at each point.

The next step is to compare the averaged field values with an equivalent simulation of a wave incident upon a homogeneous half-space. Using a 1D FDTD simulation, a look-up table (LUT) can be generated to represent the wave incident upon a dielectric half-space. The same observation points can be used (i.e. same spatial discretization

in z), such that comparison with the FVTD solution is possible (shown in Fig. 5.10). The LUT parameters are chosen such that $\Delta\epsilon = 0.005$ [m], ranging on the dielectric values prescribed by the inclusion and host medium (i.e. $1 \leq \epsilon_h < \epsilon_i$).

For each potential solution in the LUT we minimize the L^2-norm (5.23) of the electric fields computed in the FVTD simulation (heterogeneous half-space medium) and the FDTD simulation (homogeneous half-space medium), to find the value of ϵ_{eff} that gives us the closest equivalent homogeneous substance. The L^2-norm is given by the following expression:

$$f(\epsilon_{eff}) = \sqrt{\frac{\sum_{i=0}^{Nz-1}\sum_{j=0}^{Nt-1}(E_{i,j}^{FVTD} - E_{i,j}^{LUT})^2}{\sum_{i=0}^{Nz-1}\sum_{j=0}^{Nt-1}(E_{i,j}^{FVTD})^2}}, \tag{5.23}$$

where N_z represents the number of points along the z-axis chosen to represent the medium, N_t is the total number of timesteps, and the superscripts FVTD and LUT refer to the averaged FVTD simulation and LUT simulations respectively.

5.3.4 Numerical Homogenization Results and Discussion

FVTD simulations were performed in batches on a computing cluster, while post-processing (LUT generation and evaluation) were performed on a desktop PC. The FVTD simulations were performed using a serial implementation of the algorithm, which was previously described. The computational domain was chosen as a rectangular prism, with dimensions of x = 0.05 m, y = 0.05 m, and z = 0.07 m. The domain

size was chosen in the interest of maintaining a reasonable computation time for each realization, while still providing enough room for a large number of spheres. We ran our simulations for a total of 1 ns, with an input waveform that used the time function given in equation (4.11) and used the same parameters as for the rough surface scattering examples.

We selected ten volume fractions ranging up to about 30% (corresponding to a maximum of 60 spheres), since above this value the hard sphere model limits the randomness of the medium. In other words, we found that above 30% there were basically no differences between random realizations, and so, our results would depend on the regular lattice of the initial position only. A total of 25 realizations were used to provide the statistics for each given volume fraction. Therefore, in order to calculate the equivalent dielectric as a function of volume fraction, a total of 250 simulations were required.

We chose 50 observation points located within the inhomogeneous region to provide a sampling of the wave propagation. The size of the timestep in a given realization is determined by the FVTD algorithm and is based upon the size of the elements provided by GMSH. Since the meshes were all different, the sizes of the timesteps were all different. Therefore, an interpolation scheme was required to facilitate the comparison across realizations [114]. All simulations were interpolated to a total of 5000 timesteps (i.e. $N_z = 50$, $N_t = 5000$).

All of our results are based on the calculation of two-component mixtures under a

variety of permittivity contrasts. Our simulations consisted of random realizations of a number of dielectric spheres suspended in free space (i.e. $\epsilon_h = \epsilon_0$), and with several different inclusion dielectrics (specifically, $\epsilon_i = 2$, 3, and 4).

The size of sphere was chosen with a radius of $r = \lambda_0/10$, with the wavelength corresponding to the free space wavelength at 5.5 GHz. We chose 5.5 GHz as our frequency of interest since this value corresponds to the frequency of the scatterometer, which is the frequency at which we will later compute the scattering from a sea ice medium. Additionally, we desired to observe the behavior of our method with closely positioned large scatterers, as this is where dielectric mixture models reportedly tend to break down.

The effective dielectric ϵ_{eff} calculated by the PVD model for dielectric spheres of ϵ_i in a host background medium of ϵ_h is given by equation (2.29). The theoretical bounds of the dielectric mixture are given by the so-called Wiener bounds, given by equation (2.30).

The results of our simulations with $\epsilon_i = 2$, 3, and 4 are given in Figs. 5.11, 5.12, and 5.13, respectively. We found that the FVTD simulations were consistently within the Wiener bounds, except for the values with low volume fraction (about 3%). Increasing the number of realizations (from 25 to 50) and the resolution in the LUT ($\Delta\epsilon = 0.0005$) improved upon this result since the low number of spheres permits a large variation in the positioning of the spheres. In comparison with the PVD model, we observe that the equivalent dielectric follows a similar trend. A 2^{nd} order polynomial fit was

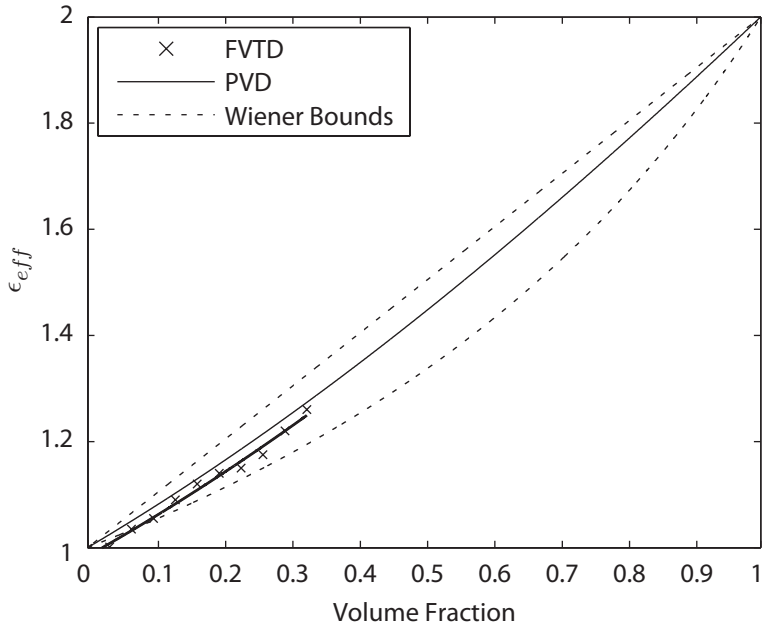

Fig. 5.11: Homogenization results for an inclusion dielectric $\epsilon_i = 2$.

provided and it appears that the FVTD results are similar to the PVD model.

5.3.5 Implications of the Homogenization Simulations

We have presented a method of homogenization of an inhomogeneous medium using the FVTD method and a Monte Carlo process. Results were compared with the theoretical Wiener bounds and the PVD dielectric mixture model and were found to be reasonable. Future work could consist of using lossy dielectric spheres and different inclusion shapes (such as spheroidal particles).

An important implication of the results presented in this sub-section is that our scattering model may not require the use of the inclusions. In other words, we have shown that for a dielectric contrast of up to four and for volume fractions up to about

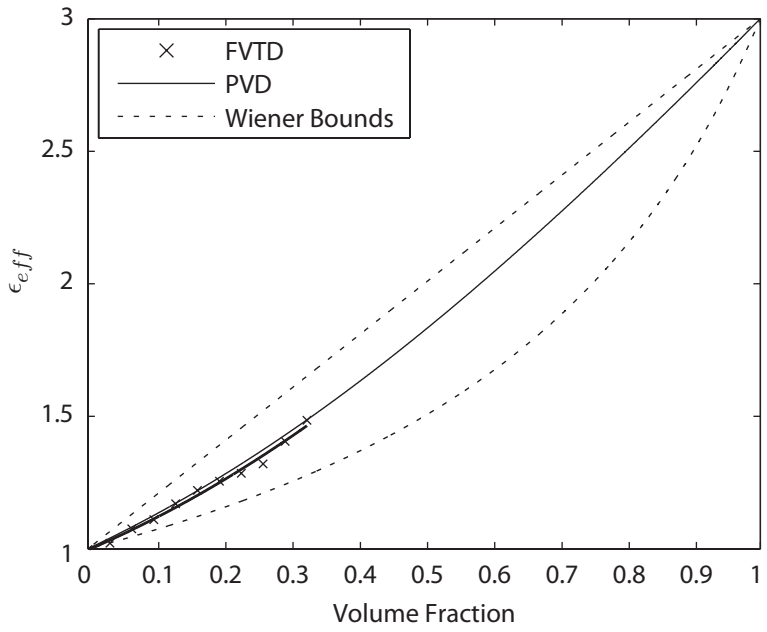

Fig. 5.12: Homogenization results for an inclusion dielectric $\epsilon_i = 3$.

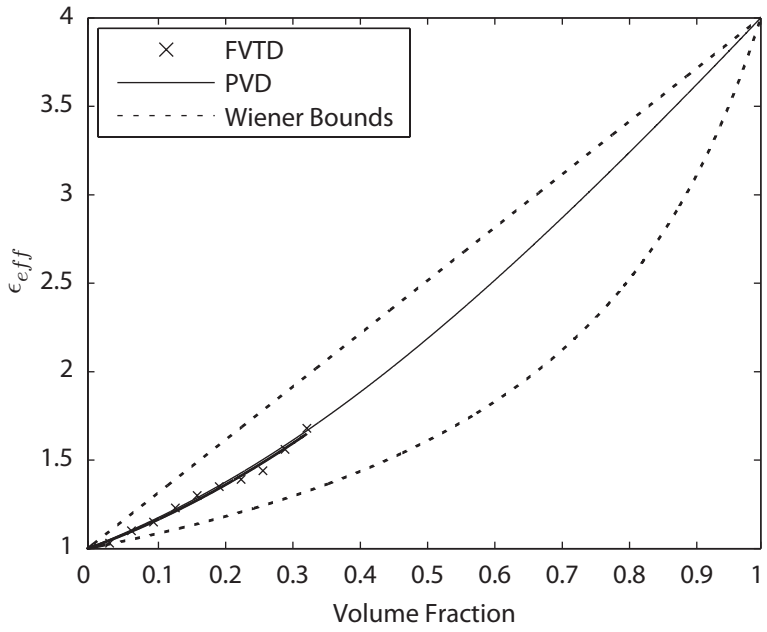

Fig. 5.13: Homogenization results for an inclusion dielectric $\epsilon_i = 4$.

30%, the dielectric mixture model can represent the overall dielectric of the medium. The importance of this result is discussed further in the following chapter where we evaluate the current model for sea ice remote sensing.

The size of the brine pockets in sea ice, combined with their high dielectric constant, is a major issue to consider when using a numerical method to model the wave interactions. More specifically, since the dielectric constant is very high, the discretization of the pocket must be very small. At the same time, the size of the pockets are quite small, so this also demands that the discretization be very fine. This is a problem because the size of the elements requires that a very large mesh must be created to represent the sea ice medium. For example, if we have a discretization of $\Delta z = 0.00125$ [m], and the domain size is $5\lambda \times 5\lambda \times 3\lambda$, then we have 400 billion elements. Even if we have a computing cluster at our disposal, the memory requirements are too immense and the brute force method of refining the mesh is not feasible.

As previously stated, our initial examples were chosen to validate our homogenization method (and are not an attempt to compete with the PVD model). With the method validated, the next step would be to consider cases where the PVD model is not readily applicable, or where the inclusion shape does not permit an analytic solution for the polarization of the inhomogeneity (for example, a dendritic snowflake shape). In these cases, the numerical solution provided by the FVTD method would prove to be beneficial.

5.4 Chapter Conclusions and Discussion

In this chapter we have presented simulation techniques that utilize Monte Carlo methods for dielectric and scattering models in remote sensing. All of our simulation techniques rely upon the FVTD computational engine and the FDTD incident-field that were discussed in the previous chapter. We have presented the necessary components of the scattering model and discussed the statistical aspects of the method. We developed a technique that can be used for rough surface scattering and validated it by comparing with the small perturbation model (SPM). We also developed a technique for homogenizing an inhomogeneous medium, focusing particularly on the validation of our method, rather than attempting to compete with the PVD method. An important implication of the homogenization method was that the simulation of discrete scatterers is not necessarily required, given the size of the inclusions (on the order of millimeters) and the frequency of interest (5.5 GHz).

The following chapter provides a culmination of all of our research through connecting the modeling techniques developed with geophysical measurements and associated scatterometer measurements.

6. APPLICATION OF THE FVTD MODEL FOR REMOTE SENSING OF SEA ICE

In this chapter we combine our physical measurements of sea ice with dielectric modeling techniques, and utilize them in the FVTD remote sensing scattering model that we have developed. Several examples are given to show the applicability of the model and we give some discussion regarding the modeling issues that we have discovered. The goal of this chapter is to show how our modeling technique can provide good agreement with field results for a variety of physical situations.

6.1 A Monte Carlo Method for Simulating Scattering from Sea Ice using FVTD

In Chapter 5, we presented Monte Carlo methods for simulating rough surface scattering and propagation through inhomogeneous media. These methods were based on a numerical simulation technique using the FVTD method as the computational engine. The next step is to use sea ice dielectric values in the Monte Carlo simulation method. We can convert the measured physical parameters, such as the temperature

and salinities, into a complex permittivity for use in the FVTD model, as discussed in Chapter 2. Once the dielectric values have been prescribed, we can perform a Monte Carlo simulation of the medium in order to obtain the scattering properties of the simulated sea ice medium. The general steps for the modeling process are summarized as follows:

1. Convert measured physical variables to estimates of dielectric constants of the medium using dielectric models
2. Use a rough surface generator to create random realizations of the rough surface
3. Create a geometry file as input to the meshing program
4. Generate and optimize the mesh
5. Run simulations and perform Monte Carlo averaging of the results
6. Compare with the experimentally measured NRCS

This is an iterative process, since it is unlikely that we will be able to precisely match the experimentally measured results with the simulation results on the first pass. In the following case studies we present some of the issues and variations that arose when trying to model sea ice.

For reference, Table 6.1 provides a list of input parameters, the associated model parameter, and a reference for the modeling input parameter.

Tab. 6.1: Model Input Parameters and Corresponding References

Input Parameter	Model Parameter	Reference
f, T_{ice}	ϵ_{ice}	Mätzler *et al.* [32]
f, T_{ice}	ϵ_{brine}	Stogryn and Desargent [33]
T_{ice}, S_{ice}	v_b	Frankenstein and Garner [11]
$v_b, \epsilon_{ice}, \epsilon_{brine}$	ϵ_{seaice}	Ulaby *et al.* [31]
$f, T_{seawater}, S_{seawater}$	$\epsilon_{seawater}$	Klein and Swift [115]
Thickness	d_{ice}	Isleifson *et al.* [65]

6.2 Discussion of Dielectric Models

From our previous studies on the dielectric properties of mixtures (in Chapter 5) we found that populating a volume with dielectric spheres resulted in good agreement with the PVD models for a decently large range of dielectric contrasts and volume fractions. The size of the inclusions and the size of the computational domain were made such that the method was numerically feasible and tractable.

For modeling brine inclusions in sea ice, the initial naïve approach would be to model the actual physical inclusions within the sea ice volume using the FVTD method. This would entail modeling a pure ice background populated with dielectric inclusions that represent the brine pockets. While this would provide the most realistic situation from a physical standpoint, from an electromagnetic (and equally importantly, computational electromagnetic) perspective, this is inefficient. The brine pockets have a high dielectric constant and they are very small in comparison to wavelength in the microwave regime. Therefore, modeling the dielectric inclusions using their true size within the FVTD mesh makes the computation inefficient. The size of the inclusions is typically on the order of 1 mm (as discussed in Chapter 2). Therefore,

at microwave frequencies we would require such a fine discretization of our mesh that our computation would be so memory-intensive, and the computational time so exhaustive, that it would be rendered useless from a practical perspective.

One approach that we had considered was making the dielectric inclusions larger by somehow taking an average dielectric constant of the inclusion and the surrounding fresh ice. This method was appealing in that the shape of the inclusions could be preserved (i.e. simply using a larger sphere with a higher dielectric constant than the surrounding medium would provide an effective scattering center). While it seems that conceptually this idea would work, we found that the method does not provide a usable result. This fact is summarized succinctly in the following quote by Bohren, regarding the average dielectric function of an inhomogeneous particle:

> But we would not be tempted to recast the problem of scattering by a coated sphere in the form of scattering by an equivalent homogeneous sphere with an average, or effective, dielectric function obtained by combining somehow the dielectric functions of core and coating. For although our prescription might give good results for one size at a particular wavelength, it would not do so for other sizes and wavelengths; we would be faced with the task of continuously modifying the prescription to force the scattering and absorbing properties of the equivalent homogeneous particle into congruence with those of the inhomogeneous particle. Clearly, therefore, some kind of statistical irregularity on an appropriate scale is a

> necessary concomitant of a well-defined average dielectric function of an inhomogeneous medium. [116]

In spite of this warning, we still tested the idea of using the average dielectric properties as a scattering center, since other researchers had tried it as well. For example, Nassar [47] attempted to use a similar concept to add some volume scattering properties in his FDTD studies of scattering from sea ice. We were not able to recreate a similar result, and in fact, we found that using the equivalent homogeneous spheres resulted in a large backscatter increase. This did not match our measurements, nor did it behave in a way that we had anticipated. We therefore abandoned this approach and proceeded to work with dielectric mixture models as others have done in the past (Fung presented similar simplifications [40], and alternatively, Chanal *et al.* [62] presented homogenization methods for multiple species of scatterers).

6.3 Simulations and Comparison with Radar Data

We have collected a large series of scatterometer measurements, along with coincident geophysical measurements, during the CFL and ArcticNet projects. In this section, we present the results of a series of modeling case studies that were conducted to evaluate the applicability of the proposed Monte Carlo method for simulating scattering from sea ice using FVTD. We chose three case studies that were relatively similar (in terms of sea ice physics) to provide an area of confidence in the developed method. The examples were all newly-formed sea ice, which is of significant interest to the Arctic

research community, as discussed in the introduction of Chapter 3.

We presented a Monte Carlo method for simulating scattering from a rough surface in Chapter 5. We now apply this technique in the modeling of the scattering from sea ice. Inherent with any statistical technique is the error associated with a finite number of realizations. In our work, we have decided to use up to 24 different realizations to represent the sea ice medium. We chose a maximum of 24 realizations as a compromise between running a prohibitively large number of simulations and having some statistical significance. We know that a larger number of realizations would provide a lower error; moreover, the convergence of the results shows when the obtained values are adequate for the purposes of our modeling.

Ideally, we would have liked to simulate a region that was the same size as the scatterometer footprint to represent the rough surface. However, due to limitations in the numerical method, it was impossible to simulate a region that was greater than several wavelengths in the x- and y-dimensions (for f = 5.5 GHz, $\lambda_0 = 5.4545$ cm). In order to overcome this problem, we created a large number of smaller realizations that represented the sea ice medium in a Monte Carlo modeling study of the scattering properties. The scattering from one simulation of the sea ice medium provided a single sample of the scattering characteristics of this highly inhomogeneous medium.

In this modeling study, we made the assumption that all of the significant scattering interactions would take place at the surface of the sea ice, since newly-formed sea ice is generally a highly lossy dielectric material at microwave frequencies. We relied

on literature values of surface roughness parameters for sea ice since we were not able to consistently and accurately measure the surface roughness in our fieldwork. Example literature values are given in Table 6.2 to provide a relative range of sea ice surface roughness parameters. Generally, we expect that the height variation, σ_r, should be on the order of millimeters, whereas the correlation length, L_c, should be on the order of centimeters. Note that in Table 6.2 the acronym CRREL(EX) refers to experimental work performed at the US Army Corps of Engineers Cold Regions Research and Engineering Laboratory.

Tab. 6.2: Literature Values for Sea Ice Surface Roughness Parameters.

σ_r[m]	L_c[m]	Reference
0.0002-0.0048	0.00669-0.0177	CRREL'88 [40]
0.00216	0.0047	CRRELEX'90 [117]
0.00136	0.0176	CRRELEX'90 [117]
0.0005	0.0175	CRREL'94 [47]
0.0019	0.008	CRREL'94 [47]

Estimations of dielectric properties of the sea ice medium were obtained through well-established dielectric modeling techniques. The models we used are summarized in Table 6.1, where we provide a list of input parameters, the associated model parameter, and a literature reference. Details of the usage of the models is given in each of our case studies. In our case studies, simulations were conducted only for the TE case, that is, a horizontally-polarized incident-field. From our simulations we obtain both the co-polarized return σ^0_{HH} and the cross-polarized return σ^0_{VH}. Future work could entail TM simulations to calculate σ^0_{VV}.

Since we did not have actual measurements of the surface roughness parameters,

we used SPM to give us an initial guess for L_c and σ_r. We performed a series of simulations varying the surface roughness parameters and found values that provided good agreement between simulated and measured NRCS in a manual optimization problem. We constrained our optimization problem by assuring that our surface roughness parameters were within the range of literature data (see Table 6.2).

6.3.1 Case Study I: CFL Station 1800C

We utilized the data collected at CFL Station 1800C as our first example of sea ice remote sensing. CFL Station 1800C was newly-formed nilas that was 5.5 cm in thickness. From the microstructural analysis (not presented here, but performed in a parallel ice physics study), it appeared to have formed under quiescent conditions. Physical measurements of the sea ice were conducted as described in the methods of Chapter 3 and these data provide the baseline input for both our dielectric and scattering models. The relevant details of the physical and electrical data for this measurement location are summarized in Table 6.3. The mean ice temperature was calculated by averaging the ice surface and ice-water interface temperatures. The *in situ* temperature and laboratory calculated salinity were used to calculate brine volume according to Frankenstein and Garner [11]. The brine volume fraction and *in situ* temperature were then used to calculate both the dielectric constant of the brine using the equations derived by Stogryn and Desargent in [33] and the dielectric constant of the ice using the expressions given by Mätzler et al. [32]. Finally, an

estimate of the dielectric mixture was obtained using the PVD model assuming spherical brine pockets (equation 2.29).

Tab. 6.3: Physical Parameters and Evaluated Dielectric Values for CFL Station 1800C

Physical Parameters	Thickness	d_{ice} = 5.5 cm
	Ice Surface Temperature	T_{si} = -8.74°C
	Mean Ice Temperature	T_{msi} = -5.21°C
	Ice Bottom Temperature	T_{iw} = -1.68°C
	Bulk Ice Salinity	S_b = 11.8 PSU
	Brine Volume Fraction	v_b = 11.5%
Dielectric Values	Brine Dielectric	$\epsilon_{brine} = 50.0011 + j43.6265$
	Pure Ice Dielectric	$\epsilon_{ice} = 3.1837 + j0.0010$
	Sea Ice Dielectric	$\epsilon_{seaice} = 4.5241 + j0.2118$
	Sea Ice Conductivity	$\sigma_{seaice} = 0.06480$

With the dielectric properties of the medium defined, the FVTD modeling domain was created next. The input parameters and some of the details on the computational domain are summarized in Table 6.4. We set the dimensions as $x_{max} = y_{max} = 17$ cm, and $x_{rs} = y_{rs} = 15$ cm, similar to the rough surface parametric tests performed in Chapter 5. The geometry of the FVTD computational domain is shown in Fig. 6.1.

The results of our simulations for σ^0_{HH} are presented in Fig. 6.2 and are compared

Tab. 6.4: FVTD Simulation Parameters for CFL Station 1800C

Modeling Domain Parameters	$x_{max} = y_{max} = 0.17$ [m]
	$x_{rs} = y_{rs} = 0.15$ [m]
	z-dimension = 0.0325 [m]
	# of elements = 1.75 million
Rough Surface Parameters	σ_r= 0.00062
	L_c= 0.015

with the scatterometer measurements. We have plotted the mean measured scatterometer results with the error bars showing the maximum and minimum measurement values of each scan. Our FVTD simulation results follow the trend of the scatterometer data reasonably well. At the incidence angles of 55° and 60°, the scatterometer measurements appear to saturate, that is, they appear to reach a minimum value and do not decrease with increasing incidence angle. One possible explanation could be that there is a volumetric scattering aspect that is evident at these incidence angles, whereas it is not as dominant at the lower incidence angles. Our FVTD simulations do not attempt to add a volumetric scattering element, and so, they continue to decrease with increasing incidence angle. Additionally, the effects of noise on the NRCS measured by the scatterometer could also be a source of error, in spite of our best efforts to ensure that the radar processing algorithm minimized its effects. The FVTD cross-polarized simulation results (σ^0_{VH}) are <-50 dB (below the scatterometer noise floor), and are much lower than the scatterometer measurements. We conclude that our FVTD simulations have provided a good comparison with the scatterometer measurements for the co-polarized signal (σ^0_{HH}); however, the FVTD results have not replicated the results of the cross-polarized signal (σ^0_{VH}). In order to match the cross-polarized signal, we hypothesize that we would have to include some form of anisotropy for the sea ice dielectrics and/or the rough surfaces. The current implementation of the FVTD engine supports only isotropic media. As part of our future research, we could consider adding the capability for simulating anisotropic dielectric

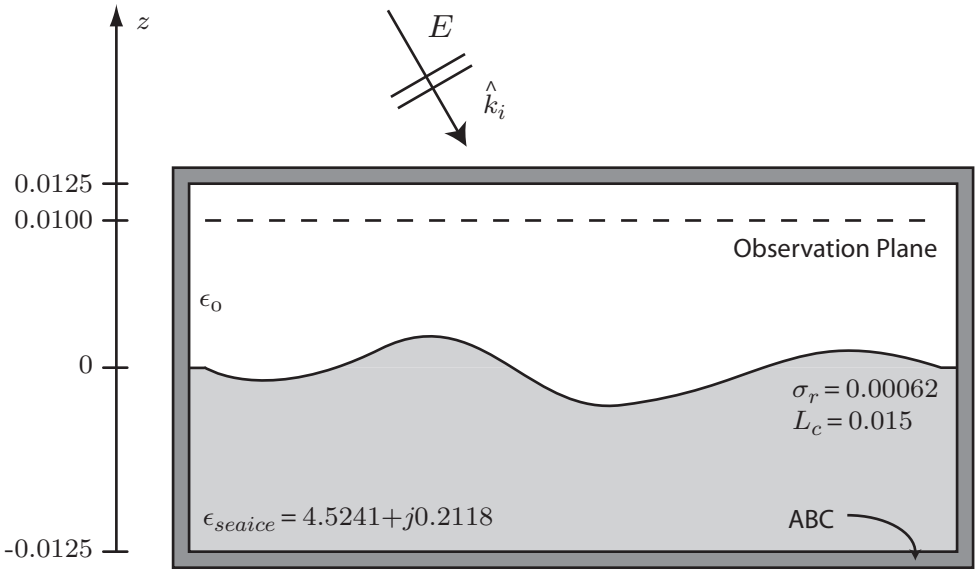

Fig. 6.1: A 2D Slice of the FVTD Computational Geometry for CFL Station 1800C.

media in the FVTD engine in order to see its effects. Additionally, we could also consider using different surface roughness parameterizations. In all of our examples, we make the assumption that the rough surface follows a statistical distribution that is independent of direction. Although the sea ice in our parametric studies appeared to have grown under quiescent conditions, environmental effects (wind direction, wave action) could potentially impact the surface. By adding anisotropic capabilities, we could improve upon our physical description of the sea ice in the model, and likely improve the match between our simulated and measured cross-polarized signals.

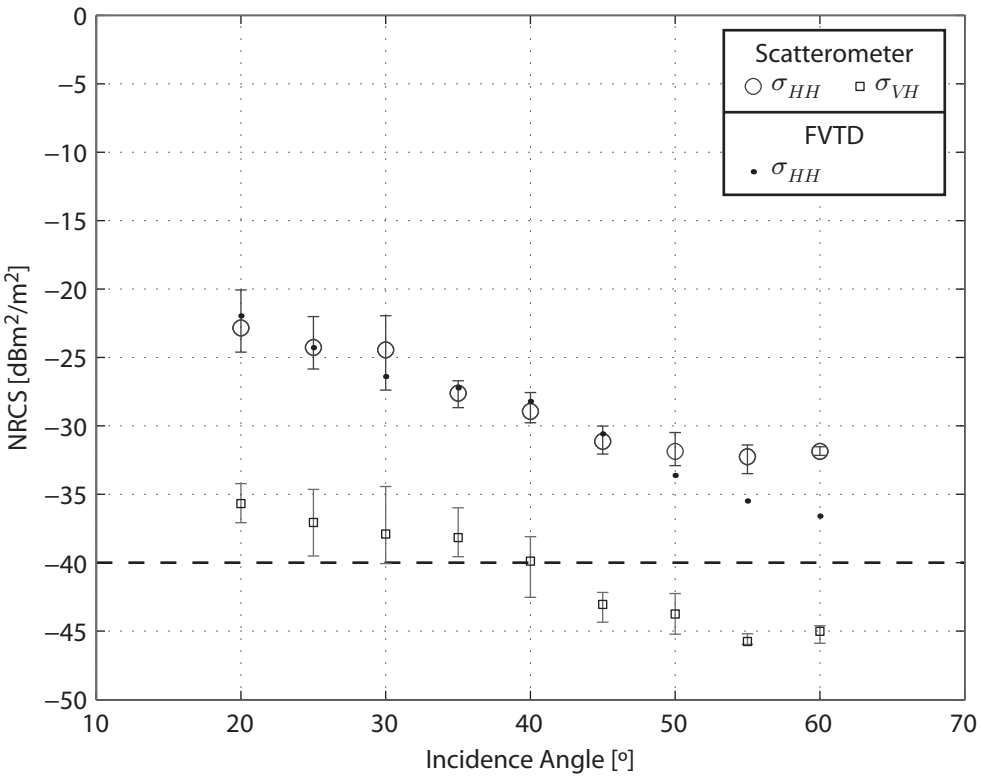

Fig. 6.2: Comparison of FVTD simulation results and scatterometer measurements at CFL Station 1800C. The dashed line at -40 dB represents the estimated noise floor of the scatterometer.

6.3.2 Case Study II: CFL Station 1800B

We utilized the data collected at CFL Station 1800B as our second example of sea ice remote sensing. CFL Station 1800B was light nilas that was 9 cm in thickness. There were a few small frost flowers (<1 cm) that populated the surface and we estimated the percentage coverage as a maximum of 25%. We considered the frost flowers as a roughening of the surface, and so, the roughness parameters of this station are greater than that of Case Study I: CFL Station 1800C. The details of the physical and electrical data for this measurement location are summarized in Table 6.5.

With the dielectric properties of the medium defined, the FVTD modeling domain was created next. The input parameters and some of the details on the computational domain are summarized in Table 6.6. In Table 6.6 the total z-dimension is a summation of the modeled sea ice layer and an overlying free-space layer. Again, we began the modeling process by considering the scatterometer measurements of the ice to be dominated by surface scattering. By varying the parameters of the surface roughness characterization, we found that we could match the scatterometer measurements almost perfectly with a surface roughness characterization that was within an acceptable range for newly-formed sea ice (see Table 6.2). The geometry of the FVTD computational domain is shown in Fig. 6.3.

Although the thickness of the sea ice is 9 cm, we only modeled the top portion of the sea ice for three reasons. First, the exploration depth of the interrogating EM wave (using ϵ_{seaice}) is smaller than the complete ice thickness, so the bottom

Tab. 6.5: Physical Parameters and Evaluated Dielectric Values for CFL Station 1800B

Physical Parameters	Thickness	d_{ice} = 9 cm
	Ice Surface Temperature	T_{si} = -10.7°C
	Mean Ice Temperature	T_{msi} = -6.21°C
	Bulk Ice Salinity	S_b = 13.7 PSU
	Brine Volume Fraction	v_b = 11.4%
Dielectric Values	Brine Dielectric	$\epsilon_{brine} = 47.9030 + j44.0821$
	Pure Ice Dielectric	$\epsilon_{ice} = 3.1827 + j0.0010$
	Sea Ice Dielectric	$\epsilon_{seaice} = 4.5056 + j0.2183$
	Sea Ice Conductivity	$\sigma_{seaice} = 0.0668$

interface would play a minor role in the backscattering simulation. In other words, we hypothesize that this highly saline ice would present a predominantly surface scattering situation. Second, it would take considerably more time to simulate a larger domain using our present method. Since the expected contribution from the ice-water interface is very small, it is inefficient to simulate the complete ice thickness. Third, we are approximating the sea ice as a homogeneous slab of constant dielectric, so the absorbing boundary conditions should effectively terminate the wave propagation with minimal reflection back into the solution domain. From a computational perspective,

Tab. 6.6: FVTD Simulation Parameters for CFL Station 1800B

Modeling Domain Parameters	x-dimension = 0.17 [m]
	y-dimension = 0.17 [m]
	z-dimension = 0.035 [m]
	# of elements = 1.7 million
Rough Surface Parameters	σ_r= 0.003027
	L_c= 0.018056

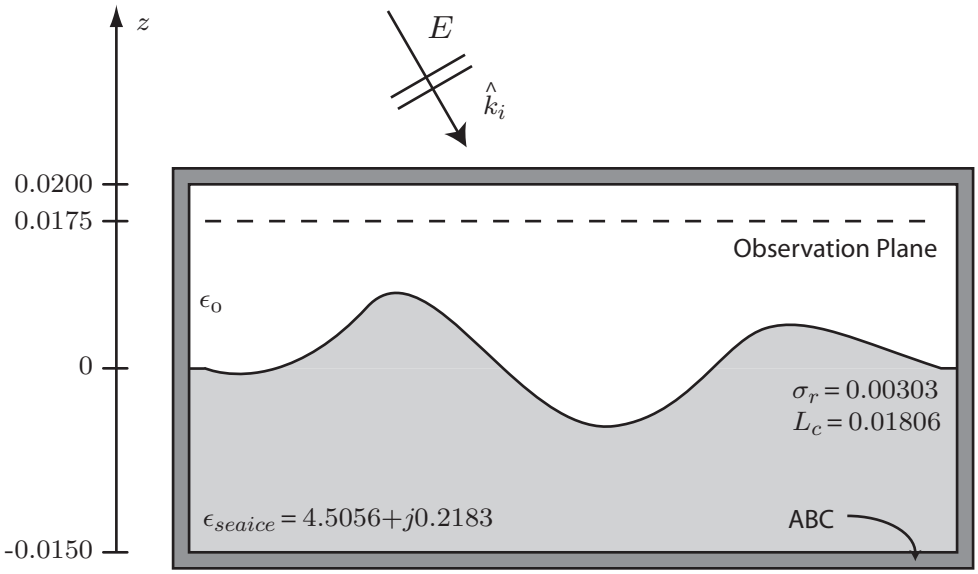

Fig. 6.3: A 2D Slice of the FVTD Computational Geometry for CFL Station 1800B.

the sea ice appears to continue to negative infinity in the z-direction, and so, there would be no difference in simulating thicker sea ice (unless, of course, we went as far as to include the ice-water interface). Therefore, we only modeled the top 2 cm of the sea ice.

The results of our simulations for σ^0_{HH} and σ^0_{VH} are presented in Fig. 6.4 and are compared with the scatterometer measurements. We have plotted the mean measured scatterometer results with the error bars showing the maximum and minimum measurement values of each scan. Our FVTD simulation results follow the trend of the scatterometer data reasonably well for σ^0_{HH}; however, the FVTD simulations have not replicated the results of the cross-polarized signal (σ^0_{VH}). This is likely due to limitations in the computational method, more specifically, we have assumed that

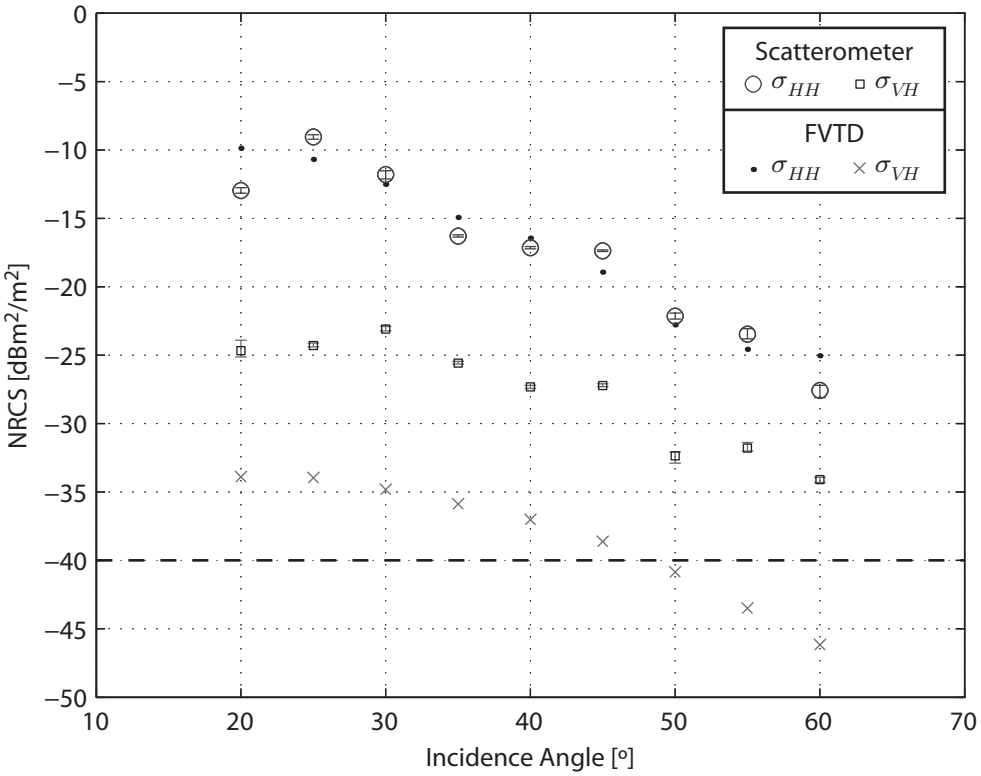

Fig. 6.4: Comparison of FVTD simulation results and scatterometer measurements at CFL Station 1800B. The dashed line at -40 dB represents the estimated noise floor of the scatterometer.

the dielectric medium is completely isotropic and the rough surface is isotropic. It is not surprising that the simulated cross-polarized signal is lower than the measured cross-polarized signal since we have not taken all of the depolarizing factors into account in our model.

6.3.3 Case Study III: CFL Station D28A

We utilized the data collected at CFL Station D28A as our third example of sea ice remote sensing. CFL Station D28A was newly-formed lead ice with a thickness of 9 cm. The details of the physical and electrical data for this measurement location are summarized in Table 6.7. This station was different from the previous two examples particularly because it had a slushy layer that was around 1 [mm] in depth on the surface. In our modeling, we followed the approach of Nghiem et al [85] who estimated that the slushy layer was 25% brine and 75% ice in a similar situation. We estimated the dielectric of this slushy layer by using the PVD model, under the assumption that the layer was a two-phase mixture of brine and ice, where the brine could be represented by spherical pockets.

With the dielectric properties of the medium defined, the FVTD modeling domain was created next. The input parameters and some of the details on the computational domain are summarized in Table 6.8. Again, we began the modeling process by considering the scatterometer measurements of the sea ice to be dominated by surface scattering. By varying the parameters of the surface roughness characterization, we found that we could match the scatterometer measurements almost perfectly by the correct choice. The values selected for the surface roughness characterization were within an acceptable range of literature values. The geometry of the FVTD computational domain is shown in Fig. 6.5. The computational domain of CFL Station D28A consists of three layers (air, slush, and sea ice), as opposed to the previous two case

Tab. 6.7: Physical Parameters and Evaluated Dielectric Values for CFL Station D28A

Physical Parameters	Thickness	d_{ice} = 9 cm
	Ice Surface Temperature	T_{si} = -12.6°C
	Mean Ice Temperature	T_{msi} = -10.455°C
	Bulk Ice Salinity	S_b = 17.1 PSU
	Brine Volume Fraction	v_b = 9.2%
	Ice Surface Salinity	S_{si} = 82.0 PSU
	Slush Thickness	1 mm
Dielectric Values (Slushy Layer)	Brine Dielectric	$\epsilon_{brine} = 37.5798 + j42.5864$
	Pure Ice Dielectric	$\epsilon_{ice} = 3.1769 + j0.0010$
	Slush Dielectric	$\epsilon_{slush} = 7.2173 + j1.7059$
	Sea Ice Conductivity	$\sigma_{slush} = 0.52196$
Dielectric Values (Sea Ice Layer)	Brine Dielectric	$\epsilon_{brine} = 40.5769 + j43.7644$
	Pure Ice Dielectric	$\epsilon_{ice} = 3.1789 + j0.0010$
	Sea Ice Dielectric	$\epsilon_{seaice} = 4.1711 + j0.1726$
	Sea Ice Conductivity	$\sigma_{seaice} = 0.052811$

studies, which consisted of two layers (air and sea ice).

The results of our simulations for σ^0_{HH} are presented in Fig. 6.6 and were compared with the scatterometer measurements, and the SPM. We have plotted the mean measured scatterometer results with the error bars showing the maximum and minimum measurement values of each scan. Our FVTD simulation results follow the trend of the scatterometer data reasonably well. We conclude that our FVTD simulations have provided a good comparison with the scatterometer measurements for the co-polarized signal (σ^0_{HH}); however, the FVTD simulations have not replicated the results of the cross-polarized signal (σ^0_{VH}). Again, this is likely due to limitations in the computational method, where we have assumed that the dielectric medium is completely isotropic and the rough surface is isotropic. By adding more of the depolarizing

Tab. 6.8: FVTD Simulation Parameters for CFL Station D28A

Modeling Domain Parameters	x-dimension = 0.17 [m] y-dimension = 0.17 [m] z-dimension = 0.0325 [m] # of elements = 2.3 million
Rough Surface Parameters	σ_r= 0.00152649 L_c= 0.0140625

features into our model, we hypothesize that we could improve the agreement between the simulated and measured cross-polarized signals.

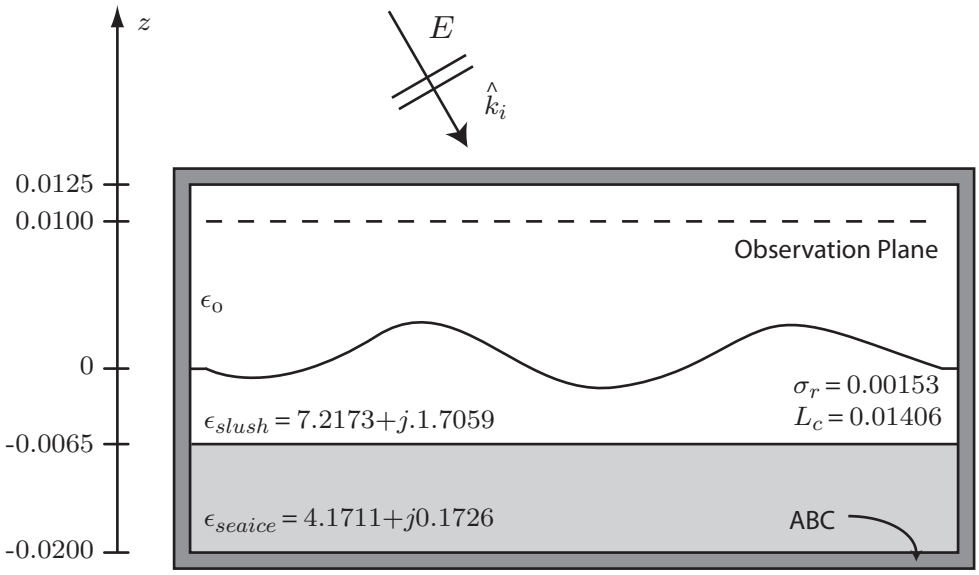

Fig. 6.5: A 2D Slice of the FVTD Computational Geometry for CFL Station D28A.

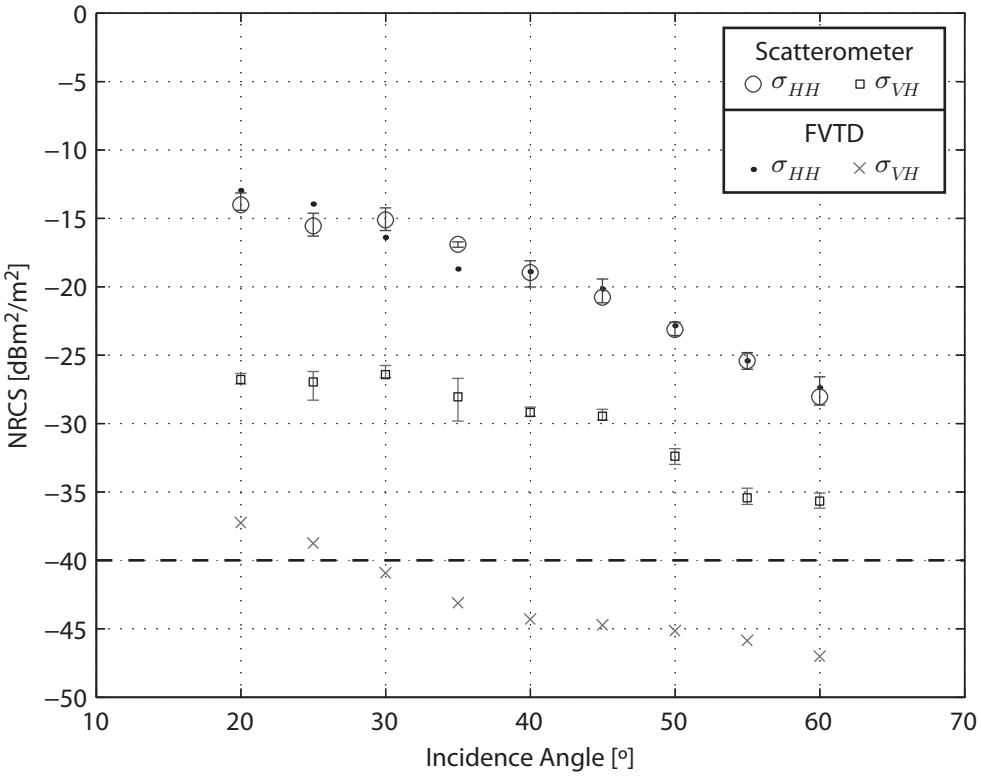

Fig. 6.6: Comparison of FVTD simulation results and scatterometer measurements at CFL Station D28A. The dashed line at -40 dB represents the estimated noise floor of the scatterometer.

6.4 Chapter Conclusions and Discussion

This chapter has combined the physical measurements of sea ice with dielectric modeling techniques for use in the FVTD remote sensing scattering model that we have developed. Several examples were given to show the applicability of the model and we gave some discussion regarding the modeling issues that we have discovered. We have shown how our modeling technique can provide good agreement with field results for a variety of physical situations, even with approximations and estimations on the dielectric values and roughness scales. We have shown that the surface roughness

parameters are a critical measurement, since we were able to achieve a reasonable match between simulated and measured results through a manual optimization of the roughness parameters. It is clear that the modeling method does not take all necessary aspects into account, since the measured and simulated cross-polarized signal were not in good agreement and we were not able to simultaneously match both σ^0_{HH} and σ^0_{VH}.

This series of simulation case studies has shown that significant challenges still remain in modeling the scattering from sea ice. We had to make several assumptions and approximations to arrive at the final scattering model. As an example, we had to assume that there was no variation in the temperature of the sea ice in the horizontal direction (recall the assumption of a z-stratified medium), but in Chapter 3, we showed that the temperature could significantly impact the scatterometer measurements for both co-polarized and cross-polarized signals.

When modeling CFL Station 1800B, we considered it to be a lossy dielectric half-space with a rough surface that followed Gaussian statistics. We did not specifically account for the effects of the presence of individual frost flowers. It is conceivable that the frost flowers could account for part of the cross-polarized signal, and since we did not account for them in the model, their contribution is not present. A future model could consider adding frost flowers, which is entirely feasible in the FVTD model. The challenges, which are quite formidable, would be to determine the dielectric properties of the frost flowers and to ensure that a proper statistical description (such as distribution, percentage surface coverage, size, orientation) would be used.

Although we have not attempted to model multiyear sea ice (MYI) in this thesis, future work could be conducted in this area. MYI is brine-poor, meaning that it is electrically similar to fresh ice. The inclusions in MYI are typically air pockets that are appreciable in size with respect to the incident wavelength at our frequency of 5.5 GHz. A generally accepted assumption is that scattering from air bubbles is important at frequencies above 2-3 GHz [7]. In contrast to newly-formed sea ice, where the brine pockets are very small and have a high dielectric constant, the inclusions in MYI are comparatively larger and have a dielectric constant equal to that of free-space (i.e. ϵ_0). In FVTD, a computational mesh containing the large air pocket inclusions of MYI would likely be feasible for simulation studies for several reasons. First, the size of the mesh elements would not be intolerably small due to the physically small size of the inclusions (as was the case for newly-formed sea ice). Second, a mixture model technique to find the average effect of the inclusions is not necessary since we could mesh the true dimensions of the inclusions (without decreasing the mesh element size to be intolerably small). Furthermore, assuming that we have properly discretized the computational domain for the ice dielectric, then the discretization of the inclusions is already adequate for computational stability. This is the exact opposite of brine pockets, where the higher dielectric constant actually requires a finer discretization.

Another important application of our modeling technique could be in estimating the dielectric constant of the upper layer of the sea ice. If we could measure the surface roughness of the sea ice using another remote sensing instrument (for example,

a Lidar), then we could calculate the statistical roughness parameters (σ_r and L_c) to a reasonable tolerance. If we prescribed the statistical roughness parameters in the FVTD scattering model, then we could perform a parametric study in which we varied the dielectric constant of the sea ice. An optimization process, which would involve matching the simulated and measured σ^0_{HH}, could be used to estimate the dielectric constant. The problem could be further constrained by including physical variables (for example, the air temperature, or the surface temperature as measured by a infrared transducer pointing at the surface of the sea ice). As discussed throughout this thesis, the temperature and salinity govern the dielectric constant, and so, remotely sensing the dielectric constant could provide a method to estimate some of the thermodynamic variables of interest. Of course, this is an inverse problem, and so, due care to ensure the uniqueness and stability of the solution would be required.

At this point, we consider our preliminary modeling study to be complete. Our methods and techniques have opened up many different areas that we would consider to be important areas of research. The final chapter of our thesis will summarize our findings and provides some direction for future work that we believe has merit in completing at some point in the future.

7. CONCLUSIONS AND FUTURE WORK

This dissertation has presented new experimental results and modeling techniques that are applicable for microwave remote sensing of sea ice. In our introduction, we presented a series of objectives with the overarching goal of developing a novel modeling technique that integrates *in situ* field data and provides a simulation tool to predict the polarimetric radar signatures of sea ice. We have succeeded at each of these objectives and also in our overarching objective.

7.1 Contributions to Research

The contributions of this dissertation can be divided into three major areas:

1. The collection, analysis, and interpretation of experimentally obtained sea ice remote sensing and associated geophysical ground truth data,

2. The creation of appropriate electromagnetic modeling tools for conducting simulations of sea ice by modifying and using an existing FVTD computational electromagnetics tool,

3. The application of the developed FVTD Monte Carlo Method for simulating

the backscattering from newly-formed sea ice and the subsequent comparison with experimentally measured backscattering.

On the experimental side, we have contributed towards a large database of scatterometer measurements and associated geophysical measurements. These data were collected from a time-period which includes the conditions present from before the fall freeze-up to just before the spring melt season, and cover a wide variety of sea ice types under a wide variety of thermodynamic states. Amongst other future uses, these data are being used by the European Space Agency (ESA) to create a database for which to base future satellite missions. Specific contributions include:

- The collection and presentation of polarimetric scatterometer measurements of open water, newly-forming sea ice, first year sea ice, and multiyear sea ice. A variety of naturally occurring surface coverage types were investigated, dependent upon the ice condition at each of our measurement sites. Polarimetric C-band scatterometer measurements were conducted at each site and analyzed in conjunction with the geophysical measurements.

- Analysis of the copolarization correlation coefficient, ρ_{hhvv}, describing it as a potential candidate for determining sea ice thickness. We were able to separate sea ice thickness into two separate regimes: ice that was less than 6 cm thick and ice that was greater than 8 cm thick. The statistical relationship was consistent for an assortment of sea ice types under a variety of surface conditions.

- Focused studies on the physical characteristics of frost flower covered sea ice. We took special care to measure the salinity, structure, and physical description of frost flowers in order to provide natural field-based results (as opposed to laboratory measurements).

In terms of model development, we have made contributions in time-domain computational electromagnetic techniques. Our work built upon the previously developed parallel FVTD engine that was created within the Computational Electromagnetics Group in the Department of Electrical and Computer Engineering at the University of Manitoba.

- Implementation of a plane-wave source for multi-layered media in a scattered-field formulation of an FVTD solver. We created a 1D-FDTD numerical solution for plane wave propagation through multi-layered media and developed an interpolation method so that it could act as the source in the unstructured FVTD mesh. The method was validated through comparison, and good agreement, with other numerical solvers and previously published literature.

- Development of a method for simulating rough surface scattering using a scattered-field formulation. A method that represents the rough surface as contrast sources in the presence of layered media was developed and validated through good agreement with the SPM for rough surface scattering.

- Demonstration of a homogenization technique of an inhomogeneous medium

using the FVTD method for the purposes of simplifying a scattering model. A homogenization technique for an inhomogeneous medium populated by randomly located dielectric inclusions was created. The method was validated for the canonical case of dielectric spheres and the results showed that for the size of inclusions and the dielectric contrasts used, the PVD mixture model was an appropriate approximation for our sea ice scattering model.

Finally, we have explored the use of an FVTD Monte Carlo Method for computing the scattering of electromagnetic waves from a computational domain representative of an actual sea ice remote sensing experiment.

- Utilized the physical measurements and derived dielectric values to create a geometry that mimicked the sea ice medium. We used well-established dielectric modeling techniques to convert the physical measurements (temperature, salinity, and structure) of sea ice to equivalent relative dielectric constant values. The multi-layered, rough surface, scattering model that was developed in the FVTD framework was used to simulate wave propagation and scattering from the computational mesh that was representative of a sea ice medium.

- Successfully matched experimentally obtained scatterometer data with modeled outputs for the co-polarized return (σ^0_{HH}) within a reasonable tolerance. Modifications are required to the FVTD engine (such as anisotropic media) in order to match the cross-polarized signal. Another approach is needed to simulate σ^0_{VV}.

To our knowledge, this is the first time that the FVTD method for electromagnetics has been used for modeling remote sensing of sea ice.

7.2 Future Work

This thesis has touched upon many different aspects for understanding the propagation and scattering of electromagnetic waves with sea ice, ranging from measurement techniques to simulation techniques. There are many different future projects that could be undertaken following this thesis, which we summarize in the following.

In terms of experimentation, we encountered many different challenges and difficulties when collecting both physical data and scatterometer data. Our ship-based research platform, the CCGS *Amundsen*, provided us with many opportunities to perform measurements on a variety of sea ice types. The ship gave us a unique opportunity to visit newly-forming sea ice, which is not generally accessible in the field. For example, some of the ice types we visited would not support the weight of a person walking on it, and so, we were suspended over the ice using the ship's ice cage. In this manner, we were able to conduct the physical sampling necessary to provide ground truth data for our scatterometer measurements. Furthermore, it was a logistical challenge for the ship to remain stationary during measurements and to provide a large time window in which to perform our sampling. Due to these logistical challenges, we were not able to perfectly characterize the sea ice, but we were able to identify some critical measurements from our research. Furthermore,

some of our future experimentation suggestions are driven by the desire to obtain a better understanding of the sea ice environment. We recommend the following:

- Improve upon the methods for measurement of surface roughness parameters (for example, by using a Lidar system and statistical analysis). The surface roughness is a very important parameter for sea ice signature modeling, yet it is a logistical challenge to make such measurements. Even with a Lidar system, we expect difficulties will exist in making the measurements. For example, the presence of fog, and cold temperatures, could each hinder the system's operation.

- Utilize measurement systems with different frequencies to further our understanding of the interactions of microwaves with sea ice (for example, an L-band or X-band scatterometer system). Satellite-based platforms generally lack contemporariness; moreover, ship-based systems could provide the measurements at multiple frequencies simultaneously. A new scatterometer system could be deployed on the ship, or any other measurement platform, in order to obtain scattering measurements at other frequencies. Some challenges would exist in ensuring that the separate systems were measuring equivalent sea ice surfaces. Having a single system with broadband capabilities (for example, ranging from L-band to X-band), would be the best from the perspective of logistical constraints; however, it would be a major challenge to design the system.

In the EM modeling component of this thesis, we explored the use of the FVTD

method for simulating scattering from sea ice and from dielectric inhomogeneities in multi-layered media. As it stands, the FVTD computational engine is an excellent candidate for such simulations; however, we have not fully realized the potential of the computational method. For example, we spent substantial time in ensuring that our simulation method would be capable of modeling inhomogeneities; however, when modeling sea ice, we found that we were able to obtain satisfactory results (for HH) without incorporating a volume scattering aspect, and also by considering the sea ice to be a simple dielectric medium. In terms of modeling, we recommend the following:

- Add anisotropic capabilities to our implementation of the FVTD method. The current implementation of our FVTD engine assumes isotropic media for each distinct volumetric region of the computational domain. Modifications to the base FVTD algorithm could be created to permit a matrix representation of the relative permittivities and conductivities, such that an anisotropic medium could be represented in the computational geometry. The capability to model anisotropic media would provide further utility of the FVTD engine, and in the context of sea ice, would permit a better physical representation of the crystal structure of the ice.

- Parametric studies with different scales of roughness for the rough surface model. In Chapter 5, we demonstrated a method for generating rough surfaces with Gaussian statistics and mentioned the existence of others, such as the 1.5-power, and the exponential correlation function. The natural progression would be to

undertake parametric studies of surfaces with different correlation functions, such that the model would have a wider range of applicability. Additionally, superimposing multiple scales of roughness on a surface would be a possibility.

- Parametric studies of rough surfaces using TM polarization. In Chapter 4, we presented the derived expressions for TE and TM wave propagation, yet throughout the thesis we only presented results for a TE incident-field. In our work, we were successful at implementing the TM wave, but due to time constraints, we limited our study to only the TE simulations. The next step would be to perform parametric studies with the TM polarization, as we did for the TE polarization in Chapter 5.

A major goal of this thesis was to create a simulation method that was capable of emulating the scattering from sea ice, and ensuring that this model had good agreement with measured scatterometer response. In this thesis, we showed that our FVTD Monte Carlo Method provided good agreement for the co-polarized signal (HH), for three separate case studies. The other co-polarized signal (VV) was not simulated, and moreover, the simulated cross-polarized signal did not provide favorable agreement, as discussed in Chapter 6. The domination of surface scattering was a major assumption in our scattering model, and we represented the inhomogeneous sea ice medium as an isotropic, homogeneous dielectric substance. We are not stating that the dielectric mixture model approximation is appropriate in all cases of sea ice, since the size, shape, and volume fraction of the inclusions may play a role in the

scattering properties. We therefore recommend the following:

- Starting from our initial three case studies, create a database of modeling results with acceptable comparisons to experimental measurements. The knowledge obtained from further simulation results could help elucidate when the mixture model approximation is appropriate. Furthermore, these types of simulation studies could provide forward modeling data that could eventually be used in an inversion technique for extraction geophysical properties of the sea ice.

- Use the developed Monte Carlo Method as a simulation technique to study scattering from MYI. In the conclusion of Chapter 6, we suggested that the developed FVTD Monte Carlo Method for scattering simulations could be used for MYI since air pocket inclusions would be computationally tractable; whereas brine pockets increase the computational demands. One challenge would be in ensuring that the large-scale roughness (i.e. the effects of hummocks on the local incidence angle of the impinging EM wave) of the MYI is properly considered when comparing the scatterometer data to the simulation results.

Throughout our research, we have relied on field-based experimental data, in terms of both scattering measurements and geophysical characterization. It is clear that these types of data are extremely useful from a practical point of view, since they represent real scenarios of sea ice conditions. However, when sea ice grows, it is subjected to substantial environmental forcings, the most obvious being temperature

changes, wind, and wave action. When making field-based measurements, we cannot always determine the exact history of the growth of the sea ice and it is challenging to make measurements of the ice properties without significantly disturbing it. In order to reduce the effects of these uncontrollable variables, a laboratory setting would be very useful. Furthermore, in a laboratory setting, standard microwave engineering EM test equipment could be used since the robustness requirements of the field-based equipment could be relaxed. The University of Manitoba is currently building a unique sea ice research facility, known as SERF (Sea-ice Environmental Research Facility), which will provide an opportunity to take physical and scattering measurements of sea ice under a variety of controlled conditions. Specific test cases of interest could be investigated, such as the long-term fate of frost flowers as the year progresses from fall freeze-up into the winter (as discussed in Chapter 3). Measurements could be performed to improve upon our understanding of the relationship between ice thickness and ρ_{hhvv}, with a particular emphasis placed on studying the effects of the surface properties (see Chapter 3). Initially, we can study the scattering properties of sea ice using the C-band scatterometer and the new L-band scatterometer, similar to how we perform our measurements in the field; however, these instruments can be complimented by purpose-built instrumentation that will work under a large variety of frequencies and interrogation methods. For example, we can develop measurement devices that can be frozen into the ice in order to monitor the dielectric properties, which can then be linked to the thermodynamic and physical properties of the ice.

Electromagnetic simulation tools, such as the FVTD method used in this thesis, can be used to describe the propagation and scattering properties of the sea ice, in addition to modeling the actual devices used to make the measurements.

REFERENCES

[1] J. C. Comiso, C. L. Parkinson, R. Gersten, and L. Stock, "Accelerated decline in the Arctic sea ice cover," *Geophysical Research Letters*, vol. L01703, no. 35, 2008.

[2] D. G. Barber, "Microwave remote sensing, sea ice and Arctic climate," *Phys. Can.*, vol. 61, pp. 105–111, 2005.

[3] N. P. Walker, K. C. Partington, V.Woert, M. L. Street, and L. T. Towanda, "Arctic sea ice type and concentration mapping using passive and active microwave sensors," *IEEE Trans. Geosci. Remote Sens.*, vol. 44, no. 12, pp. 3574–3584, 2006.

[4] R. D. Abreu, D. Flett, B. Scheuchl, and B. Ramsay, "Operational sea ice monitoring with RADARSAT-2 - a glimpse into the future," Geoscience and Remote Sensing Symposium. IGARSS, 2003, pp. 1308–1310.

[5] D. P. Winebrenner, J. Bredow, A. K. Fung, M. R. Drinkwater, S. V. Nghiem, A. J. Gow, D. K. Perovich, T. C. Grenfell, H. C. Han, J. A. Kong, J. K. Lee, S. Mudaliar, R. G. Onstott, L. Tsang, and R. D. West, *Microwave Remote Sensing of Sea Ice*. Washington, DC: American Geophysical Union, 1992, vol. 68, ch. 8. Microwave Sea Ice Signature Modeling.

[6] T. MathWorks, "MATLAB 7, R2008b," 2008.

[7] W. F. Weeks and S. F. Ackley, "The growth, structure, and properties of sea ice," *CRREL Monogr.*, vol. 82, no. 1, 1982.

[8] G. F. N. Cox and W. Weeks, "Profile properties of undeformed first-year sea ice," CRREL, Hanover, N. H., Tech. Rep., 1988.

[9] L. H. Smedsrud and R. Skogseth, "Field measurements of Arctic grease ice properties and processes," *Cold Regions Science and Technology*, vol. 44, pp. 171–183, 2006.

[10] W. B. I. Tucker, D. K. Perovich, A. J. Gow, W. F. Weeks, and M. R. Drinkwater, *Microwave Remote Sensing of Sea Ice*. American Geophysical Union, 1992, vol. 68, ch. 2. Physical properties of sea ice relevant to remote sensing.

[11] G. Frankenstein and R. Garner, "Equations for determining the brine volume of sea ice from -0.5 °C to -22.9 °C," *J. Glaciol.*, vol. 6, no. 48, pp. 943–944, 1967.

[12] A. Assur, "Composition of sea ice and its tensile strength," *Arctic Sea Ice, Pub. 598*, pp. 106–138, 1958.

[13] G. F. N. Cox and W. F. Weeks, "Equations for determining the gas and brine volumes in sea-ice samples," *J. Glaciol.*, vol. 29, no. 102, pp. 306–316, 1983.

[14] K. M. Golden, S. F. Ackley, and V. I. Lytle, "The percolation phase transition in sea ice," *Science*, vol. 282, pp. 2238–2241, 1998.

[15] D. K. Perovich and A. J. Gow, "A statistical description of the microstructure of young sea ice," *J. Geophys. Res.*, vol. 96, no. C9, pp. 16 943–16 953, 1991.

[16] B. Light, G. A. Maykut, and T. C. Grenfell, "Effects of temperature on the microstructure of first-year Arctic sea ice," *J. Geophys. Res.*, vol. 108, no. C2, 2003.

[17] D. M. Cole and L. H. Shapiro, "Observations of brine drainage networks and microstructure of first-year sea ice," *J. Geophys. Res.*, vol. 103, pp. 21,739–21,750, 1998.

[18] D. K. Perovich and A. J. Gow, "A quantitative description of sea ice inclusions," *J. Geophys. Res.*, vol. 101, no. C8, pp. 18 327–18 343, 1996.

[19] H. Eicken, C. Bock, R. Wittig, H. Miller, and H. O. Poertner, "Magnetic resonance imaging of sea-ice pore fluids: Methods and thermal evolution of pore microstructure," *Cold Reg. Sci. Technol.*, vol. 31, pp. 207–225, 2000.

[20] N. Ono and T. Kasai, "Surface layer salinity of young sea ice," *Annals Glaciol.*, vol. 6, pp. 298–299, 1985.

[21] G. Cox and W. Weeks, "Brine drainage and initial salt entrapment in sodium chloride ice," CRREL, Tech. Rep., 1975.

[22] J. S. Wettlaufer and M. G. Worster, "Dynamics of premelted films: Frost heave in a capillary," *Physical Review E*, vol. 51, no. 5, pp. 4679–4689, 1995.

[23] D. G. Barber and L. Reddan, "Statistical analysis of the geophysical and electrical properties of snow on landfast first year sea ice," *J. Geophys. Res.*, vol. 100, no. C2, pp. 2673–2686, 1995.

[24] S. G. Warren, I. G. Rigor, N. Untersteiner, V. F. Radionov, N. N. Bryazgin, Y. I. Aleksandrov, and R. Colony, "Snow depth on Arctic sea ice," *J. Clim.*, vol. 12, pp. 1814–1829, 1999.

[25] M. Sturm, J. Holmgren, and D. K. Perovich, "Winter snow cover on the sea ice of the Arctic Ocean at the surface heat budget of the arctic ocean (SHEBA): Temporal evolution and spatial variability," *J. Geophys. Res.*, vol. 107, p. 8047, 2002.

[26] S. C. Colbeck, "An overview of seasonal snow metamorphism," *Reviews of Geophysics and Space Physics*, vol. 20, no. 1, pp. 45–61, 1982.

[27] S. Martin, Y. Yu, and R. Drucker, "The temperature dependence of frost flower growth on laboratory sea ice and the effect of the flowers on infrared observations of the surface," *J. Geophys. Res.*, vol. 101, no. C5, pp. 12 111–12 125, 1996.

[28] S. Martin, Drucker, R., and M. Fort, "A laboratory study of frost flower growth on the surface of young sea ice," *J. Geophys. Res.*, vol. 100, no. C4, pp. 7027–7036, 1995.

[29] D. K. Cheng, *Field and Wave Electromagnetics*, 2nd ed. New York: Addison-Wesley Publishing Company, Inc., 1992.

[30] A. Sihvola, *Electromagnetic Mixing Formulas and Applications*. London, United Kingdom: The Institution of Electrical Engineers, 1999.

[31] F. T. Ulaby, R. K. Moore, and A. K. Fung, *Microwave Remote Sensing: Active and Passive*. Norwood, MA: Artech House Inc., 1986, vol. 3.

[32] C. Mätzler and U. Wegmuller, "Dielectric properties of fresh-water ice at microwave frequencies," *J. of Physics D: Applied Physics*, vol. 20, pp. 1623–1630, 1987.

[33] A. Stogryn and G. D. Desargant, "The dielectric properties of brine in sea ice at microwave frequencies," *IEEE Trans. Antennas Propag.*, vol. AP-33, no. 5, pp. 523–532, 1985.

[34] M. Tiuri, A. Sihvola, E. Nyfors, and M. Hallikainen, "The complex dielectric constant of snow at microwave frequencies," *IEEE J. of Ocean. Eng.*, vol. OE-9, no. 5, pp. 377–38, 1984.

[35] A. K. Jordan and M. E. Veysoglu, "Electromagnetic remote sensing of sea ice," *Inverse Problems*, vol. 10, pp. 1041–1058, 1994.

[36] M. R. Drinkwater, R. Kwok, E. Rignot, H. Israelsson, R. G. Onstott, and D. P. Winebrenner, *Microwave Remote Sensing of Sea Ice*. Washington, D.C.: American Geophysical Union, 1992, vol. 68, ch. 24. Potential Applications of Polarimetry to the Classification of Sea Ice.

[37] M. I. Skolnik, *Radar Handbook*, 2nd ed. New York,: McGraw-Hill, 1990.

[38] L. Tsang and J. A. Kong, *Scattering of Electromagnetic Waves*. New York: Wiley, 2000.

[39] R. G. Onstott, *Microwave Remote Sensing of Sea Ice*. Washington, D.C.: American Geophysical Union, 1992, ch. 5. SAR and Scatterometer Signatures of Sea Ice.

[40] A. K. Fung, *Microwave Scattering and Emission Models and Their Applications*. Norwood, MA: Artech House, Inc., 1994.

[41] S. V. Nghiem, R. Kwok, S. H. Yueh, A. J. Gow, D. K. Perovich, J. A. Kong, and C. C. Hsu, "Evolution in polarimetric signatures of thin saline ice under constant growth," *Radio Science*, vol. 32, no. 1, 1997.

[42] K. C. Jezek, D. K. Perovich, K. M. Golden, C. Luther, D. G. Barber, P. Gogineni, T. C. Grenfell, A. K. Jordan, C. D. Mobley, S. V. Nghiem, and R. G. Onstott, "A broad spectral, interdisciplinary investigation of the electromagnetic properties of sea ice," *IEEE Trans. Geosci. Remote Sens.*, vol. 36, no. 5, pp. 1633–1641, 1998.

[43] S. V. Nghiem, M. Borgeaud, J. A. Kong, and R. T. Shin, "Polarimetric remote sensing of geophysical media with layer random medium model," *Progress in Electromagnetic Research (PIER)*, vol. 3, pp. 1–69, 1991.

[44] A. Stogryn, "Strong fluctuation theory for moist granular media," *IEEE Trans. Geosci. Remote Sens.*, vol. GE-23, no. 2, pp. 78–83, 1985.

[45] A. Ishimaru, *Wave Propagation and Scattering in Random Media*. New York: Academic Press, 1978, vol. 1 & 2.

[46] S. O. Rice, "Reflection of electromagnetic waves from slightly rough surfaces," *Communications on Pure and Applied Mathematics*, vol. 4, no. 2-3, pp. 351–378, 1951. [Online]. Available: http://dx.doi.org/10.1002/cpa.3160040206

[47] E. Nassar, "Numerical and experimental studies of electromagnetic scattering from sea ice," Ph.D. dissertation, Ohio State University, 1997.

[48] W. R. Tinga, "Mixture laws and microwavematerial interactions," *Progress in Electromagnetic Research (PIER)*, vol. 6, no. Monograph Series on Dielectric Properties of Heterogeneous Materials, pp. 1–40, 1992.

[49] M. E. Shokr, "Field observations and model calculations of dielectric properties of Arctic sea ice in the microwave C-band," *IEEE Trans. Geosci. Remote Sens.*, vol. 36, pp. 463–478, 1998.

[50] K. Golden, "Bounds on the complex permittivity of sea ice," *J. Geophys. Res.*, vol. 100, no. C7, pp. 13 699–13 711, 1995.

[51] L. Jylhä and A. Sihvola, "Numerical modeling of disordered mixture using pseudorandom simulations," *IEEE Trans. Geosci. Remote Sens.*, vol. 43, no. 1, pp. 59–64, 2005.

[52] K. Kärkkäinen, A. Sihvola, and K. Nikoskinen, "Effective permittivity of mixtures: Numerical validation by the FDTD method," *IEEE Trans. Geosci. Remote Sens.*, vol. 38, no. 3, pp. 1303–1308, 2000.

[53] D. P. Landau and K. Binder, *A Guide to Monte-Carlo Simulations in Statistical Physics*, 3rd ed. New York, USA: Cambridge University Press, 2009.

[54] A. Taflove and S. C. Hagness, *Computational Electrodynamics: The Finite-Difference Time-Domain Method*, 2nd ed. Norwood, MA: Artech House, Inc., 2000.

[55] K. S. Yee, "Numerical solution of initial boundary value problems involving Maxwell's equations in isotropic media," *IEEE Trans. Antennas Propag.*, vol. 14, pp. 302–307, 1966.

[56] P. Bonnet, X. Ferrieres, P. L. Michielsen, and P. Klotz, *Finite Volume Time Domain Method*, S. M. Rao, Ed. San Diego: Academic Press, 1999, in Time Domain Electromagnetics.

[57] D. Firsov, J. LoVetri, I. Jeffrey, V. Okhmatovski, C. Gilmore, and W. Chamma, "High-order FVTD on unstructured grids using an object-oriented computational engine," *ACES*, vol. 22, no. 1, pp. 71–82, 2007.

[58] M. N. O. Sadiku, *Monte Carlo Methods for Electromagnetics*. New York, USA: CRC Press, Taylor & Francis Group, 2009.

[59] C. D. Moss, F. L. Teixeira, Y. E. Yang, and J. A. Kong, "Finite-difference time-domain simulation of scattering from objects in continuous random media," *IEEE Trans. Geosci. Remote Sens.*, vol. 40, no. 1, pp. 178–186, 2002.

[60] K. Demarest, R. Plumb, and Z. Huang, "FDTD modeling of scatterers in stratified media," *IEEE Trans. Antennas Propag.*, vol. 43, no. 10, pp. 1164–1168, 1995.

[61] K. Uchida, K. Y. Yoon, and A. Ishimaru, "FVTD analysis of electromagnetic wave scattering by rough surface," vol. IV, DD11. IGARSS'98, 1998, pp. 2292–2294.

[62] H. Chanal, J. P. Segaud, P. Borderies, and M. Saillard, "Homogenization and scattering from heterogeneous media based on finite-difference-time-domain monte carlo computations," *J. Opt. Soc. Am. A*, vol. 23, no. 2, pp. 370–381, 2006.

[63] *Sea-Ice Nomenclature, Terminology, Codes and Illustrated Glossary*, Secretaria World Meteorol. Org., World Meteorol. Org., WMO/DMM/BMO 259-TP-145 Std., 1985.

[64] K. C. Partington, J. D. Flach, D. Barber, D. Isleifson, P. J. Meadows, and P. Verlaan, "Dual-polarization C-band radar observations of sea ice in the Amundsen Gulf," *IEEE Trans. Geosci. Remote Sens.*, vol. 48, no. 6, pp. 2685–2691, June 2010.

[65] D. Isleifson, B. Hwang, D. G. Barber, R. K. Scharien, and L. Shafai, "C-band polarimetric backscattering signatures of newly formed sea ice during fall freeze-up," *IEEE Trans. Geosci. Remote Sens.*, vol. 48, no. 8, pp. 3256–3267, Aug. 2010.

[66] R. Kwok, G. F. Cunningham, M. Wensnahan, I. Rigor, H. J. Zwally, and D. Yino, "Thinning and volume loss of the Arctic Ocean sea ice cover: 2003–2008," *J. Geophys. Res.*, vol. 114, p. C07 005, C7 2009.

[67] N. R. Bates and J. T. Mathis, "The Arctic Ocean marine carbon cycle: Evaluation of air-sea CO2 exchanges, ocean acidification impacts and potential feedbacks," *Biogeosciences*, vol. 6, pp. 2433–2459, 2009.

[68] W. Dierking, H. Skriver, and P. Gudmandsen, "On the improvement of sea ice classification by means of radar polarimetry," in *Proc. 23rd EARSel Symp. Remote Sens. Transition*, Ghent, Belgium, 2004, pp. 203–209.

[69] S.-E. Shih, K.-H. Ding, S. Nghiem, C.-C. Hsu, J. A. Kong, and A. Jordan, "Thin saline ice thickness retrieval using time-series C-band polarimetric radar measurements," *IEEE Trans. Geosci. Remote Sens.*, vol. 36, no. 5, pp. 1589–1598, Sep. 1998.

[70] D. K. Perovich, *The Optical Properties of Sea Ice.* Helsinki, Finland: Helsinki University Press, 1998, vol. 1, pp. 195–230.

[71] S. V. Nghiem, S. Martin, D. K. Perovich, R. Kwok, R. Drucker, and A. J. Gow, "A laboratory study of the effect of frost flowers on C-band radar backscatter from sea ice," *J. Geophys. Res.*, vol. 102, no. C2, pp. 3357–3370, February 1997.

[72] D. G. Barber and S. V. Nghiem, "The role of snow on the thermal dependence of microwave backscatter over sea ice," *J. Geophys. Res.*, vol. 104, no. C11, pp. 25 789–25 803, 1999.

[73] D. G. Barber and A. Thomas, "The influence of cloud cover on the radiation budget, physical properties, and microwave scattering coefficient of first-year and multiyear sea ice," *IEEE Trans. Geosci. Remote Sens.*, vol. 36, no. 1, pp. 38–50, 1998.

[74] D. Isleifson, A. Langlois, D. Barber, and L. Shafai, "C-band scatterometer measurements of multiyear sea ice before fallfreeze-up in the Canadian Arctic," *IEEE Trans. Geosci. Remote Sens.*, vol. 47, no. 6, pp. 1651–1661, June 2009.

[75] T. Geldsetzer, J. Mead, J. Yackel, R. Scharien, and S. Howell, "Surface-based polarimetric C-band scatterometer for field measurements of sea ice," *IEEE Trans. Geosci. Remote Sens.*, vol. 45, no. 11, pp. 3405–3416, 2007.

[76] N. P. Fofonoff, "Physical properties of seawater: A new salinity scale and equation of state for seawater," *J. Geophys. Res.*, vol. 90, no. C2, pp. 3332–3342, 1985.

[77] J. K. Ehn, B. J. Hwang, R. J. Galley, and D. G. Barber, "Investigations of newly formed sea ice in the Cape Bathurst polynya: 1. Structural, physical, and optical properties," *J. Geophys. Res.*, vol. 112, no. C5, p. C05 003, May 2007.

[78] P. Beckmann and A. Spizzichino, *The Scattering of Electromagnetic Waves from Rough Surfaces*, 2nd ed. Norwood, MA: Artech House, 1987.

[79] S. Beaven and S. P. Gogineni, "Radar backscatter measurements from Arctic sea ice during the fall freeze-up," in *Proc. Better Understand. Earth Environ.*, vol. 2. IGARSS, 1993, pp. 850–852.

[80] S. G. Beaven, S. P. Gogineni, and M. Shanableh, "Radar backscatter signatures of thin sea ice in the central Arctic," *Int. J. Remote Sens.*, vol. 15, no. 5, pp. 1149–1154, 1994.

[81] J. Grandell, J. Pallonen, M. Hallikainen, and M. Toikka, "Scatterometer measurements of Arctic sea ice at C-band," in *Proc. Better Understand. Earth Environ.* IGARSS, 1993, pp. 853–854.

[82] K. Pimsamarn, "Electromagnetic scattering model for saline ice covered with frost flowers," Master's thesis, MIT, 1997.

[83] R. Onstott, P. Gogineni, A. Gow, T. Grenfell, K. Jezek, D. Perovich, and C. Swift, "Electromagnetic and physical properties of sea ice formed in the presence of wave action," *IEEE Trans. Geosci. Remote Sens.*, vol. 36, no. 5, pp. 1764–1783, Sep. 1998.

[84] S. V. Nghiem, R. Kwok, S. H. Yueh, J. A. Kong, C. C. Hsu, M. A. Tassoudji, and R. T. Shin, "Polarimetric scattering from layered media with multiple species of scatterers," *Radio Science*, vol. 30, no. 4, pp. 835–852, Nov. 1995.

[85] S. V. Nghiem, R. Kwok, S. H. Yueh, and M. R. Drinkwater, "Polarimetric signatures of sea ice 2. experimental observations," *J. Geophys. Res.*, vol. 100, no. C7, 1995.

[86] F. Mattia, T. Le Toan, J.-C. Souyris, C. De Carolis, N. Floury, F. Posa, and N. Pasquariello, "The effect of surface roughness on multifrequency polarimetric sar data," *IEEE Trans. Geosci. Remote Sens.*, vol. 35, no. 4, pp. 954–966, Jul. 1997.

[87] S. Malhotra, D. Kasilingam, and D. Schuler, "The dependence of polarimetric coherence on surface roughness for very rough surfaces," vol. 3. IGARSS, 2003, pp. 1654–1656.

[88] B. J. Hwang, J. K. Ehn, and D. G. Barber, "Impact of ice temperature on microwave emissivity of thin newly formed sea ice," *J. Geophys. Res.*, vol. 113, no. C2, p. C02 021, Feb. 2008.

[89] D. Isleifson, I. Jeffrey, L. Shafai, J. LoVetri, and D. G. Barber, "An efficient scattered-field formulation for objects in layered media using the FVTD method," *IEEE Trans. Antennas Propag.*, in press.

[90] S. V. Nghiem, R. Kwok, S. H. Yueh, and M. R. Drinkwater, "Polarimetric signatures of sea ice 1. theoretical model," *J. Geophys. Res.*, vol. 100, no. C7, 1995.

[91] M. El-Shenawee, "Polarimetric scattering from two-layered two-dimensional random rough surfaces with and without buried objects," *IEEE Trans. Geosci. Remote Sens.*, vol. 42, no. 1, pp. 67–76, 2004.

[92] T. J. Cui and W. C. Chew, "Fast evaluation of Sommerfeld integrals for electromagnetic scattering and radiation by three-dimensional buried objects," *IEEE Trans. Geosci. Remote Sens.*, vol. 37, no. 2, pp. 887–900, 1999.

[93] D. Hill, "Electromagnetic scattering by buried objects of low contrast," *IEEE Trans. Geosci. Remote Sens.*, vol. 26, no. 2, pp. 195–203, 1988.

[94] I. Capoglu and G. Smith, "A total-field/scattered-field plane-wave source for the FDTD analysis of layered media," *IEEE Trans. Antennas Propag.*, vol. 56, no. 1, pp. 158–169, 2008.

[95] Y. Fang, L. Wu, and J. Zhang, "Excitation of plane waves for FDTD analysis of anisotropic layered media," *IEEE Antennas Wireless Propag. Lett.*, vol. 8, pp. 414–417, 2009.

[96] T. Tan and M. Potter, "FDTD discrete planewave (FDTD-DPW) formulation for a perfectly matched source in TFSF simulations," *IEEE Trans. Antennas Propag.*, vol. 58, no. 8, pp. 2641–2648, 2010.

[97] K. Sankaran, C. Fumeaux, and R. Vahldieck, "Cell-centered finite-volume-based perfectly matched layer for time-domain Maxwell system," *IEEE Trans. Microw. Theory Tech.*, vol. 54, no. 3, pp. 1269–1276, 2006.

[98] T. J. Cui, W. Wiesbeck, and A. Herschlein, "Electromagnetic scattering by multiple three-dimensional scatterers buried under multilayered media. II. Numerical implementations and results," *IEEE Trans. Geosci. Remote Sens.*, vol. 36, no. 2, pp. 535–546, 1998.

[99] C. Geuzaine and J.-F. Remacle, "Gmsh: A three-dimensional finite element mesh generator with built-in pre- and post-processing facilities," *Int. J. for Num. Methods in Eng.*, vol. 79, no. 11, pp. 1309–1331, 2009.

[100] D. Isleifson and L. Shafai, "Numerical homogenization of heterogeneous media using FVTD simulations," in *Antenna Technology and Applied Electromagnetics the American Electromagnetics Conference (ANTEM-AMEREM), 2010 14th International Symposium on*, 2010, pp. 1–4.

[101] K. Sarabandi and P. Polatin, "Electromagnetic scattering from two adjacent objects," *IEEE Trans. Antennas Propag.*, vol. 42, no. 4, pp. 510–517, 1994.

[102] C. A. Balanis, *Advanced Engineering Electromagnetics*. USA: John Wiley & Sons, Inc., 1989.

[103] M. N. O. Sadiku, *Numerical Techniques in Electromagnetics*, 2nd ed. New York, New York: CRC Press, 2001.

[104] D. Bergström, J. Powell, and A. F. Kaplan, "The absorption of light by rough metal surfaces–a three-dimensional ray-tracing analysis," *Journal of Applied Physics*, vol. 103, no. 10, p. 103515, 2008. [Online]. Available: http://link.aip.org/link/?JAP/103/103515/1

[105] D. Isleifson, L. Shafai, and D. G. Barber, "Numerical scattering from 3D randomly rough surfaces using FVTD," in *2011 IEEE International Symposium on Antennas and Propagation and USNC-URSI National Radio Science Meeting*, 2011.

[106] N. Garcia and E. Stoll, "Monte Carlo calculation for electromagnetic-wave scattering from random rough surfaces," *Phys. Rev. Lett.*, vol. 52, no. 20, pp. 1798–1801, May 1984.

[107] A. K. Fung, M. R. Shah, and S. Tjuatja, "Numerical simulation of scattering from three-dimensional randomly rough surfaces," *IEEE Trans. Geosci. Remote Sens.*, vol. 32, 1994.

[108] F. D. Hastings, J. B. Schneider, and S. L. Broschat, "A Monte Carlo FDTD technique for rough surface scattering," *IEEE Trans. Antennas Propag.*, vol. 43, no. 11, pp. 1183–1191, 1995.

[109] Y. Altuncu, A. Yapar, and I. Akduman, "On the scattering of electromagnetic waves by bodies buried in a half-space with locally rough interface," *IEEE Trans. Geosci. Remote Sens.*, vol. 44, no. 6, pp. 1435–1443, June 2006.

[110] R. Marchand and G. Brown, "On the use of finite surfaces in the numerical prediction of rough surface scattering," *IEEE Trans. Antennas Propag.*, vol. 47, no. 4, pp. 600–604, April 1999.

[111] K. F. Warnick and W. C. Chew, "Numerical simulation methods for rough surface scattering," *Waves in Random Media*, vol. 11, no. 1, pp. 1 – 30, 2001. [Online]. Available: http://www.informaworld.com.proxy1.lib.umanitoba.ca/10.1088/0959-7174/11/1/201

[112] F. T. Ulaby, R. K. Moore, and A. K. Fung, *Microwave Remote Sensing: Active and Passive.* Norwood, MA: Artech House Inc., 1982-1986, vol. 2.

[113] N. Metropolis, A. W. Rosenbluth, M. N. Rosenbluth, A. H. Teller, and E. Teller, "Equation of state calculations by fast computing machines," *J. Chem. Phys*, vol. 21, pp. 1087–1092, 1953.

[114] W. H. Press, *Numerical Recipes in C++: The Art of Scientific Computing*, 2nd ed. New York: Cambridge University Press, 2002.

[115] L. Klein and C. Swift, "An improved model for the dielectric constant of sea water at microwave frequencies," *IEEE Trans. Antennas and Propag.*, vol. 25, no. 1, pp. 104 – 111, Jan. 1977.

[116] C. F. Bohren and D. R. Huffman, *Absorption and Scattering of Light by Small Particles.* New York, USA: John Wiley & Sons, Inc., 1983.

[117] S. G. Beaven, S. P. Gogineni, A. Gow, A. Lohanick, and K. Jezek, "Radar backscatter measurements from simulated sea ice during CRRELEX'90," RSL Technical Report 8243-2, Tech. Rep., 1993.